INTEGRATION OF CARBON NANOTUBE AND VANADIUM DIOXIDE THIN FILMS IN PHOTO-THERMAL ACTUATORS

By

Tongyu Wang

A DISSERTATION

Submitted to
Michigan State University
in partial fulfillment of the requirements
for the degree of

Electrical Engineering – Doctor of Philosophy

2017

ABSTRACT

INTEGRATION OF CARBON NANOTUBE AND VANADIUM DIOXIDE THIN FILMS IN PHOTO-THERMAL ACTUATORS

By

Tongyu Wang

This thesis proposal presents a series of studies which explores the use of single wall carbon nanotubes (SWNT) as a light absorber in VO_2 photo-thermal actuators. The recent strong interest in VO_2 among applied researchers has been driven by the drastic and reversible changes in the properties of this smart material, such as electrical resistivity and optical transmissivity, across its phase transition. This phase transition, also called insulator-to-metal transition (IMT), occurs at a temperature of about 68 °C and spans about 5 °C, which is highly hysteretic and temperature-dependent. Although this temperature range is close to room temperature, it still represents a considerable power burden for practical transducer applications, especially for photo-thermal actuators. Current efforts to reduce the transition temperature in VO_2 thin films involve doping or growing pre-stressed films. Nevertheless, the aforementioned approaches have great limitations due to either reduced material property change across the phase transition or requirement of specific substrates, respectively. Rather than compromising the advantages of VO_2, this paper proposes a new method based on a SWNT-VO_2 hybrid structure that utilizes the strong optical absorbance of SWNT. The devices allow more efficient triggering of the phase transition in VO_2 by light irradiation. The chirality dependent optical property of SWNT also enables a simple solution for wavelength selective micro-actuator and allows exploration of new applications based on photo-thermal actuation.

To my grandma who probably does not understand single word of this thesis,
but raised me with her hidden love in the rough hands.

ACKNOWLEDGMENTS

I would like to express my sincere appreciation to my Advisor Dr. Nelson Sepúlveda and co-advisor Dr. Chuan Wang for their constant guidance and encouragement, without which this work would not have been possible. For their support, I am truly grateful. I would also like to thank my committee members, Dr. Junghoon Yeom and Dr. Wen Li, for their kind help and inspiration through this work.

I am grateful to my brother, Tonglei, and parents, Lianxi and Hongzhi, who have provided me unwavering support in my life. I would also like to thank my aunt and uncle Xiang and Xin, who constantly support and encourage me to pursue advanced degree.

I also want to thank former colleagues and forever friends, Dr. Rafmag Cabrera, Dr. David Torres and Dr. Wei Li, for their help along the way. I would like to express my appreciation to my friends and colleagues Yunqi Cao and José Figueroa for sharing wonderful time in the lab.

I am also grateful to the following university staff: Roxanne Peacock and Meagan Kroll for their unfailing support and assistance at Michigan State University.

A very special gratitude goes out to National Science Foundation Grants ECCS 1306311 and ECCS Award 1139773.

TABLE OF CONTENTS

LIST OF TABLES

LIST OF FIGURES

CHAPTER 1

INTRODUCTION

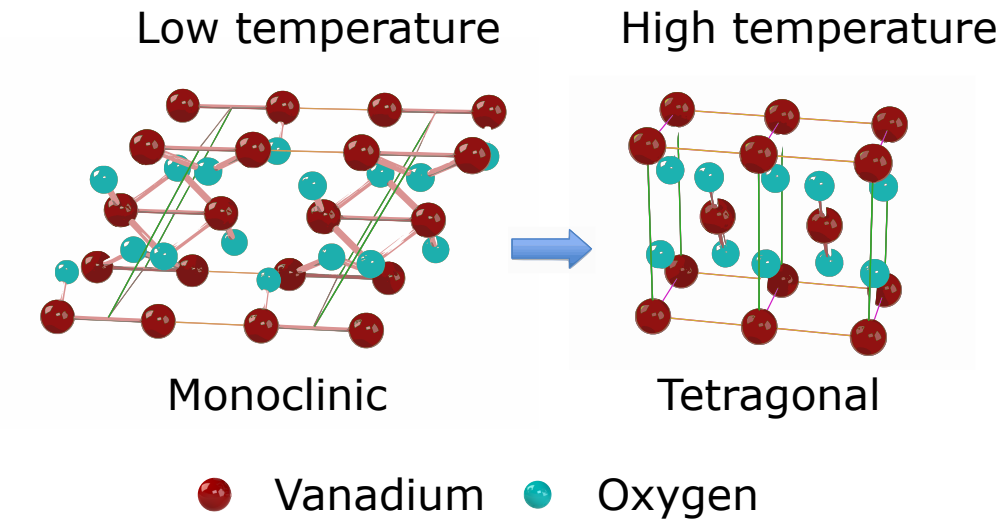

Figure 1.1: Structural phase transition of VO_2 at 68 °C.

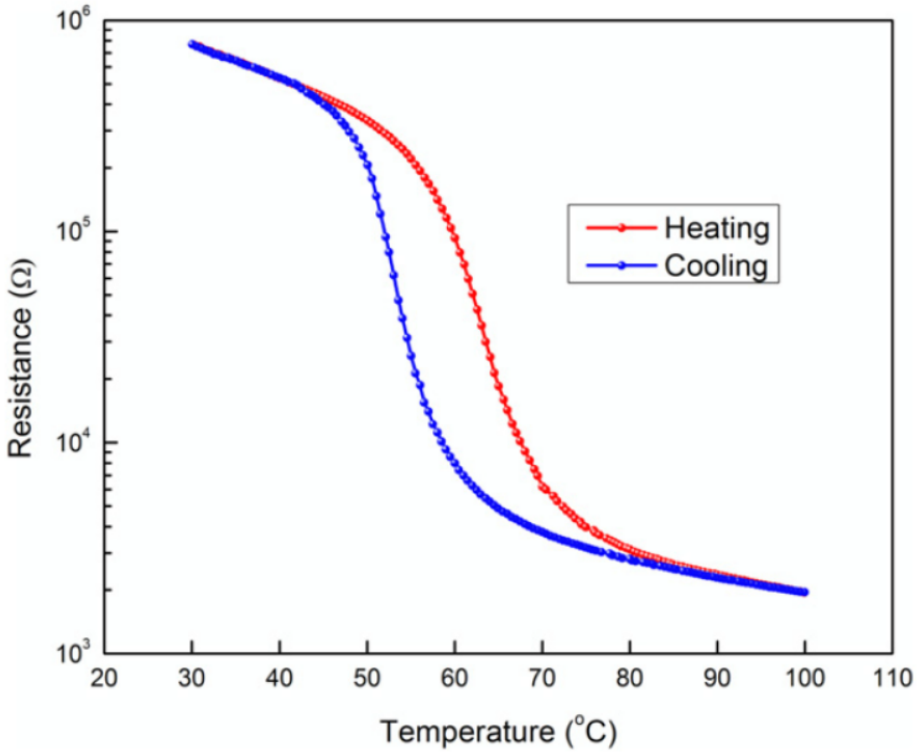

Figure 1.2: Resistance of a VO_2 thin film as a function of temperature [6].

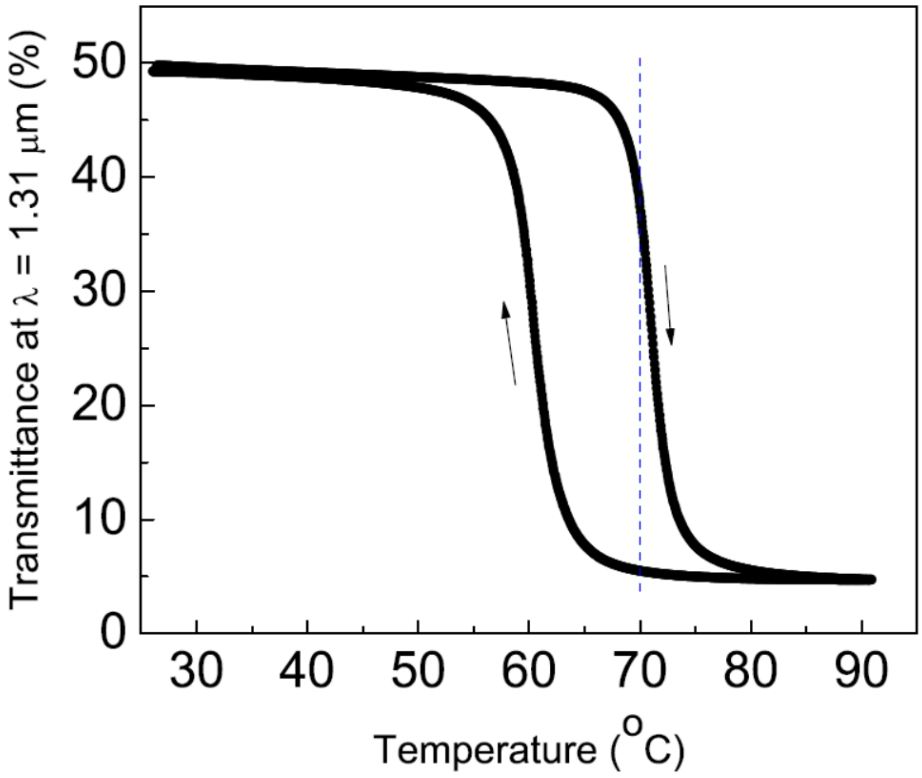

Figure 1.3: Optical transmission (wavelength 1.31 μm^2) of a VO_2 thin film as a function of temperature [7].

VO_2 goes through a fully reversible solid-to-solid phase transformation, in which the crystal structure changes from a monoclinic phase to a tetragonal phase at 68 °C (see **Figure** 1.1) [37, 38, 39]. The phase change can be induced in multiple ways (e.g. temperature [37], ultra-fast optical radiation [40], mechanical stress [41], and electric field [42]), resulting in abrupt change in the material's various properties [37, 39, 43]. **Figure** 1.2 (160 nm VO_2 thin film on single crystal silicon substrate [6]) and **Figure** 1.3 (210 nm VO_2 thin film on silicon dioxide (SiO_2) substrate [6]) show the changes of resistance and optical transmission of VO_2 across the transition. The understanding of the underlying physics in the phase change of VO_2 has drawn the attention of scientists for over 50 years [37, 44, 45, 46, 47], while the material's multi-functionality and fully reversible behavior has motivated applied scientists to integrate VO_2 in multiple devices, mainly in the last decade [26, 41, 48, 49, 50]. The promising applicability of VO_2 is further supported by the low temperature at which

the phase change can be induced (T $\sim$ 68 °C), which in fact makes it the material with the phase-change temperature closest to room temperature [51].

Although the electrical and optical changes of VO_2 during the phase transition were reported about 50 years ago, it was not until 2010 when the effects of the stress changes in the film across the phase transition in micro structures were revealed [26, 48]. It was reported that the change in area of the crystallographic planes in VO_2 parallel to the surface of a micrometer-sized cantilever is capable of producing stress levels that generate significant actuation displacements and strain energy densities [26, 52, 53] (see **Figure** 1.4). These results unveiled a new technology in micro transducers, where the actuation mechanism is based on the solid-to-solid phase-change of VO_2. Afterwards, other research groups expanded the work to include VO_2 nanowires [54, 55], the use of the hysteretic behavior in VO_2 to program multiple mechanical[56, 57, 49] and opto-electronic states [58], and the tuning of micromechanical resonators [56, 1].

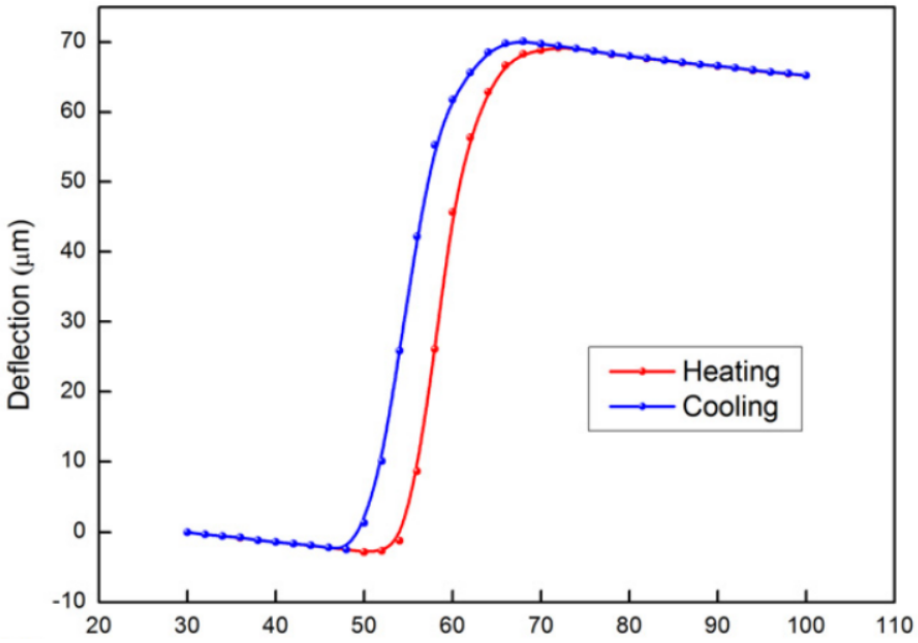

Figure 1.4: Displacement of a silicon cantilever coated with 160 nm VO_2 thin film as a function of temperature [6]. The temperature was controlled by peltier heater and circled between 30 °C to 100 °C.

In the field of micro actuators, some of the advantages of thermal micro-actuators over

their counterpart technologies (such as electrostatic [59] and piezoelectric actuators [60]) typically include large energy densities, low operating voltages, and large displacements [61, 62]. However, before VO_2-based thermal actuators were reported, the most typical mechanism used in thermal actuators was the difference in thermal expansion coefficients between two layers forming a bimorph structure. In order to achieve large actuation of such devices, relatively large temperatures had to be reached. Nevertheless, high operating temperatures can result in permanent deformation, structural damage, and degradation in performance [63, 64]. Furthermore, high actuation temperatures poses limitations on speed due to the long thermal constants (especially during cooling [1]). Phase-change actuation based on VO_2 represents a solution to this problem, by significantly lowering the actuation temperature to only ~ 68 °C. This lower actuation temperature was added to the multifunctionality aspect of VO_2 and large repeatable strain energy densities of VO_2-based actuators [52].

1.1 Problem Description and Motivation

Despite the advances made on exploiting VO_2's multifunctionality and low transition temperature in thermal actuators, little work has been done to increase the photo-thermal performance of VO_2-based photothermal actuators. One approach to reduce the required power for actuating VO_2 devices is to lower the transition temperature of the material. This has been previously achieved through doping at the cost of a reduced magnitude in the material property changes across the transition [65, 8] (see **Figure** 1.5 [8]) or deposition of pre-stressed VO_2 film on specific substrates, such as single crystal TiO_2 at the cost of a very expensive substrate and limitations during device fabrication [9, 66] (**Figure** 1.6 [9]).

In this work, a design (see **Figure** 1.7) is presented which utilizes the chirality-dependent optical properties of SWNTs. The presented VO_2/SWNT-based micromechanical photoactuators show displacements that are dependent on the wavelength of the incident light on the device, while maintaining excellent performance in terms of large displacements, low power consumption, large energy density, and fast response which are the most important

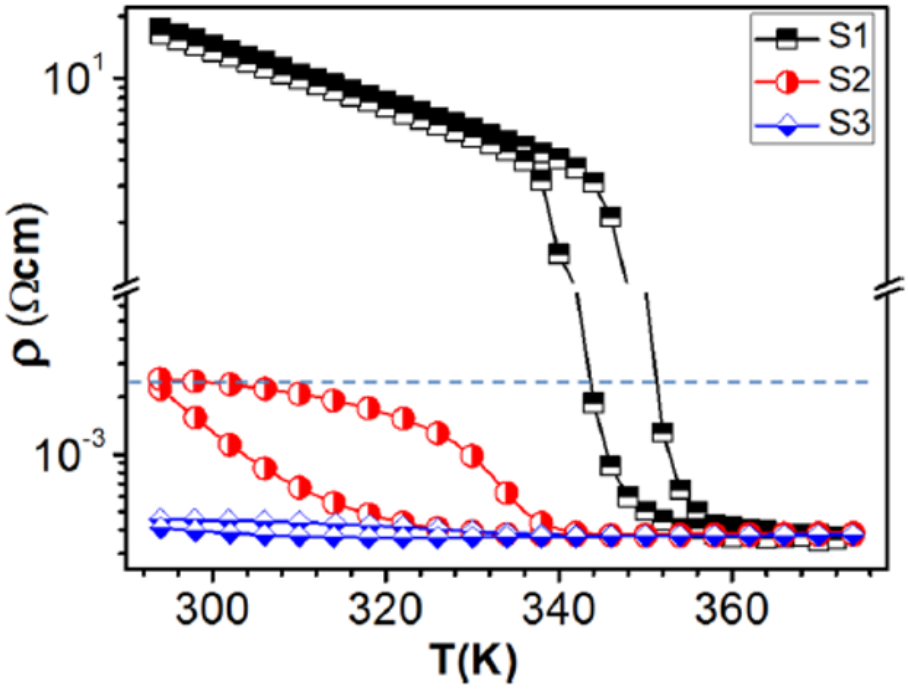

Figure 1.5: Reduced transition temperature of VO_2 achieved by hydrogen doping. [8]

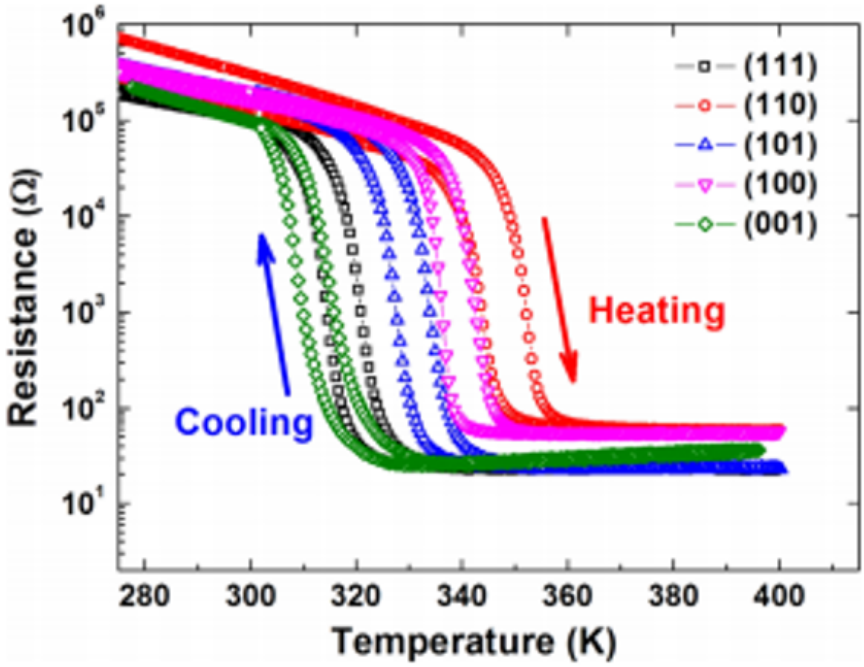

Figure 1.6: Reduce transition temperature of VO_2 achieved by growing pre-stressed VO_2 on very specific (and very expensive) substrates [9].

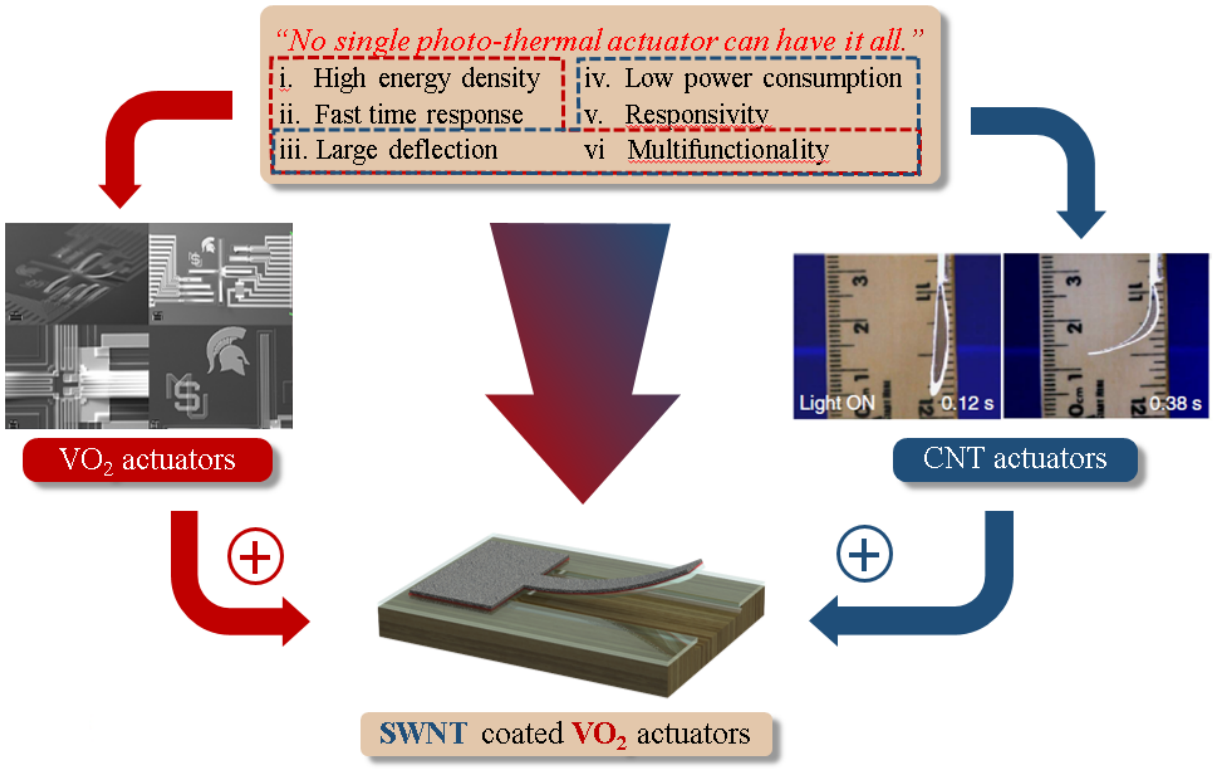

Figure 1.7: Design of VO_2/SWNT actuators.

criteria in MEMS. The large optical absorption of SWNTs to visible and near-infrared wavelengths has been demonstrated to induce significant local heating for thermal actuators [5]. Addition layer of SWNT on VO_2 devices as a light absorber can significantly improve their performances. Therefore, the effects of SWNTs with high photo-thermal absorption on VO_2 devices require to be studied, and characterizations of these devices including power efficiency, optical responsivity, wavelength selectivity and operation speed need to be done. The properties of SWNT, such as electrical conductivity and optical absorption, are dependent on its chirality. By using purified SWNT with different chirality distribution and thereby different absorption spectra, programmable wavelength-selective photo-actuator can be obtained. Utilizing such wavelength selective actuators, new applications such as soft micro-robotics, monochromatic sensors, and portable spectrometers become possible. The problems addressed in this work are:

- The fabrication process has to be explored including SWNT thin film deposition,

SWNT film transfer, compatible SWNT and VO_2 fabrication techniques.

- A VO_2-based MEMS actuator coated with SWNT thin film coated must be designed and fabricated.
- A detailed study of SWNT-coated VO_2 micro-actuators must be achieved, which includes conduction and photo-thermal actuation, calculations of photo-thermal efficiency, and demonstration of energy consumption reduction compared to VO_2 micro-actuators.
- The MEMS actuator must be characterized in terms of power efficiency, optical responsivity, and time responses.
- Based on the experimental results of unsorted SWNT coated VO_2-based actuators, a VO_2 actuator coated with different chirality distribution of SWNT thin must be designed and fabricated.
- A study of optical response to different wavelength of this VO_2 actuators.
- Characterization of SWNT (with different chirality distribution) coated VO_2 actuators including time response, power consumption, responsivity, and wavelength selectivity.
- Photo-thermo-mechanical process of this type of photothermal actuators must be modelled and analysed.

A series of experiments, simulations and analytical approaches are used to address these problems. The techniques used to fabricate SWNT coated VO_2 actuators can also be used for other types of VO_2-based structures.

1.2 Thesis Statement

This work presents the development of a SWNT and VO_2-based combined actuator with high performance. The main contributions are: development of compatible fabrication process of SWNT and VO_2; design and fabrication of devices integrated SWNT and VO_2;

demonstration of SWNT as an enhanced light absorber and capability of integration with VO_2; characterizations of SWNT coated VO_2 devices as a photo-thermal actuator in terms of power efficiency, optical responsivity, time responses, and wavelength selectivity; Modelling the photo-thermo-mechanical process of this type of actuators.

Thesis Statement: *The development of a new design micro-photo-thermal actuator is achieved through the successful integration of SWNT and VO_2, which enhances the performance of these devices in terms of power efficiency, optical responsivity, wavelength selectivity and time responses, and broadens their applications for photo-thermal driven VO_2 actuators.*

1.3 Research Contributions

In this work, the problems described in **Section 1.1** will be addressed. The fabrication techniques, including SWNT thin film deposition, SWNT film transfer, and compatible SWNT and VO_2 fabrication process, have been successfully developed. The photo-thermal actuation process in SWNT coated VO_2 actuator will be studied in terms of quasi-static and dynamic displacement, operation speed, wavelength selectivity and power consumption, which will be compared with VO_2 only actuator. The results from these studies demonstrate the advantages of using SWNT as the effective light absorption layer in VO_2 actuators. By characterizing the micro-actuator, a deeper understanding of SWNT effects can be reached and used for future optimizations. The successful design and fabrication of a wavelength selective VO_2 actuators based on specific SWNT chirality will allow further reduction of driven optical power and open a new area of applications.

1.4 Dissertation Outline

The remaining chapters are organized as follows; **Chapter 2** presents a thorough background on the MEMS actuator techniques, the optical and structural transition in VO_2, knowledge of SWNT including its chirality, optical, and thermal properties.In **Chapter 3**, a study of fabrication methods of SWNT thin film are presented, which involves vacuum filtra-

tion of SWNT solution, SWNT thin film transfer, as well as patterning of SWNT thin film that is compatible with VO_2. All the methods discussed in this chapter is used in all SWNT coated VO_2 devicess presented in this thesis. **Chapter 4** shows the design and fabrication of a SWNT coated VO_2 resistor. Experiments of temperature response and photo-thermal response of this device are carried out. In **Chapter 5**, the design and fabrication of a unsorted SWNT coated VO_2 actuator is presented. A thorough study of this device including temperature response, photo-thermal response, time response, and calculation of light absorption efficiency shows great improvement compared with VO_2 only actuator.**Chapter 6** VO_2 actuators coated with different chirality distribution SWNT thin films are studied. The wavelength selective actuation is also demonstrated in this chapter. Finally, **Chapter 7**, shows a summary of contributions and proposed work for further investigations.

CHAPTER 2

BACKGROUND

2.1 Micro-actuators

Micro-mechanical actuators are mechanical structures in micrometer dimensions, which can be driven by various forms of energy, and convert them into mechanical work. Typically, this mechanical work is delivered by generating large displacement or force applied on the load [67, 68, 69, 70, 16, 71, 72, 73, 74, 75, 76, 77, 78, 79, 80, 81, 82, 83, 84, 85]. In most cases, there is always a trade-off between displacement and force. Therefore, the total output work is often used to characterize certain actuators, and different actuation mechanisms are chosen and developed in order to achieve maximum displacement or force according to requirements of applications.

Several mature actuation techniques have been implemented and widely used in commercial micro-mechanical actuator applications, such as thermal [77, 78, 79, 80, 81, 82], electrostatic [70, 16, 71, 72, 73, 74, 75], magnetic [67, 68], and piezoelectric [69, 86, 87]. Among these actuation mechanism, thermal and electrostatic are two most common methods used in applications. However, these conventional methods have their own disadvantages and performance limits including power consumption, actuation speed, displacement, force, fabrication simplicity and compatibility, and robustness. A review on many actuation techniques was published in 2005, which includes selection criteria [73]. To improve these methods, new materials, especially smart materials, have been investigated and applied on micro-mechanical actuators driven by different mechanism. As a transition material based on temperature, VO_2 actuators is usually considered as thermal actuators, while its multi-property changes during transition give it extra features, such as self-sensing and self-control.

2.1.1 Thermal Actuators

Thermal actuators are devices that transduce heat to motion, which can be categorized into two families based on different heat effects: thermal expansion and phase change. There are two ways to utilize thermal expansion to generate motion. They are thermal bimorph structure and mono-material thermal stress structure. The thermal bimorph structure is typically a thin structure, in which two materials with significant different thermal expansion coefficient are bonded together. When temperature increases, the structure will adjust its geometry to allow one material to expand more than the other: bending motion. This technique has been used to develop a scanning micromirror for integration in an endoscope for in-vivo optical coherence tomography [10] (see **Figure** 2.1). The size of the square platform

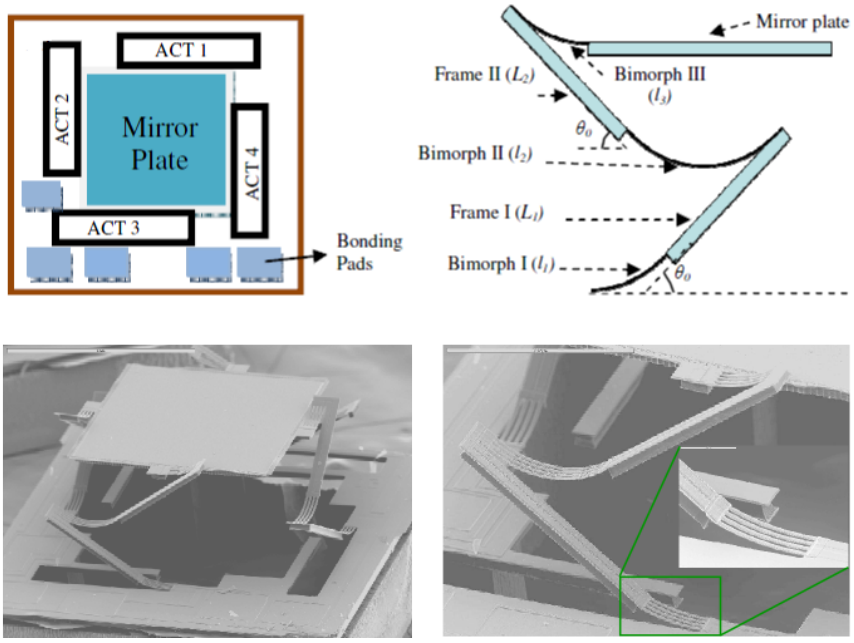

Figure 2.1: A scanning micromirror for integration in an endoscope for in-vivo optical coherence tomography [10].

of this micromirror is 1×1 mm, and more than 600 µm displacement can be achieved with only 5.5V voltage. ± 31 °C optical scan angles can be obtained at a maximum 5.5V, of which (531 °C) optical scanning ranges are linear. However, the power consumption for this micromirror is still relatively high (85 mW).

Mono-material thermal stress structure takes advantages of the geometry of actuators to have different expansions on different parts of the structure. Two examples are shown in **Figure** 2.2 and **Figure** 2.3. An U shape structure (see **Figure** 2.2), also called pseudo bimorph, consists of a thin hot arm and a thick cold arm, through which electrical current flows. Since the structure is made of same material, the thin hot arm has higher electric resistance than thick cold arm, resulting in higher temperature when current passes in beam [11]. The unbalance temperature distribution in the structure causes the beam to bend down. Although this structure can achieve horizontal deflection, its high power consumption and small displacement (10 µm at 10 V) limit its applications. Polyimide V-groove joint

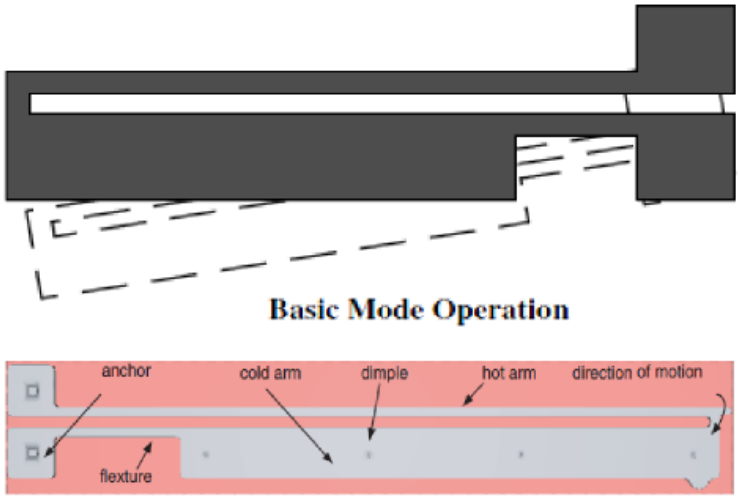

Figure 2.2: A pseudo bimorph beam consisting of a thin hot arm and a thick cold arm [11].

actuators have been implemented among microrobots and micro- conveyers applications [12]. **Figure** 2.3) shows one simple design utilizing polyimide V-groove joint to lift a platform. An embedded heater circuit is fabricated at the joint, where a couple of polyimide V-groove joints are placed. When the temperature increases , the top part and bottom part of V shape polyimide block expand proportionally the same. However, the absolute expansions ae dependent on the length of local polyimide, which causes the platform to bend down. Displacements from 100 µm to 500 µm can be achieved by this type of structure [12], while power consumption is its disadvantages (175 mW required to reach 150 µm displacement).

Moreover, the highest cut-off actuation frequency of this structure has been reported up to 40 Hz, which is mainly due to its low Young's modulus.

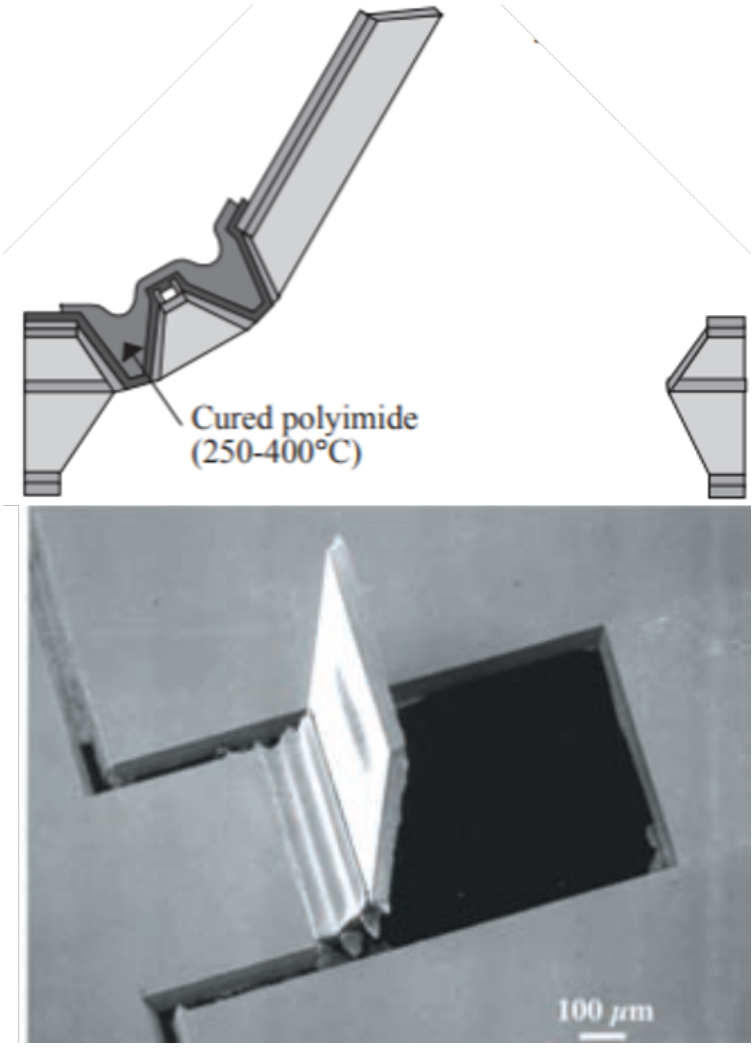

Figure 2.3: A polyimide V-groove joint actuator [12].

The phase change thermal actuators can be divided into two classes: thermopneumatic, and solid to solid phase transition. Thermopneumatic thermal actuators use phase changes to create pressure change, which can drive the motion. This type of thermal actuators are widely used in microfluidic applications [13]. In **Figure** 2.4 is a micropump made of thin PDMS membrane. Trapped liquid is kept inside the actuator cavity, underneath which there is a heater. During the actuation, heat converts liquid to vapour, pushing the membrane upwards. The diameter of the cavity is 2.5 mm, while the maximum deflection is about

123 µm. The problem of this actuator is its operation speed. A very low operation rate is reported as 2 Hz at maximum flow rate. As the operation speed increases, the deflection decreases. This deflection and speed trade-off is mainly because of the slow transfer process between liquid phase and gas phase. Recently researches of applying solid-to-solid phase

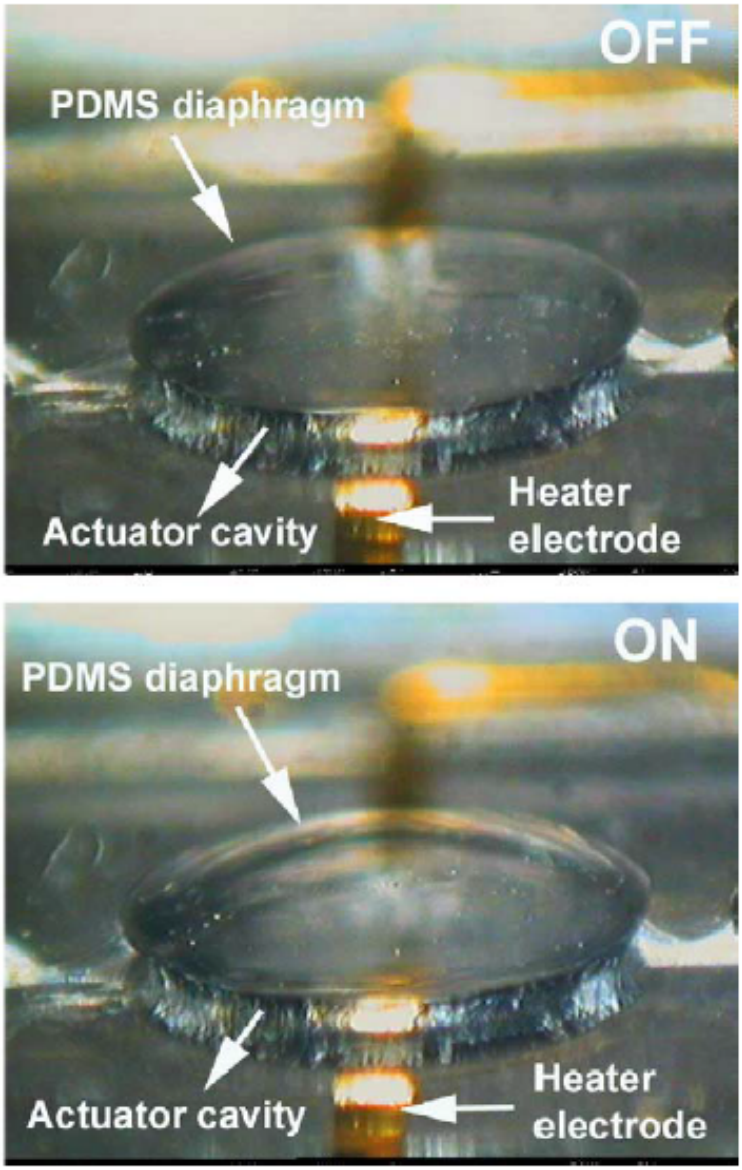

Figure 2.4: A PDMS micropump based on thermopneumatic effect [13].

transition materials into thermal actuaotrs become very popular. A well-known example is shape memory alloy (SMA), which is also considered as a smart material. Relative content will be discussed in the folowing "smart actuators" section.

2.1.2 Electrostatic Actuators

Micro-electrostatic actuators are based on the attractive or repelling effects between two charged plates. The typical designs for electrostatic actuator include combe drive [88], scratch drive [89], parallel plate [90], Inchworm [91], Impact [74], Distributed [92], Repulsive force [93], Curved electrode [94], S-shaped [95], and Electrostatic relay [96]. In order to achieve large displacement, high driving voltage is required, which limits sizes of gaps between charged plates. A narrow gap between electrodes can generate large electrical field because the mean free path of air molecules is larger than the gap allowing high breakdown electric filed. Electrostatic actuator can realize both linear (see **Figure** 2.5) and rotational motion. **Figure** 2.6 shows a electrostatic motor having a diameter of 1.4 mm , which demonstrated a rotational range of 26° (±13°) at 75 V and a maximum speed of 1.67° /ms.

Work to optimize topology designs is often required to achieve large output force or large output displacement. For comb drive actuator, 150 µm displacement has been achieved with 150 V (see **Figure** 2.7 [16]), while force of 2.5 mN has been obtained at 100 V (see **Figure** 2.8 [17]). The displacement can be further enhanced by the use of repeated motions or ratchetting mechanisms, as in scratch drives and impact actuators, which, however, are limited by the size of whole structure.

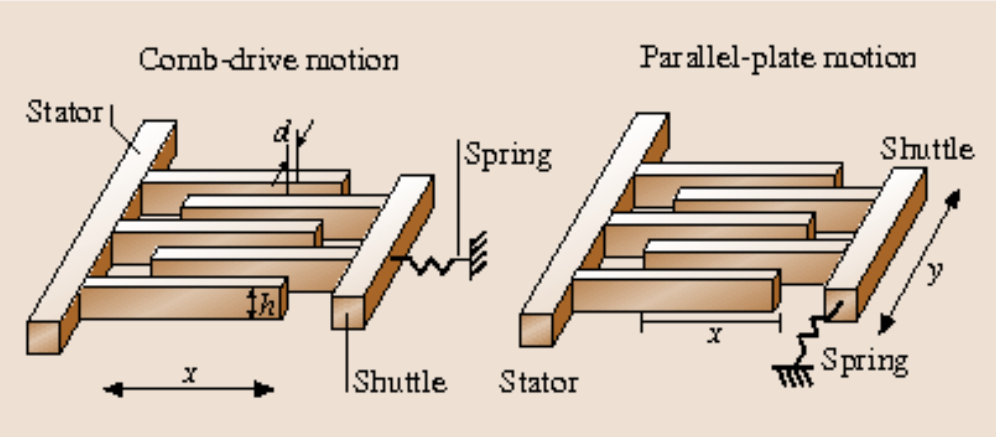

Figure 2.5: Design of electrostatice actuator for linear motion [14].

However, high operation voltage is still electrostatic micro actuator's biggest disadvantage

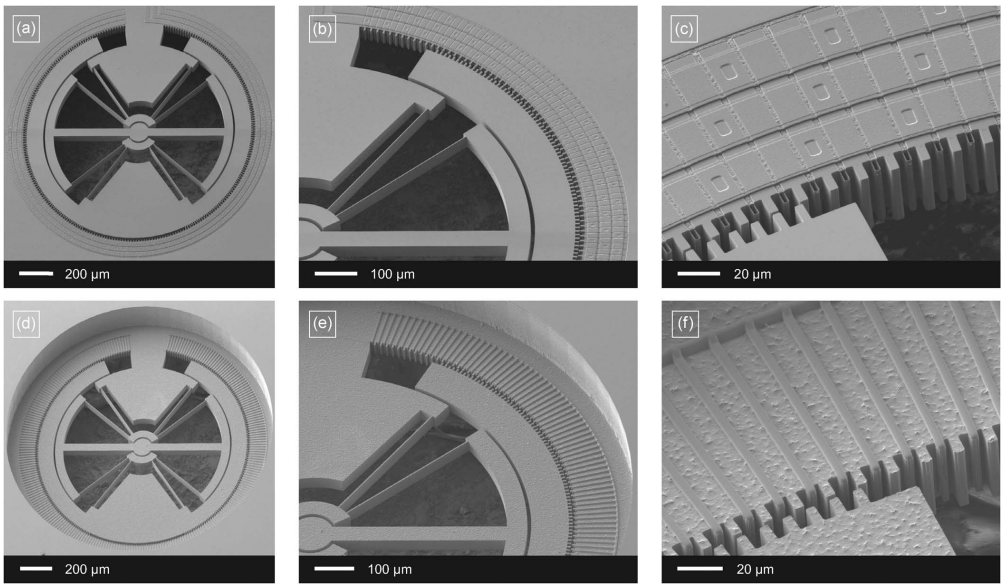

Figure 2.6: Three-phase electrostatic rotary stepper micromotor with a flexural pivot bearing[15].

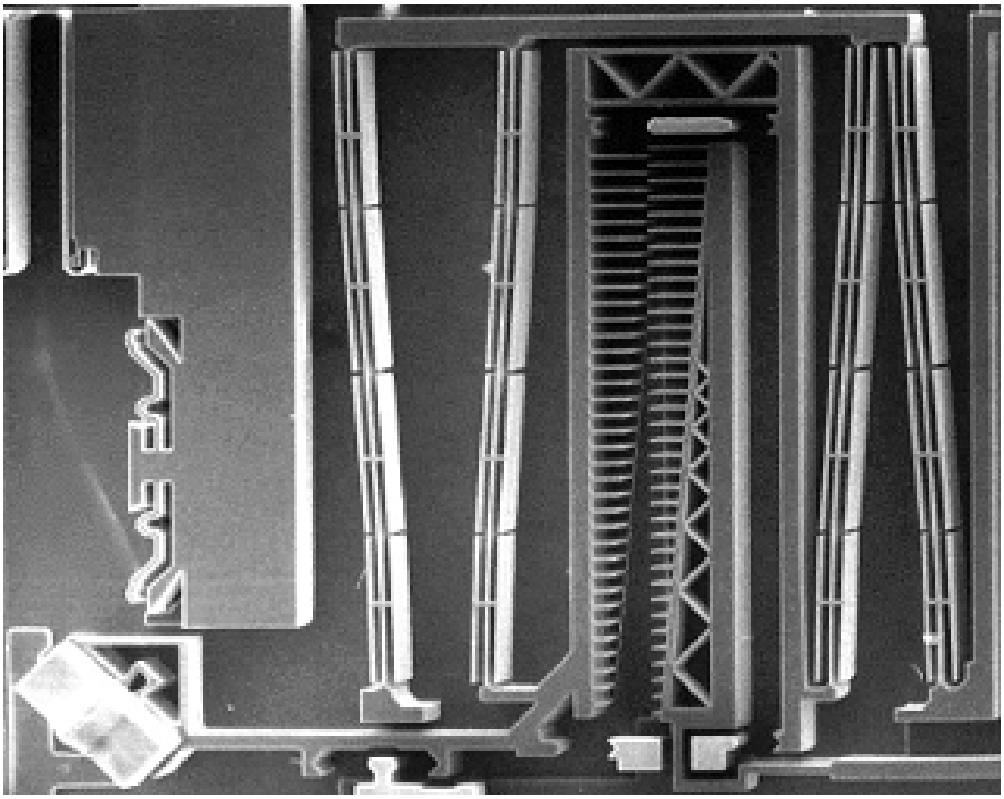

Figure 2.7: Electrostatic linear comb-drive micro-actuator with 150 µm at 150 V [16].

since high voltages are easy to get on a large device, but not on a very compact integrated system. Moreover, large surface area is required for comb-drives to generate forces equivalent to other micro-actuators.

2.1.3 Magnetic Actuator

Magnetic micro actuators are micrometer scale devices that use interaction among various magnetic elements, such as permanent magnets, external magnetic fields, magnetizable material, and current-carrying conduct. Magnetic micro actuator can be classified into electromagnetic [18], magnetostrictive [25], external magnetic [19], and magnetic relay [97, 20]. **Figure** 2.9 shows a bidirectional magnetic microactuator using electroplated permanent magnet arrays. It can achieve $\pm 80\,\mu m$ deflection by applying a dc current of 100 mA and altering its polarity. In **Figure** 2.10, it is a a micro-fabricated, membrane-type magnetic actuator driven by external magnetic field. A maximum displacement of $83\,\mu m$ is obtained in the presence of a 2.85×10^5 A/m external magnetic field.

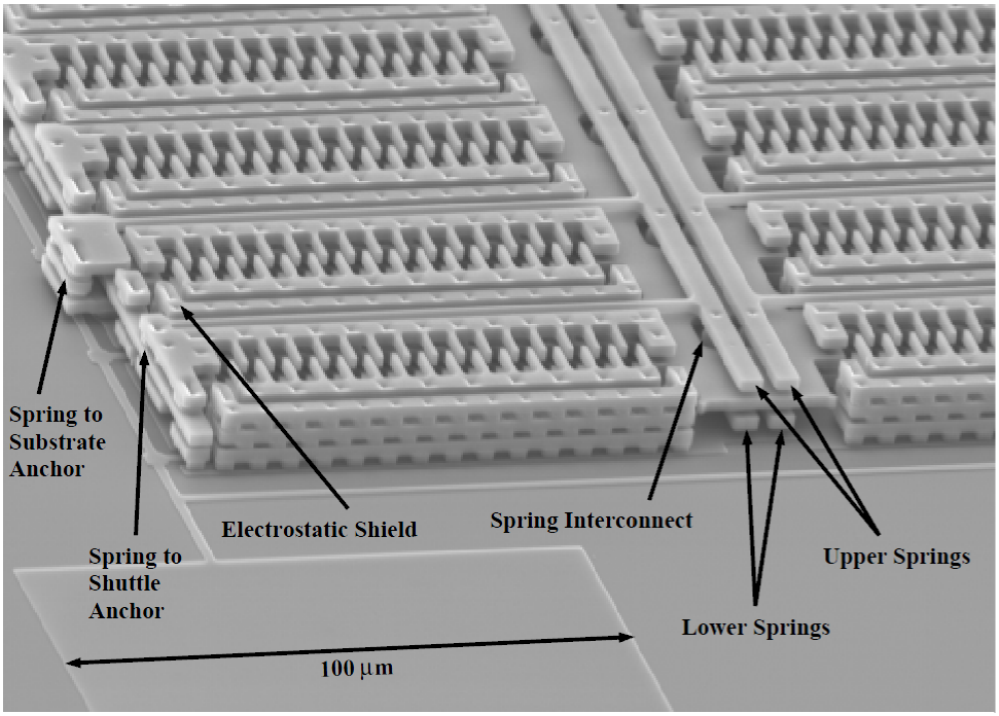

Figure 2.8: SEM image of a comb drive can achieve force of 2.5 mN at 100 V [17].

A magnetic relay structure is shown in **Figure** 2.11, which operated at 2 V and 8 mA, and output 2 mN force [20]. Magnetostrictive actuator is based magnetostrictive material that change their shape or dimensions during the process of magnetization. Magnetostrictive material is also considered as smart material, which will be discussed in the section of "smart actuator".

Although magnetic actuator can deliver relatively large force, the force induced by mag-

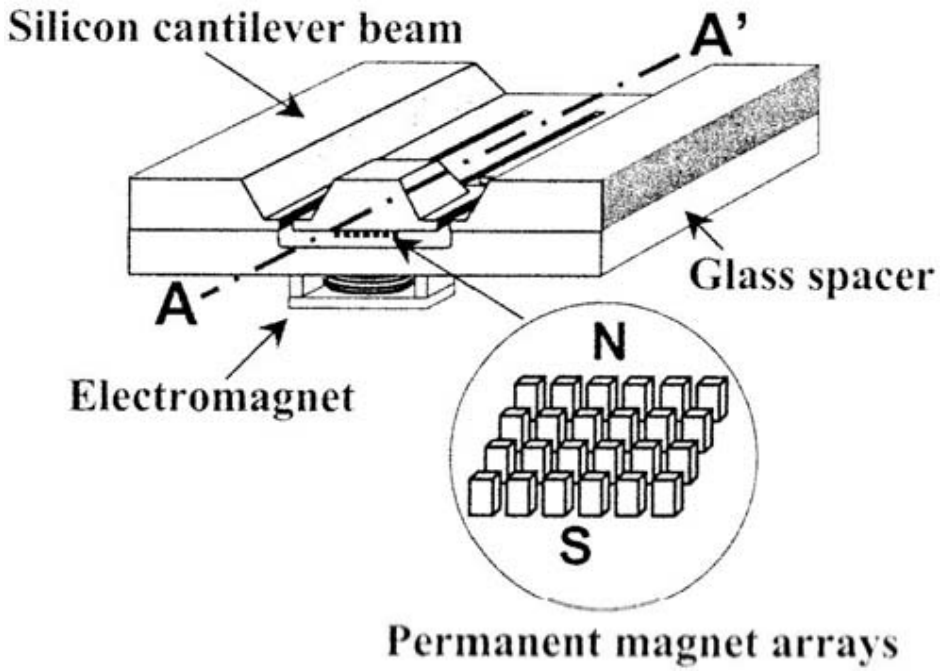

(a)

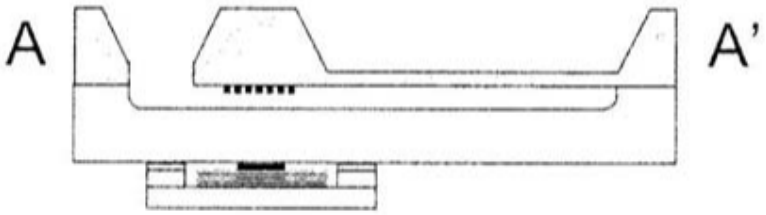

(b)

Figure 2.9: Structure of a cantilever beam microactuator: schematic view and cut view [18].

netic fields scale disadvantageously into the micro scale [98]. Materials with higher magnetic energy density are required, but not all magnetic materials can be deposited and fabricated with MEMS fabrication techniques. Simple fabrication process also need to be developed in order to be compatible with other conventional materials used in MEMS devices.

2.1.4 Piezoelectric Actuator

Piezoelectric effect is the ability of certain materials to generate an electric charge in response to applied mechanical stress. The piezoelectric effect is also reversible, meaning that materials exhibiting the direct piezoelectric effect (the generation of electricity when stress is

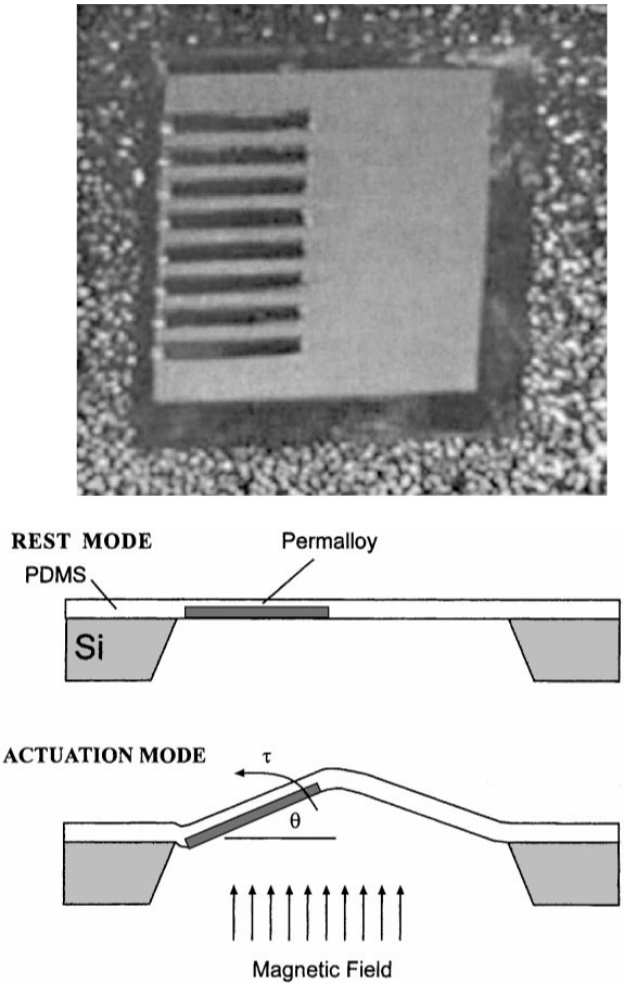

Figure 2.10: A micro-fabricated, membrane-type magnetic actuator driven by external magnetic field [19].

applied) also exhibit the converse piezoelectric effect (the generation of stress when an electric field is applied). Piezoelectric material is belong to smart materials, but since piezoelectric effect was discovered in 1880 [99] and has been widely used in a variety of applications, piezoelectric actuators become a large branch of MEMS actuators.

The maximum force of piezoelectric actuators is typically between 10^{-5} and 10^{-3} N and the maximum displacement between $^{-7}$ and $^{-3}$ m. There is a trade-off between displacement

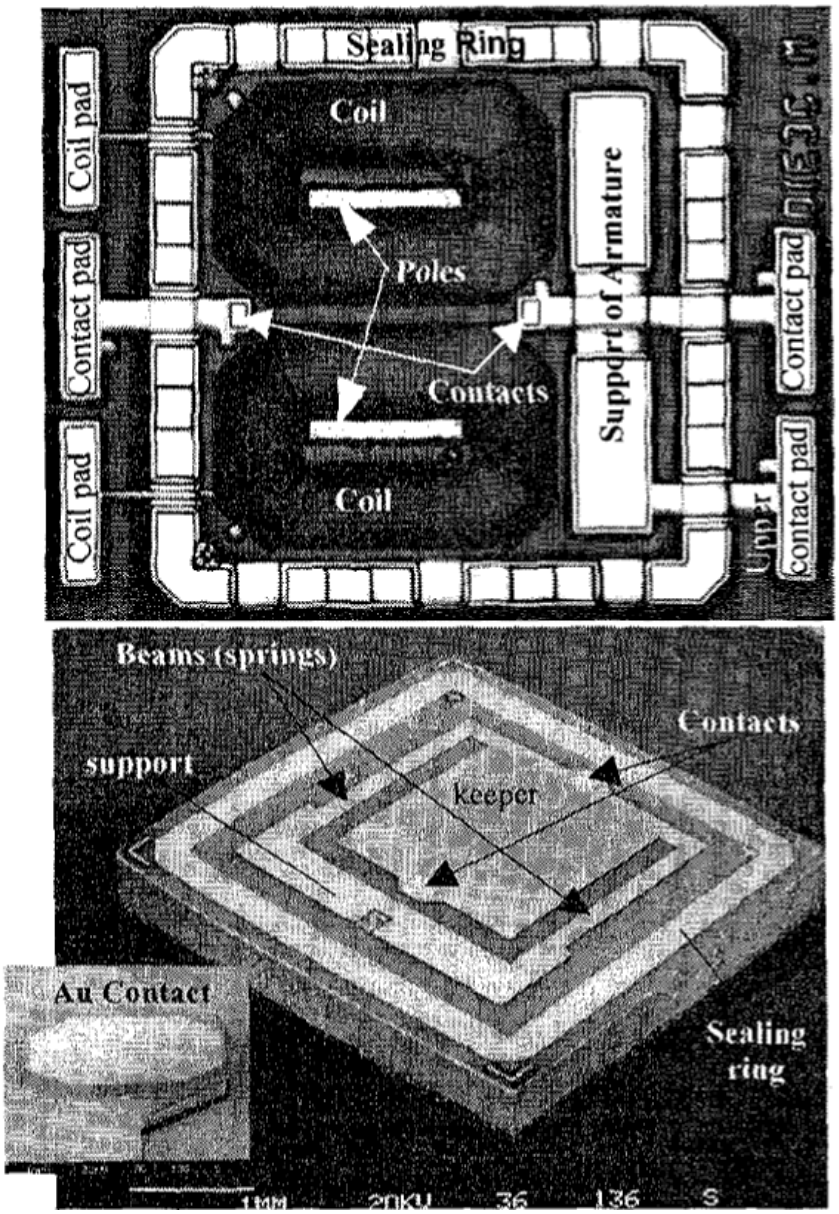

Figure 2.11: A magnetic relay [20].

and output force for piezoelectric actuators, which limit its applications. **Figure** 2.12 shows a lead-zirconate-titanate (PZT) based piezoelectric micro-machined switch [21] that reported a fast switching time of 2 μs at an actuation vatage of ¡40V. An on/off isolation of ¿25 dB was achieved up to 100 MHz. A thin film bulk wave acoustic resonators (FBAR) for wireless applications is shown in **Figure** 2.13. AlN was used as the piezoelectric material, and this resonator can achieve an quality factor over 2500 and a coupling coefficient of 100.

The advantages of piezoelectric actuators are high force (trade-off between force and displacement could be a problem for some applications), high operation speed, and low

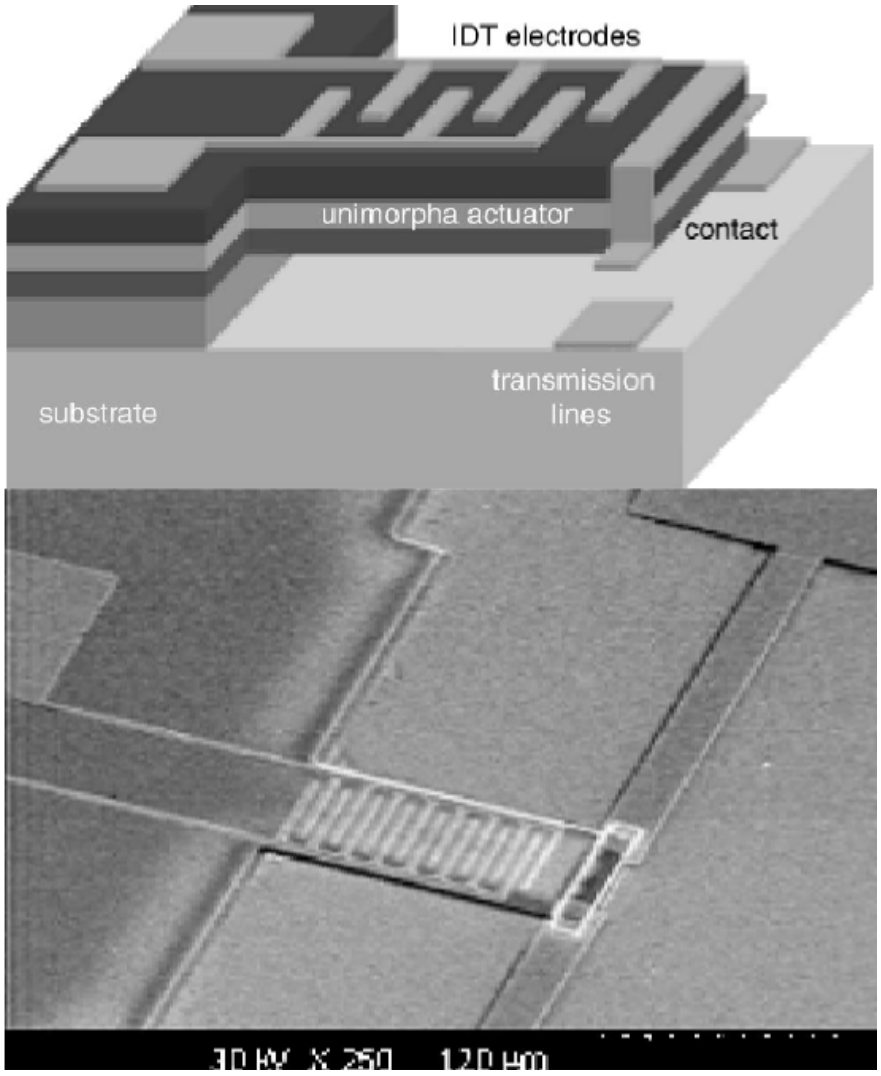

Figure 2.12: Schematic illustration of a PZT based switch and its SEM image [21].

power dissipation. On the other hand, two main challenges for this type of actuator is material challenges and fabrication challenges. Material deposition techniques need to be improved, while process compatibility with IC and piezoelectric requires further exploration.

2.1.5 Smart Actuators

Smart actuators are devices that utilize smart materials' properties to convert applied input to motion. Smart materials, by definition, are designed materials that have one or more properties that can be significantly changed in a controlled fashion by external stimuli, such as stress, temperature, moisture, pH, electric or magnetic fields. Therefore, smart actuator is not independent from other types of micro actuators that have been mentioned in previous sections, and on the contrary it should be included by them. Most common smart materials include piezoelectric materials, shape-memory alloys (SMA), electroactive polymers, and magnetostrictive materials.

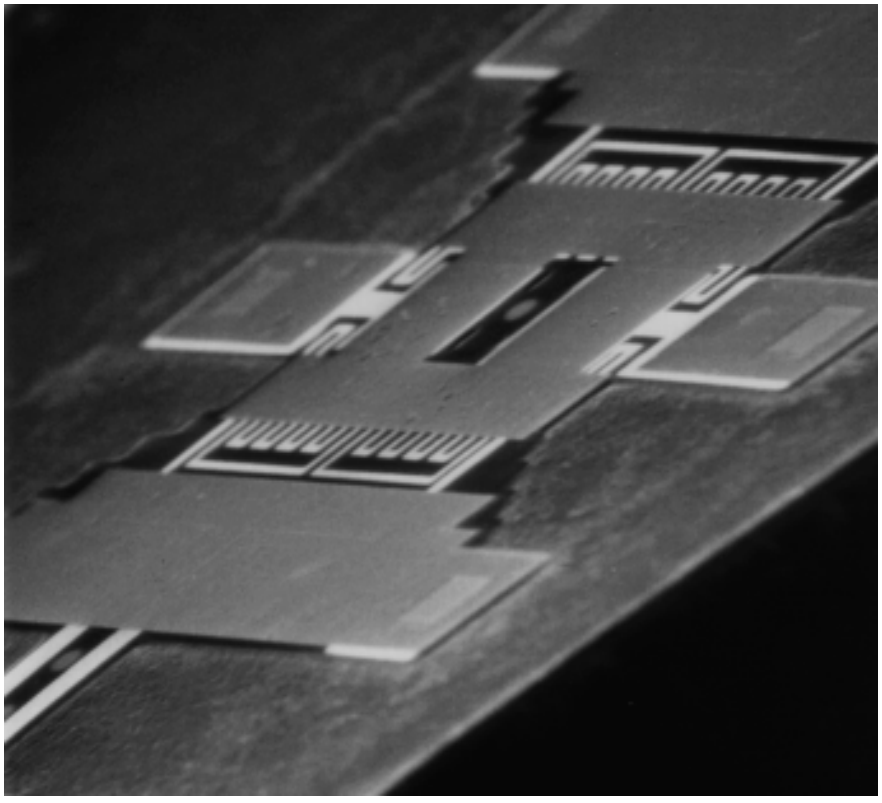

Figure 2.13: SEM image of an FBAR resonator based on piezoelectric effect. [22].

SMAs can change their structure between austenite to martensite upon the temperature. The SMA actuators can offer very high force capacity, as well as moderate displacement. An example of a TiNi SMA-based micro-actuator is shown in **Figure** 2.14. The micro-gripper is able to completely close its fingers making it possible to grab microscopic particles [23]. One weakness of SMA actuators is its functional fatigue that happens because repeated motion of SMA actuators can cause a shift of the characteristic transformation temperatures. This effect may result from a change of micro-structural and functional properties of the material [100].

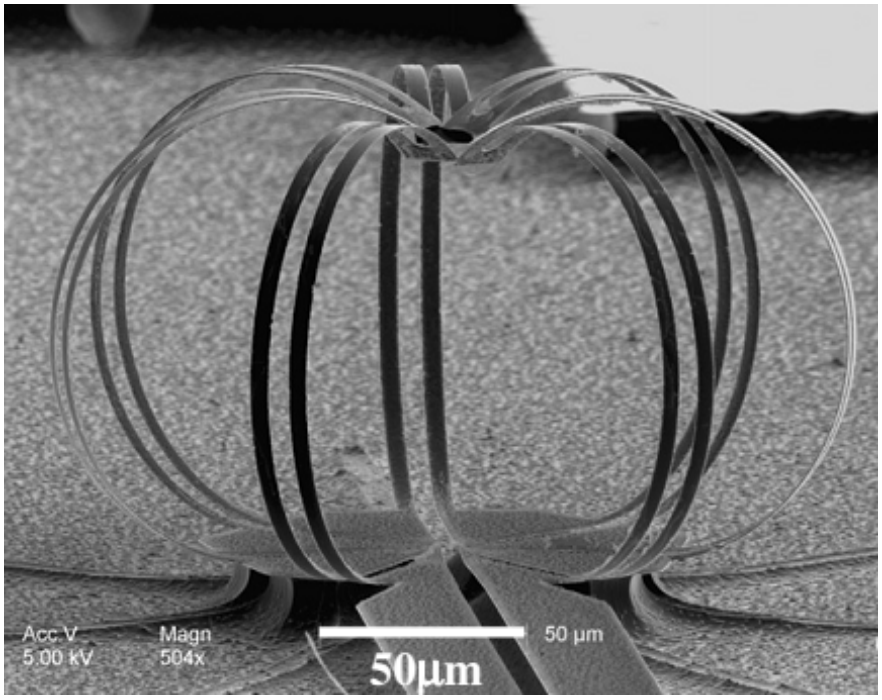

Figure 2.14: An SMA-based micro-gripper under full actuation [23].

Electroactive polymers are polymers that exhibit a change in size or shape when an electric field is applied. Actuators based on electroactive polymers have demonstrated large strains and forces [101, 102]. Meanwhile, this type of actuators also exhibit good performance in variable bioenvironment, which makes it a perfect choice for biomedical applications and artificial muscles [103, 104]. An example of electroactive polymers is shown in **Figure** 2.15, in which a ploymer based actuator is driven inside water.

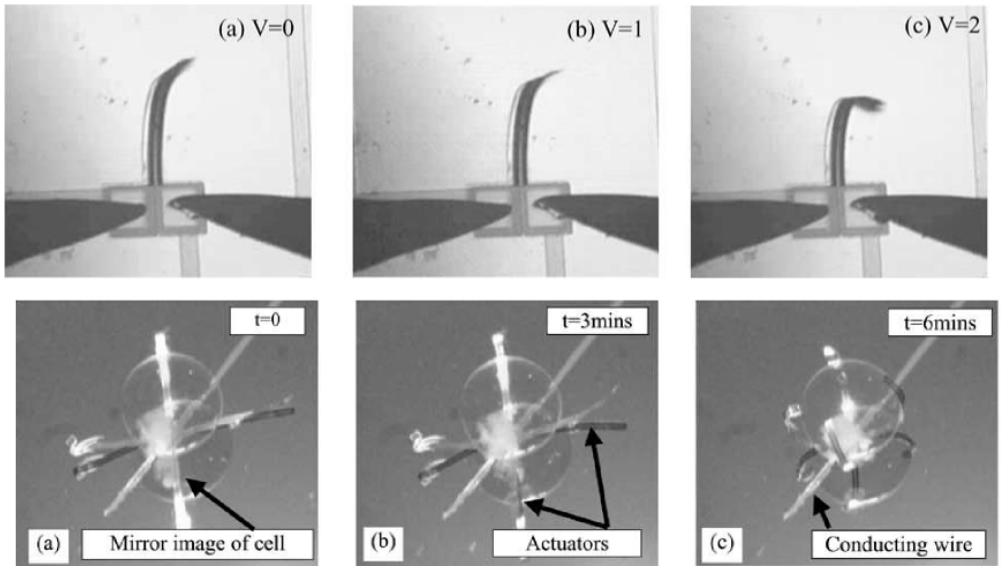

Figure 2.15: Sequence of images showing the motion of an underwater actuator by increasing the water medium. [24].

Magnetostrictive actuators, as one class of magnetic actuators, use magnetostrictive materials to perform deformation under magnetic field [25, 105]. The most common magnetostrictive materials include Cobalt, Terfenol-D, Galfenol, and Metglas 2605SC. These types of complex compounds complicate their deposition as thin films and limit their applicability in MEMS and NEMS applications. **Figure** 2.16 shows a two-dimensional optical scanner that integrated magnetostrictive actuation and piezoresistive detection, in which the magnetostrictive material it uses is a TbFeCoFe multilayer film.

2.2 Vanadium Dioxide

As a smart material, VO_2 undergoes abrupt changes of electrical [37], mechanical [26], and optical [43] properties during its solid-to-solid phase transition at 68 °C. This transition consists two deep correlated transition: electrical (insulator to metal transition (IMT)) and structural (structural phase transition (SPT)), which happen at slightly different temperature [106, 107, 28]. VO_2's transition is a hysteric and fully reversible process. At low temperature the crystal structure of VO_2 is monoclinic, while at temperature above 68 °C the crystal structure transforms to tetragonal or rutile (see **Figure** 1.1). This structure

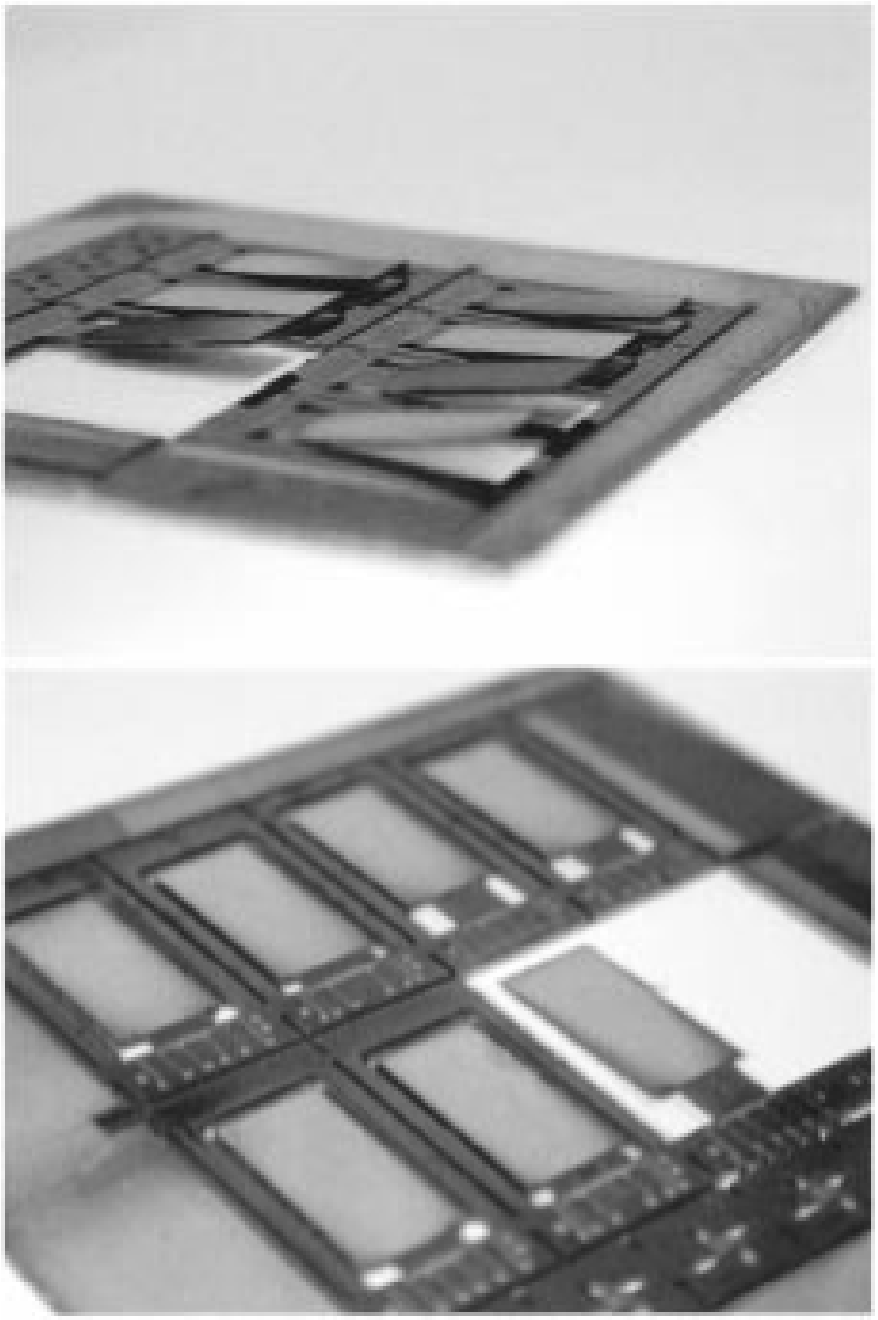

Figure 2.16: A two-dimensional optical scanner based on magnetostrictive actuation [25].

change is the foundation of VO_2 actuators that will be discussed in following section.

It should be noticed that there are other vanadium oxides that can also experience phase transition. However, compared with VO_2, the transition temperatures of these vanadium oxides are further from room temperature (e.g. $-123\,^{\circ}\mathrm{C}$ for V_6O_{13} [108] and V_2O_3 [109], and $280\,^{\circ}\mathrm{C}$ for V_2O_5 [110]). The fact that the transition temperature of VO_2 is so close

to room temperature, is what makes it very suitable for transducer applications. Efforts of reducing transition temperature of VO_2 focus on changing the crystal structure of VO_2 at low temperature slightly. Doped by other elements (e.g. Cr, Ti, W, Fe [111, 112, 113, 114]), the monoclinic structure will be slight deformed by the introduced defects, which is similar to the structural change caused by temperature increase.

2.2.1 Structural and Optical Transition

The structural transition of VO_2 is a transformation process from monoclinic to tetragonal (rutile). During this SPT, the lattice parameters of the crystal unit cell change (shrink in one direction and expand in the other two directions) [28]. Eventually the volume of unit cell increases when crystalline structure change from monoclinic to tetragonal. However, the areas of some planes are reduced. VO_2, grown by pulsed laser deposition (PLD) on amorphous SiO_2 or single crystal silicon (SCS), tends to align its (011) and (110) planes parallel to the substrate (**Figure** 2.17). In these cases, the plane area shrinks when VO_2 crystalline structure transforms from the monoclinic phase to the tetragonal phase. This deformation of structure leads to a structural strain that is about 0.3% [26], which induce the contraction at the interface between VO_2 and substrate. If VO_2 film is grown on SiO_2 or SCS made cantilevers, the cantilevers will bend upwards (see **Figure** 2.18). This is the principle of VO_2 based micro actuators.

The optical transition in VO_2 is considered as a result of IMT [115, 116] since an electronic band structure is strongly connected to the optical constants, and thus, the change of band structure inevitably alter the optical constants, which leads to a variation of extinction coefficient or refractive index [27] (see]figkaki2007optical). Band structure change is shown in **Figure** 2.20. Vanadium (V) ions in VO_2 are located in 3d states, right above the oxygen (O) 2p levels which further divide vanadium states into lower t_{2g} and higher e_g levels. The t_{2g} states split into a $d_{\|}$ state and π^* state, surrounding Fermi energy level. At low temperature, the metallic bond between vanadium ions are affected by adjacent V-O bonds,

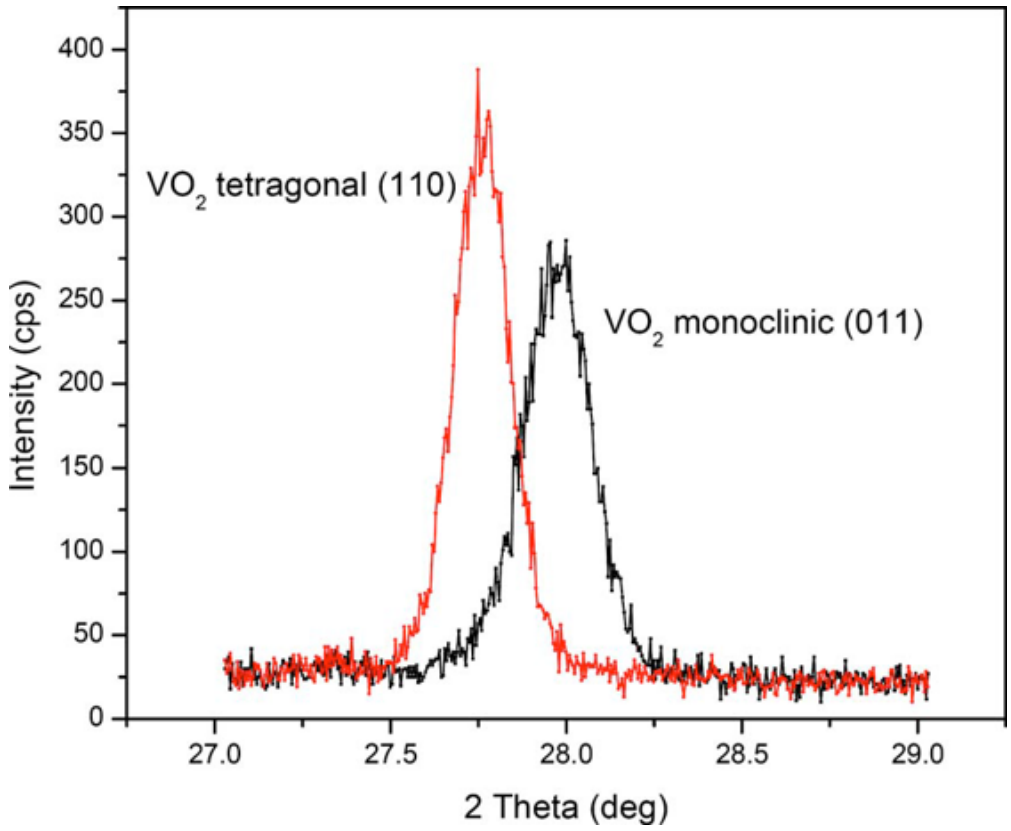

Figure 2.17: XRD scans for VO_2/Si thin film taken at room temperature (monoclinic phase) and above transition temperature (tetragonal phase) [26].

causing a splitting of $d_{||}$ state into a filled bonding and empty antibonding states. Meanwhile, the π^* state moves to higher energy, resulting a band gap about 0.7 eV. At high temperature, O atoms surround the V atoms in an octahedral configuration. The influence of V-O bond only crosses the edge of V-V bond, resulting in the splitting $d_{||}$ states close around Fermi level, and lowering the π^* state energy. The overlap between $d_{||}$ states and π^* states provides VO_2's metallic property at high temperature.

2.2.2 Vanadium Dioxide Synthesis

VO_2 thin films are usually synthesized by means such as chemical vapour deposition (CVD), physical vapour deposition (PVD), and sol-gel method. Efforts on atomic layer deposition (ALD) have also been made. Based on methods used to synthesis, the morphology of VO_2 changes accordingly, affecting characteristics of VO_2 transition. As a common industrial pro-

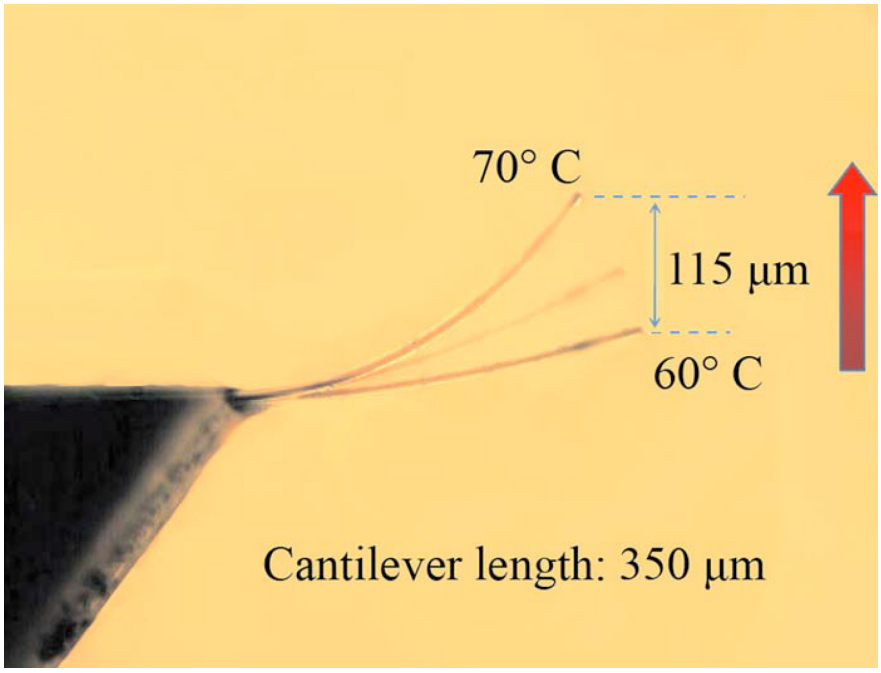

Figure 2.18: Multiple exposure picture of VO_2-coated silicon cantilever during heating [26].

cess for depositing high-quality and high-performance thin films, CVD is also used to deposit VO_2 film. Precursors containing vanadium atoms are introduced into reaction chamber, and by well controlled temperature and pressure vanadium oxide film can grow on the substrate. One example is shown in **Figure** 2.21. Annealing is usually need to facilitate the process that vanadium oxides convert to VO_2 [117, 118, 29, 119].

Sol-gel method has the advantages of low cost, suitability for large area deposition, and the feasibility of metal doping. It consists of preparation of precursor solution, transformation into sol, and into gel. After hydrolysis, condensation, and thermal treatment, thin film can be deposited on the substrates. The sol-gel approach for VO_2 deposition is also a low temperature process, which allows dopant can be introduced in the sol and the final VO_2 film [120, 121, 122, 123].

PVD methods can be divided in two main classes: sputtering and PLD. Sputtering is one of the most common physical vapour deposition processes for growing vanadium dioxide thin films. Both DC and RF sputtering were realized and studied [124]. Since RF sputtering has advantages on insulating oxides over DC sputtering, RF sputtering become a better

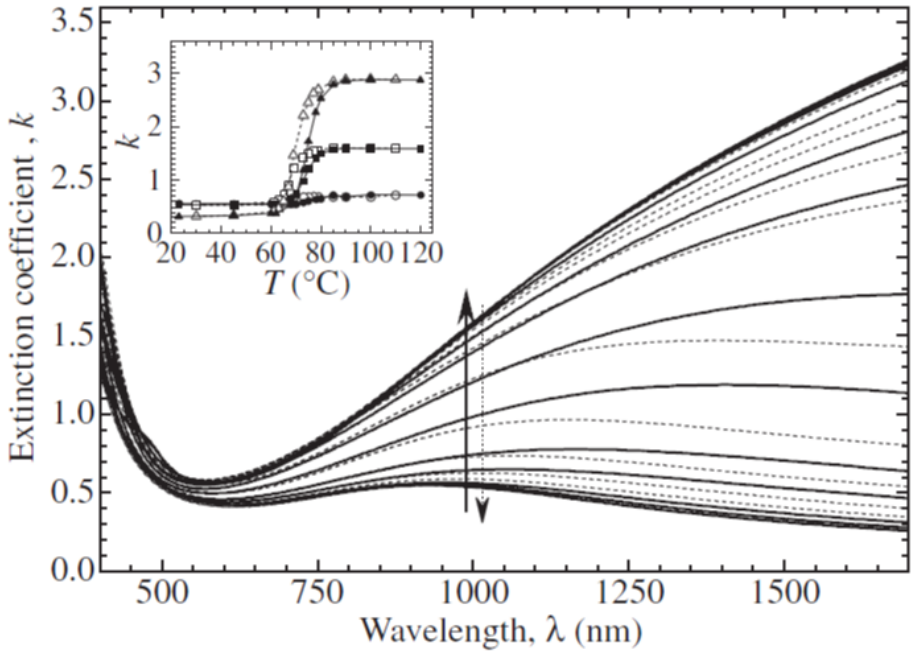

Figure 2.19: Wavelength dispersions of (a) refractive index and (b) extinction coefficient at various temperatures between 25 °C and 120 °C. Solid and broken curves indicate the data obtained during the rise and drop in temperature, respectively. The insets show the temperature dependences of the optical constants at wavelengths of 500, 1000, and 1500 nm. Closed and open symbols indicate the data obtained during the rise and drop in temperature [27].

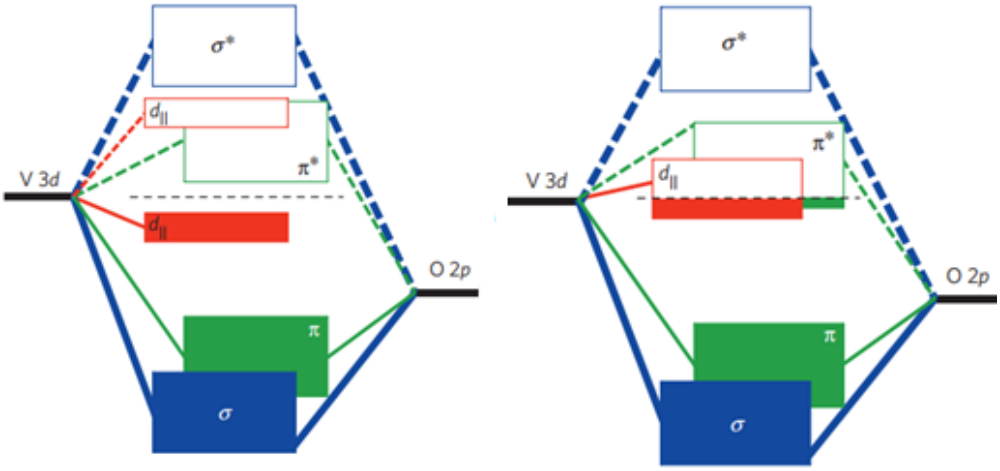

Figure 2.20: Schematic band diagrams for VO2 [28].

option (although similar qualities were obtained in both cases). The sputtering deposition of VO_2 was further improved [125, 126], and nanocrystalline VO_2 has been deposited by RF

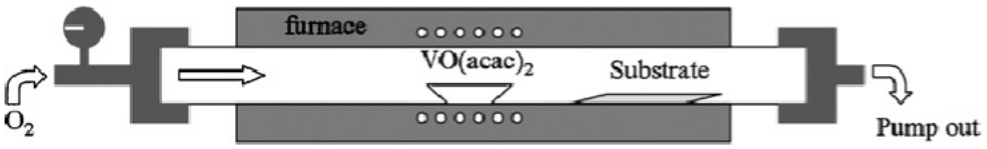

Figure 2.21: Schematic diagram of horizontal alumina tube furnace for growth of vanadium oxides [29].

sputtering [127, 128].

PLD is another very popular way of VO_2 synthesis, which provide very good quality of VO_2 thin film. The thickness of VO_2 can be well controlled by adjusting the deposition time, which makes nanoparticle fabrication possible [129]. The VO_2 thin films in this work are all deposited by PLD. The setup of PLD system is shown in **Figure** 2.22. The substrate was placed into a vacuum chamber with gas pressure of oxygen at 20 mTorr. A metallic vanadium target 2 inches apart from the sample was ablated by focused excimer laser pulses with an intensity of 352 mJ (fluence of 2 J/cm2) and a frequency of 10 Hz. A ceramic heater used to heat the sample was maintained at 595 °C through 25 minute deposition. Following the deposition, 30 minute annealing process was performed with the same deposition conditions. To determine the quality of the VO_2 film, the resistance of the VO_2 film was measured as a function of temperature which cycled between 30 °C to 100 °C. About three order drop in film resistance was observed, which indicates that the thin film is in fact good quality of VO_2.

2.3 Single-Wall Carbon Nanotubes

Carbon nanotube can be viewed as a sheet of graphene wrapped up into a tube, single-walled carbon nanotube (SWNT), as shown in **Figure** 2.23. In addition, multi-walled carbon nanotube (MWCNT) can be made of multiple graphene sheets rolling together. The diameter of SWNT can vary from sub-nm to several nanometers, while a MWCNT can have a diameter up to a few hundred of nanometers. SWNTs with their unique electrical and optical properties have drawn great attentions in academic society. There has been in-

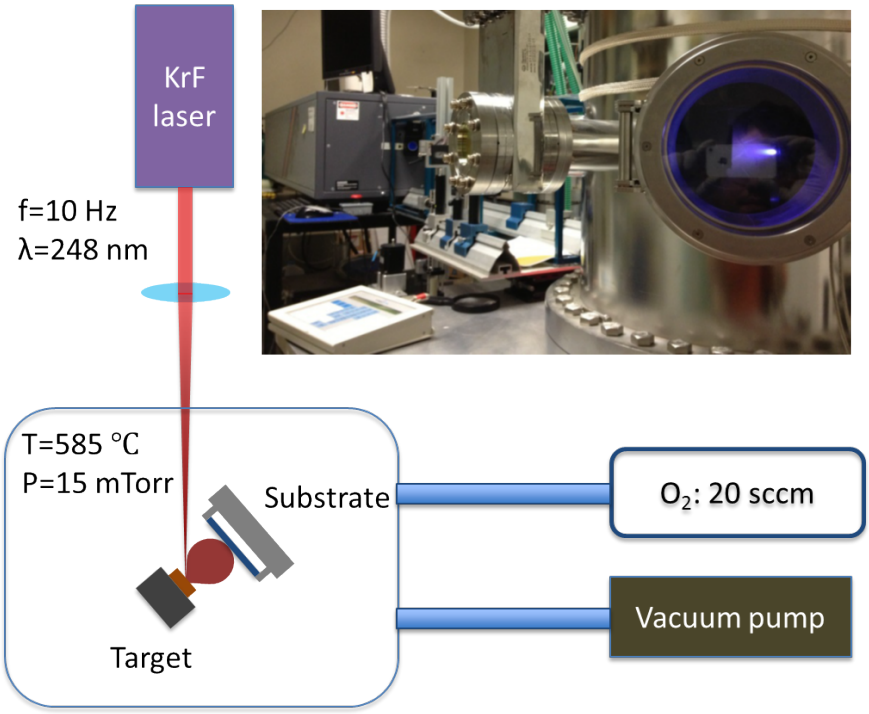

Figure 2.22: Schematic diagram of PLD system for VO_2 deposition.

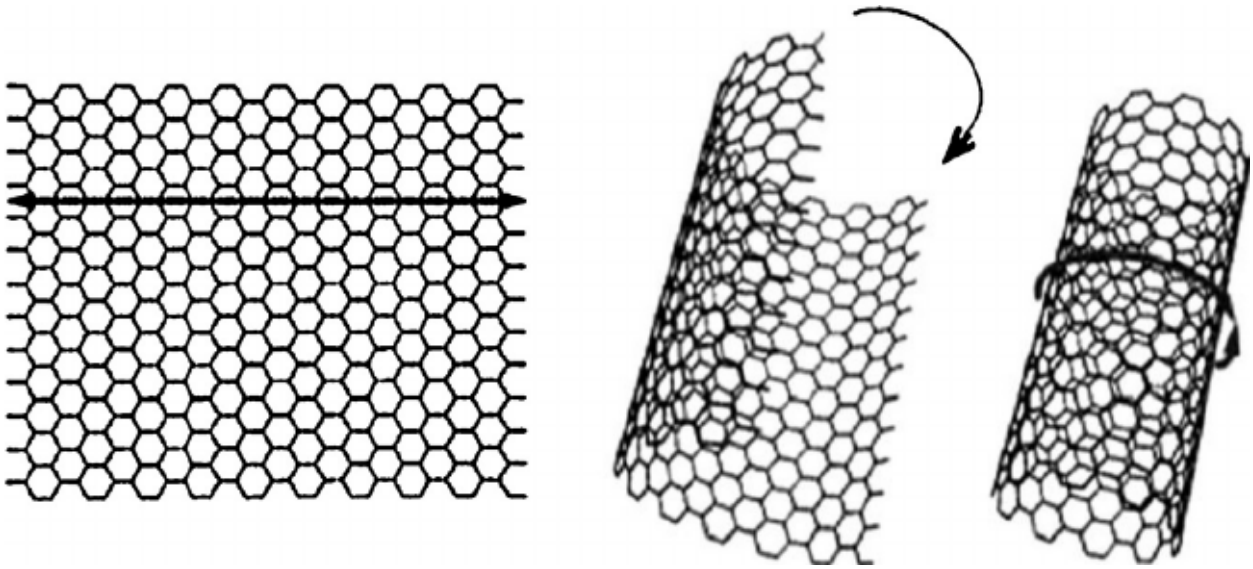

Figure 2.23: Schematic illustrating a layer of graphene lattice rolled into an SWNT [30].

tense researches exploring their potential applications such as electronics and biomedical [130, 131, 132, 133, 134, 135, 136, 137, 138]. SWNT can be characterized by its structure and chirality, which have important impacts on its electrical and optical properties. Recently, enormous investigation efforts on chirality-controlled SWNT synthesis and tre-

mendous achievements made in the nanotube growth field make use of SWNTs with certain chirality distribution possible. The devices proposed in this work also utilize this advantages to achieve wavelength selective actuators.

2.3.1 SWNT Synthesis

The properties of SWNT are strongly dependent on their structure, orientation, and length of the carbon nanotube. Thus, SWNT techniques have been focused on high yield and high quality during the past several decades. Several major methods will be described in this section including arc discharge, laser ablation and chemical vapour deposition (CVD).

Arc discharge was the first method used to synthesis carbon nanotubes [139, 140], in which two graphite electrodes were separated by a small distance in comparison with methods of C60 synthesis where electrodes were in contact. This method was improved later by introduce high pressure helium [141]. Despite the developments and higher yield of SWNTs produced by arc discharge [142, 143, 144], it is still a costly and complicate method compared with others. An arc discharge apparatus is shown in **Figure** 2.24.

laser ablation is another effective way to synthesize large amount of SWNTs (shown in **Figure** 2.25). A graphite target was placed in the way of a focused laser beam. While the high energy laser pulses hit target and ablate carbon molecules, a inert gas flow (e.g. helium flow) carried to the cooled collector. This process happened in a furnace at 1200 °C. The growth of MWCNTs by laser ablation was first demonstrated [145, 146], and later SWNTs were synthesized by this method with graphite targets mixed with metallic elements [146, 147, 148]. The quality of the SWNTs produced by laser ablation is higher than that made by arc discharge.The disadvantages of this method catalyst nanoparticles mixed with SWNT during collecting. Further treatment is required to remove them.

With the advantages of uniform and large area deposition, CVD technique is also applied to CNT synthesis. **Figure** 2.26 is a schematic of a CVD system for nanotube synthesis. Silicon wafer with catalyst layer on top is placed on a hot stage at temperature between

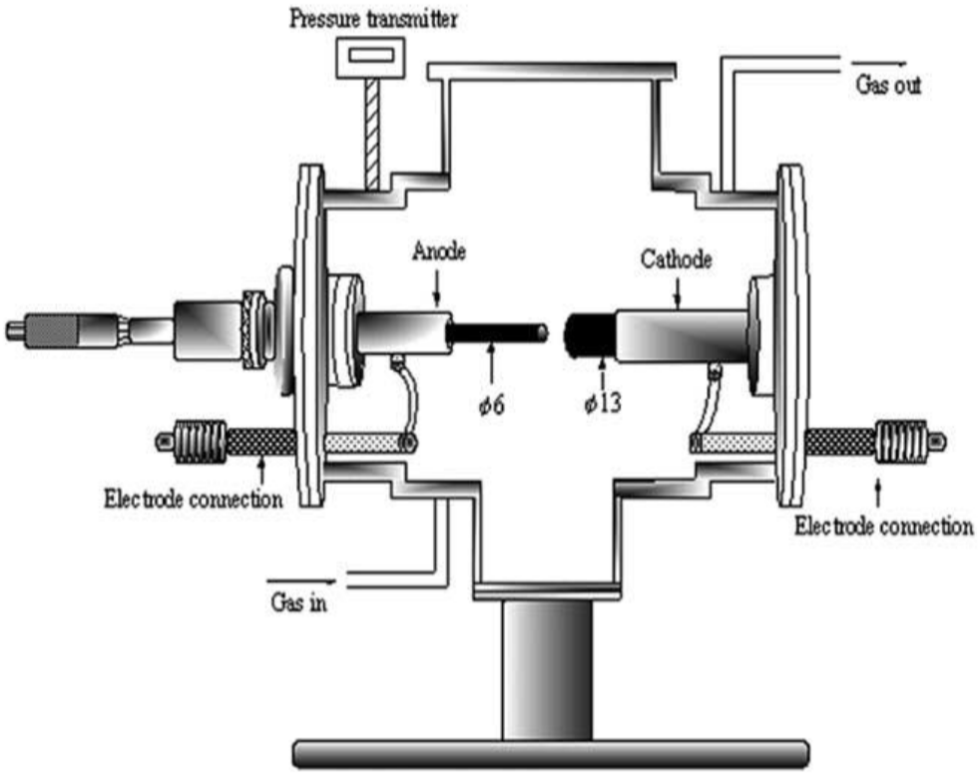

Figure 2.24: Schematics of the arc-discharge apparatus for nanotube synthesis [31].

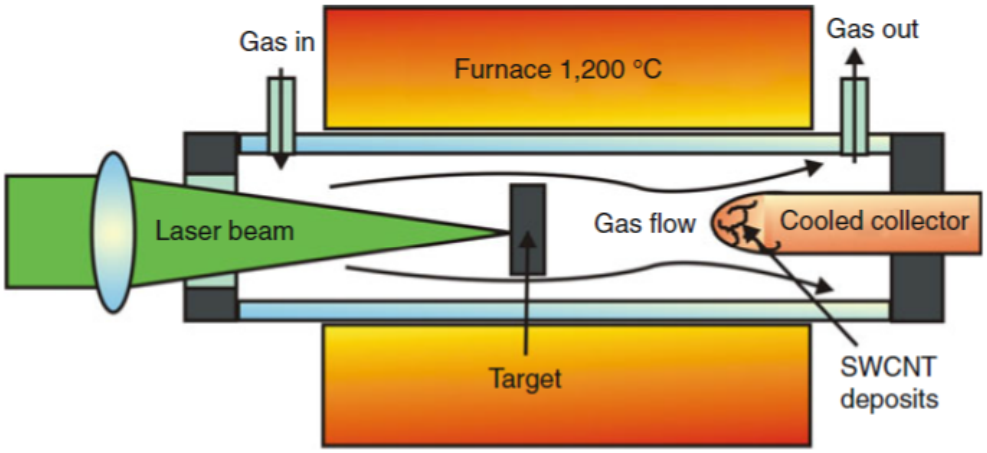

Figure 2.25: Schematics of the laser ablation apparatus for nanotube synthesis [32].

400 °C to 1000 °C. Acetylene or methane gas with a small portion of hydrogen gas flow over silicon wafer, where carbon containing gas decomposes and form carbon nanotubes. Additionally, controlled synthesis of the orientation, diameter, and electronic property has been achieved [149, 150, 151, 152, 153, 154, 155, 156, 157, 158].

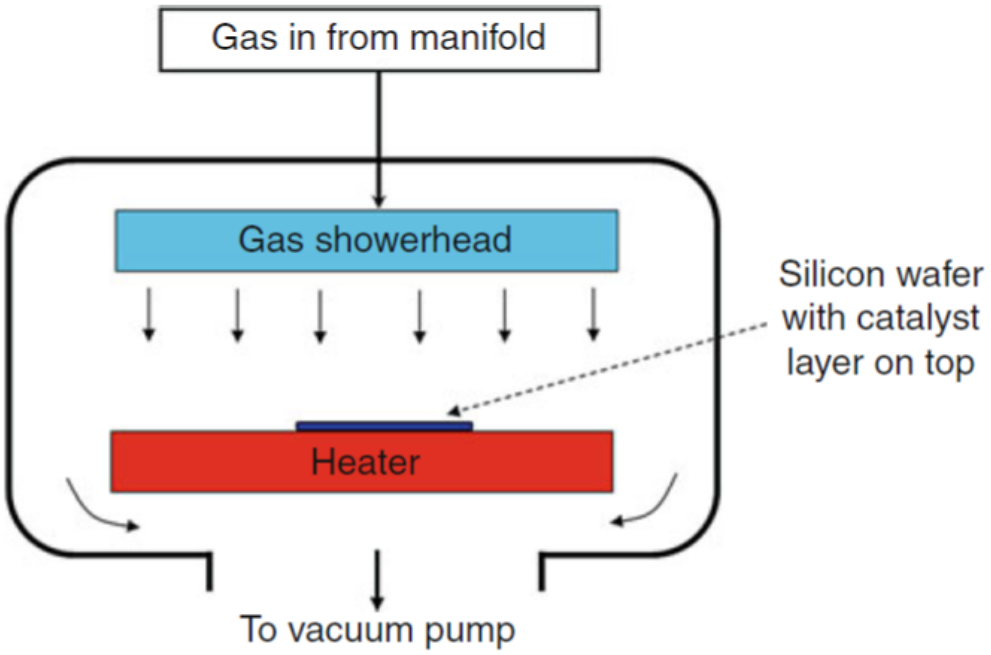

Figure 2.26: Schematic of a CVD system for nanotube synthesis [32].

2.3.2 Chirality of SWNT

As mentioned at the beginning of this section, carbon nanotubes can be pictured as a graphene sheet rolled into a tube. Hence, the geometry of nanotube can be uniquely determined by the chiral vector (in which direction the graphene sheet is rolled up) of original hexagonal graphene lattice (see **Figure** 2.27). The chiral vector (n, m) is defined as $\vec{C} = n\vec{a}_1 + m\vec{a}_2$ where n and m are integers corresponding graphene vector $\vec{a}_1$ and $\vec{a}_2$. As one example of the affects of chirality on SWNT properties, **Figure** 2.28 shows how electric property of SWNT is determined by its chirality. The condition for the metallic nanotube is: 2n+m=3q (q: integer), or (n-m)/3 is integer.

2.3.3 Optical Property of SWNT

The optical properties of SWNTs are determined by their energy band structures which strongly depend on their diameter and chiral angle. Transitions between valence and conduction bands are only allowed between states that locate symmetrically with respect to

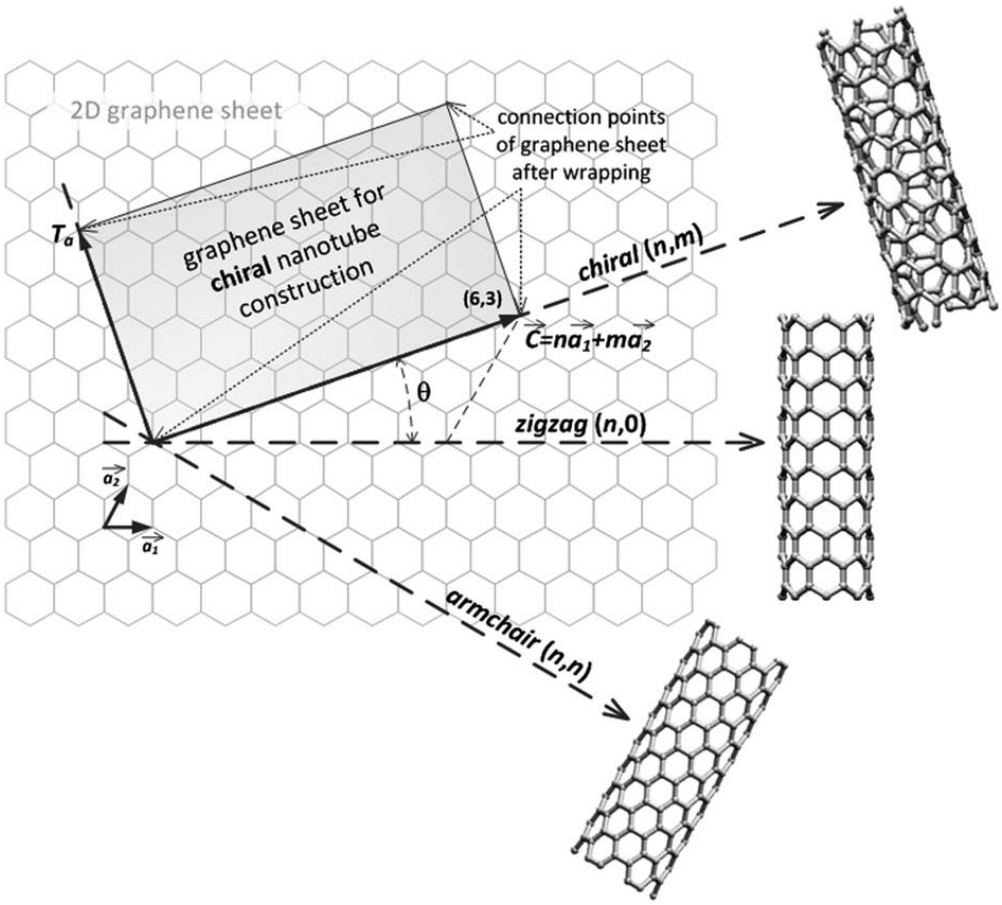

Figure 2.27: The principle of CNT construction from graphene sheet along the chiral vector $\vec{C}$ [33].

the Fermi level, which are denoted E_{ii} (i=1,2,3,...) (see **Figure** 2.29). Light absorption happens when light is resonant with E_{ii} energies of different chiralities. **Figure** 2.29 also indicates a sharp state densities of the bands, which should lead to an absorption spectrum with sharp peaks. However, the typical absorption spectrum often shows an broard peaks. This is because most nanotube samples include a varity of (n, m) chirality nanotubes, whose peaks combine together and become a broad peak. For single chirality nanotubes, the absorption spectra show relatively sharper peaks and slightly different peak positions (shown in **Figure** 2.30). This tunable absorption spectrum of SWNT provides a possibility of wavelength selective devices citezhang2015bolo, zhang2014 including photo-thermal actuators that is proposed in this work.

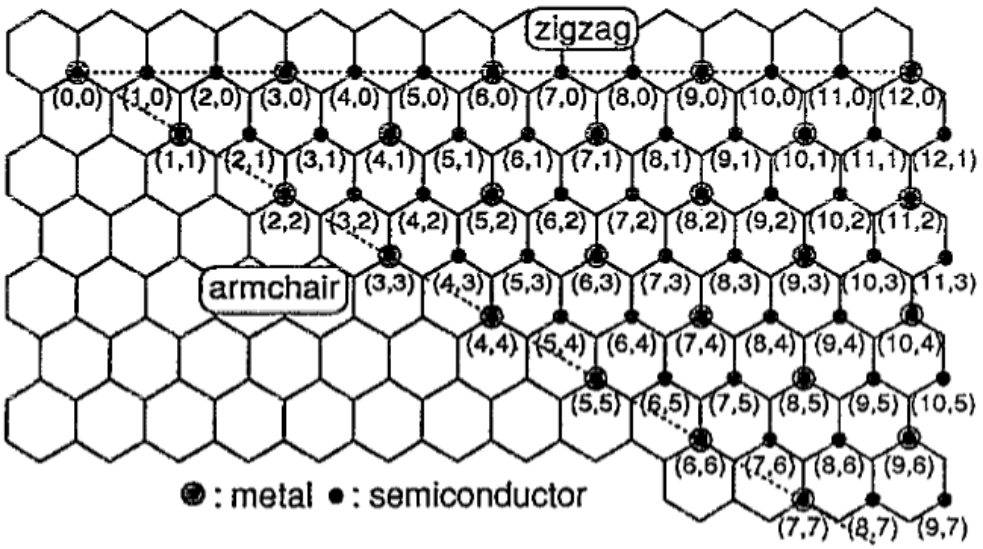

Figure 2.28: Possible vectors for chiral nanotubes. The circled dots and dots, respectively, denote metallic and semiconducting behavior for each nanotubes [34].

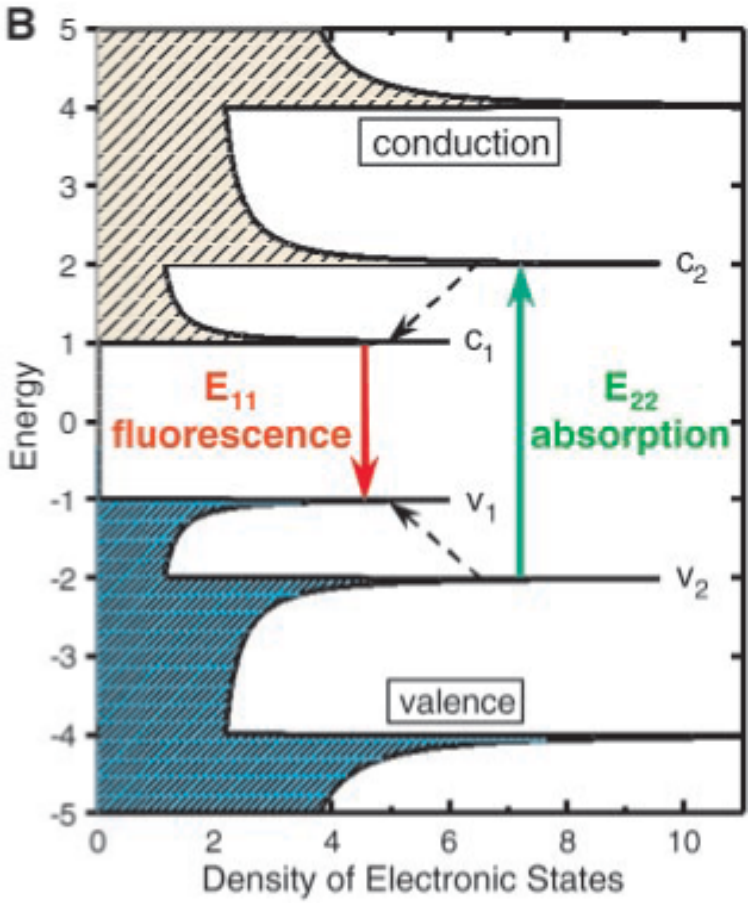

Figure 2.29: Schematic density of electronic states for a single nanotube structure [35].

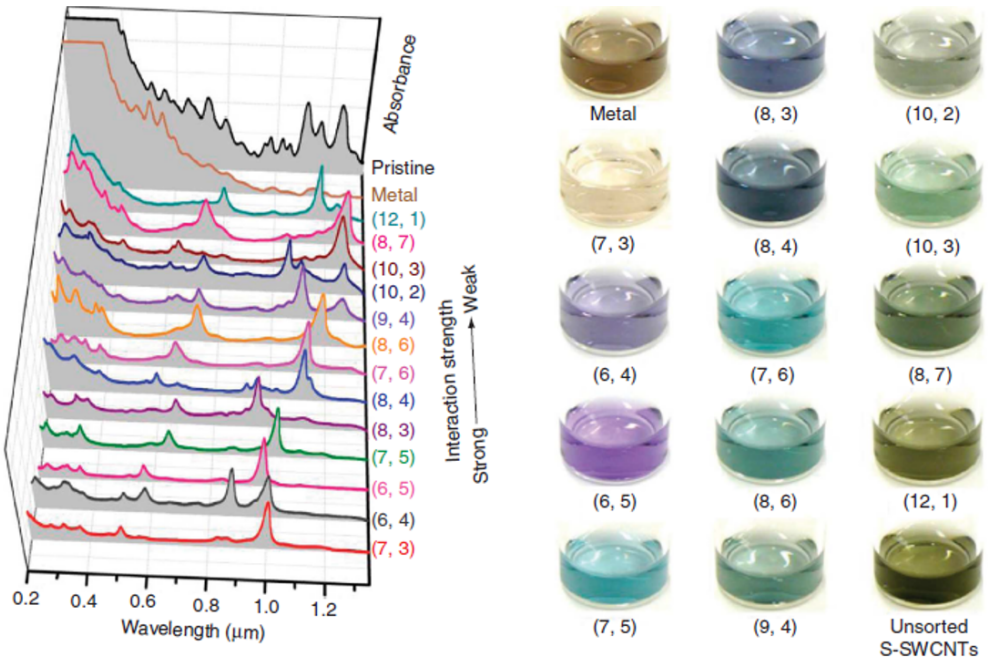

Figure 2.30: 13 species of single-chirality SWNT dispersion solutions (right) and absorption spectra of the dispersions [36].

2.4 Summary

In this chapter, a comprehensive background on micro-actuator mechanisms, vanadium dioxide and single-wall nanotubes is presented. The discussion on micro-actuators includes the most common mechanisms, such as thermal, electrostatic, magnetic , piezoelectric, and smart materials-based actuators. The transition of VO_2 is discussed in detail including structural and optical transitions, suggesting that VO_2 is a good candidate for photo-thermal actuator applications. Synthesis methods of VO_2, such as CVD, sol-gel ,and PVD, are also presented. Lastly, SWNT is introduced from the aspects of synthesis methods, chirality, and optical property. The tunable light absorption peaks based on chirality shows great potential of development of wavelength selective devices.

CHAPTER 3

FABRICATION METHODS OF SWNT THIN FILM

In this chapter, details about the fabrication methiods of SWNT will be presented including vacuum filtration of SWNT solution, SWNT thin film transfer, and the patterning of SWNT thin film. Methods of processing SWNT have been widely developed in the last decade, but not all of them are compatible with VO_2 fabrication process. The work that has been done here is to find the compatible way to fabricate SWNT thin film, film transfer process and patterning method without impairing the quality of VO_2.

3.1 Vacuum Filtration of SWNT Solution

The direct growth of carbon nanotubes on wafers, using methods such as arc discharge, laser ablation, and CVD deposition, are typical in violent conditions (e.g. high temperature above 600 °C and reactive chemical environment), which will inevitably alter the quality of VO_2. Therefore, a vacuum filtration method is used here to avoid this problem. All SWNT films used in this work were prepared by vacuum filtration.

Vacuum filtration is a technique for separating a solid product from a solvent or liquid reaction mixture. The mixture of solid and liquid is poured through a filter paper in a Buchner funnel. The solid is trapped by the filter and the liquid is drawn through the funnel into the flask below, by a vacuum. The vacuum filtration setup used to form 1 inch diameter SWNT thin film is shown in **Figure** 3.1. A vacuum pump will be connect to the outlet of flask to provide negative pressure during filtration. The membrane that is used in this work is made of mixed cellulose esters (see **Figure** 3.2), which can be dissolved by acetone vapour. Key parameters of such membranes include pore size and water flow rate. The principles of membrane selection are to have small enough pore size to block the SWNT particles and relatively high water flow rate to get quick filtration rate.

There are three types of SWNT solution used in this work, unsorted, semiconducting, and

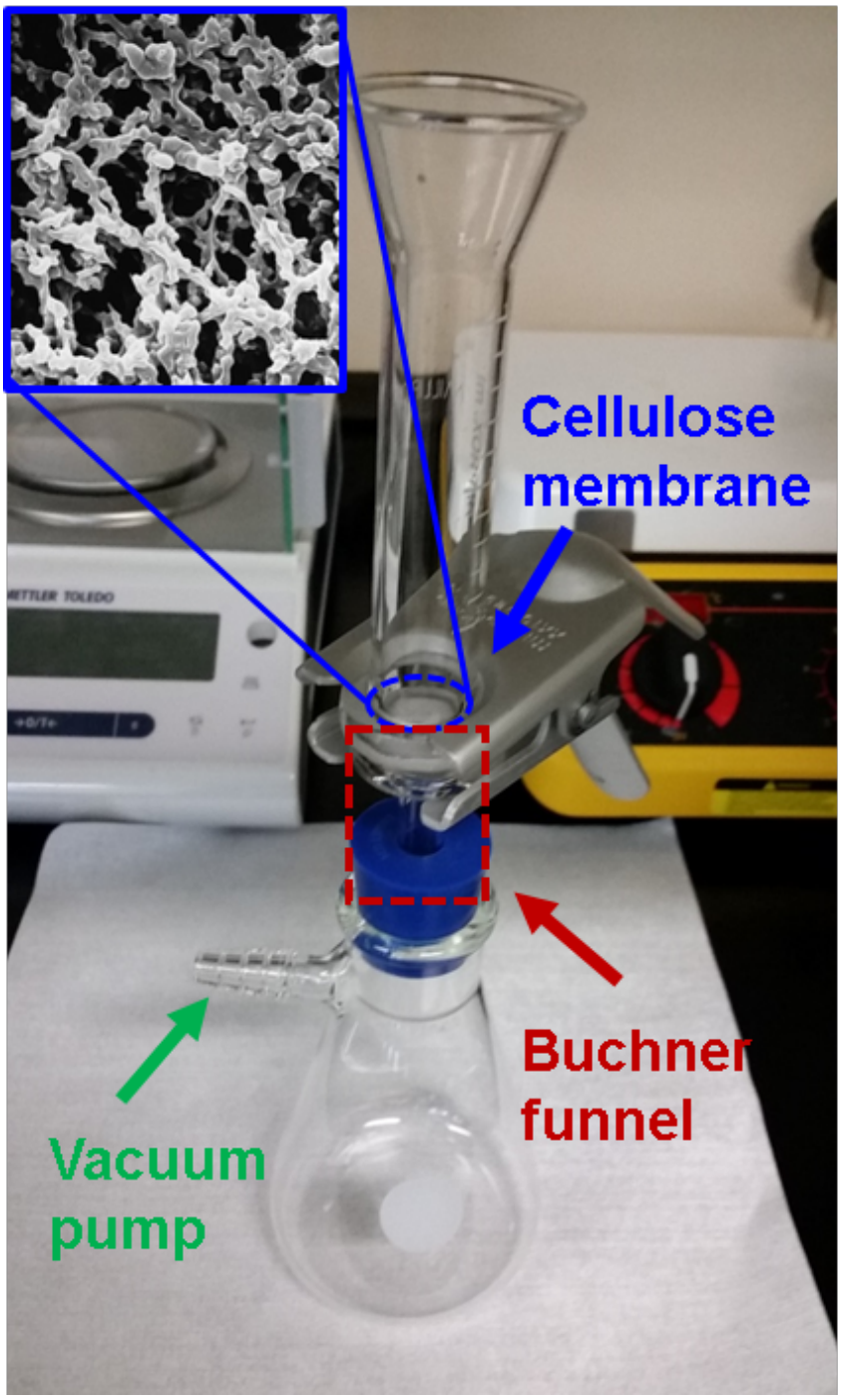

Figure 3.1: The vacuum filtration setup used to form 1 inch diameter SWNT thin film.

metallic SWNT solution. The metallic and semiconducting SWNT (mSWNT & sSWNT) solution was bought from NanoIntegris with a purity of 95% (diameter 1.2-1.7 nm) and a concentration of 0.01 mg/ml, and the 0.01 mg/ml unsorted SWNT (uSWNT) solution was

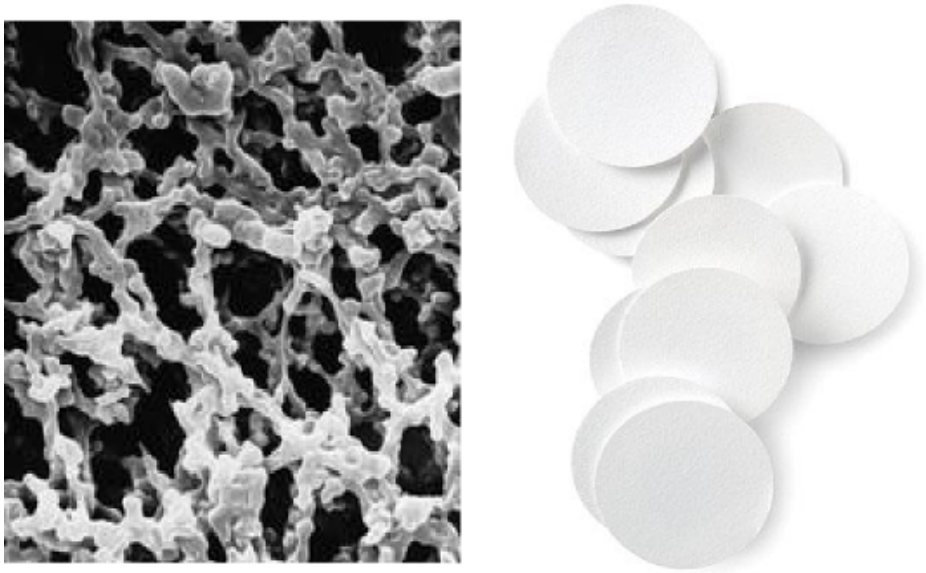

Figure 3.2: The mixed cellulose esters membrane and its SEM surface image.

made following, in general, the same processes in [5]. Purified SWNT powder purchased from Cheap Tube Inc. (Purity $> 99wt\%$, diameter 0.8-1.6 nm, length 3-30 μm), was mixed with 2% sodium deoxycholate as surfactant. An overnight sonication was performed to completely dissolve the SWNT powder. Then, 10 minute of centrifuging with 13,000 rpm rotation speed helped to remove large SWNT aggregates and non-SWNT impurities. The membrane used to filter SWNT solution are 2.5 mm diameter cellulose membranes purchased from Millipore Inc. To achieve best filtration, membranes with different pore size are used to filtrate metallic and semiconducting solution (pore size 0.025 μm), and unsorted SWNT solution (pore size 0.45 μm). The thickness of SWNT films can be controlled by the amount of solution used for filtration. The relation between solution volume and film thickness is shown in **Figure** 3.3.

The filtration procedure contain following step: **1.** Pour SWNT solution needed into funnel and add DI water if the volume of solution is low; **2.** Turn on the pump until the solution has been completely drained; **3.** Add about 10 ml DI water to rinse surface of the membrane in order to clean surfactant residue. The thickness of SWNT thin fi

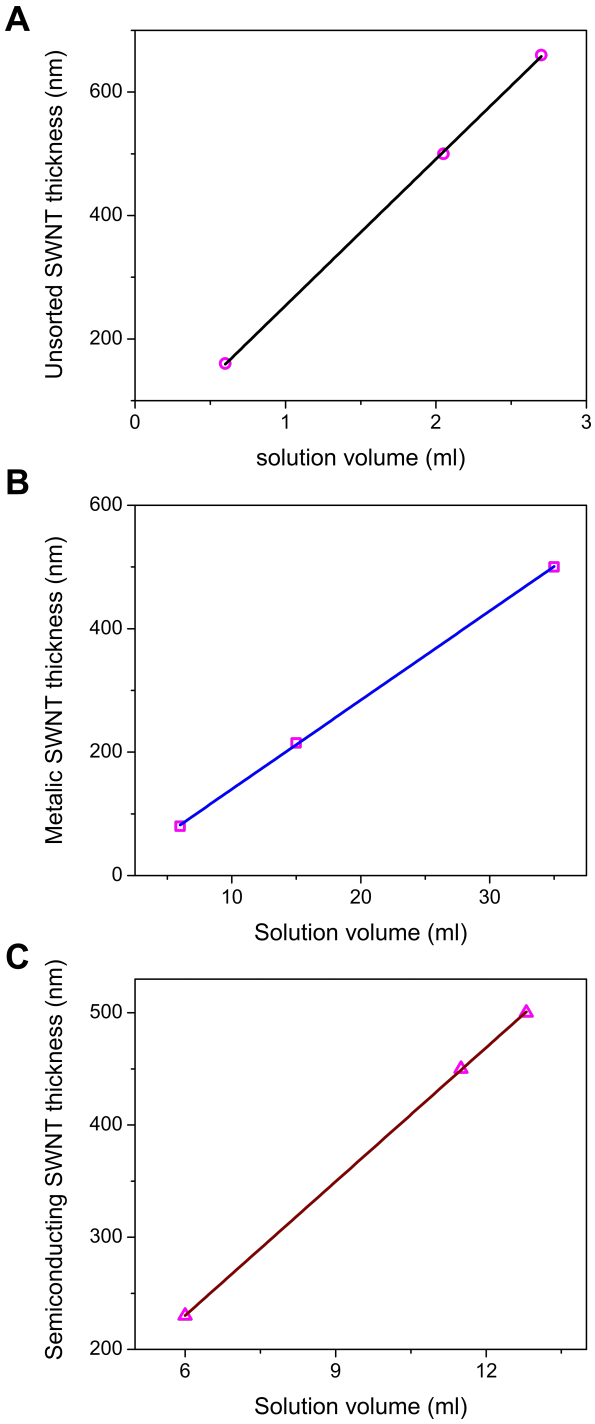

Figure 3.3: The SWNT film thickness versus the volume of SWNT solution used for vacuum filtration. The concentration of uSWNT (A), mSWNT (B), and sSWNT (C) solution is 0.5 mg/ml, 0.01 mg/ml, and 0.01 mg/ml, respectively. The thickness of the SWNT thin film can be readily controlled by adjusting the amount of SWNT solution.

lm can be precisely controlled by adjusting the concentration and the amount of solution used for filtration. The membrane after filtration is shown in **Figure** 3.4.

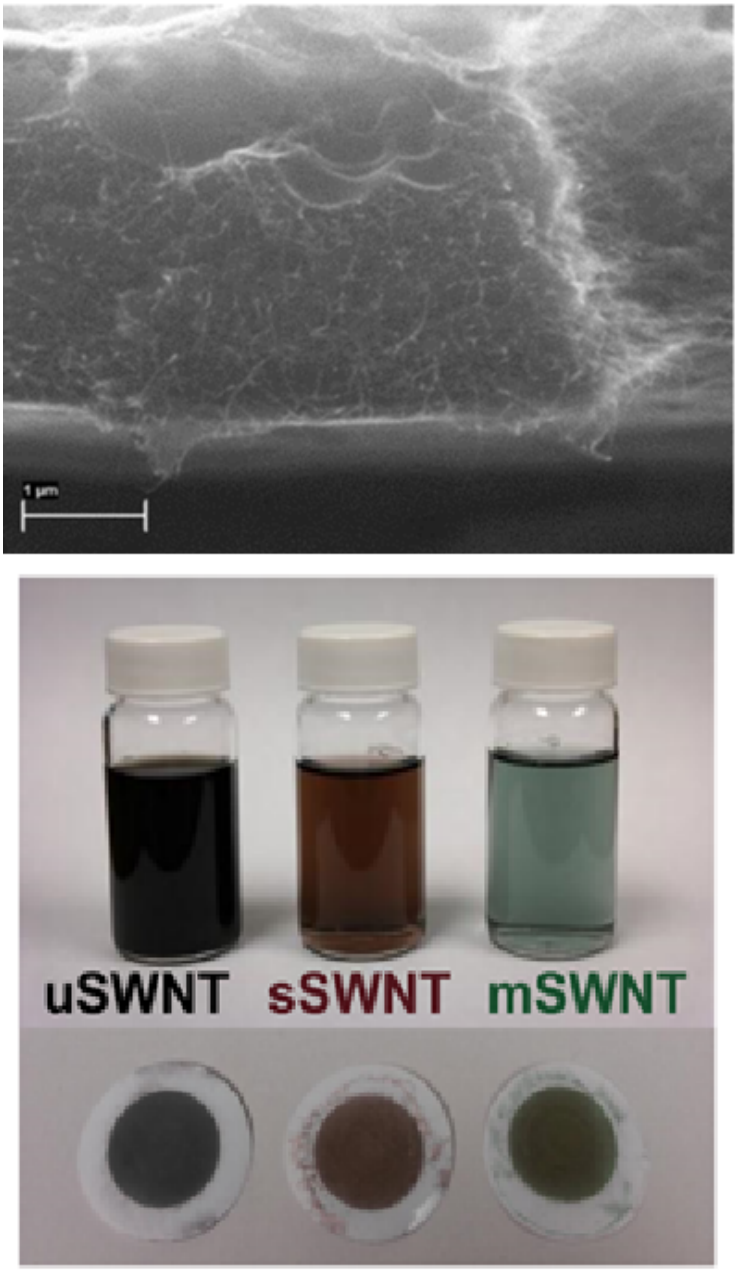

Figure 3.4: The membrane fliter with SWNT on top and the SEM surface image of the SWNT.

3.2 SWNT Thin Film Transfer

Given the SWNT membrane made by vacuum filtration, a success transfer process is used to transfer SWNT film on VO_2 surface wafer and remove the mixed cellulose esters membrane. VO_2 surface is intrinsicly hydrophilic, while SWNT has hydrophobic surface property. This difference make them hard to attach with each other. In order to obtain good adhesion between SWNT and VO_2, surface functionalization was performed by immersing the target substrate into poly-L-lysine solution for 5 minutes. Then, the cellulose/SWNT membrane was attached to VO_2 surface with SWNT side facing towards the substrate. Several drops of deionized (DI) water were used to keep the piece of membrane in the desired position. Acetone bath was used to transfer SWNT film on VO_2 surface wafer and remove the mixed cellulose membrane. The substrate was placed up-side-down in a beaker containing liquid acetone on a hotplate set to 70 °C (see **Figure** 3.5). The wafer is placed 1 inch above the surface of acetone solvent. After about 1 hour acetone vapour bath, cellulose membrane was dissolved, leaving only SWNT film on the substrate. The transfer process was completed by briefly rinsing the sample with acetone, isopropanol (IPA), and then blowing dry.

3.3 Patterning of SWNT Thin Film

Plasma etching is one of the most popular ways to pattern CNT film. In this work, we use O_2 plasma to effectively etch and pattern SWNT. Although a varity of plasma etch recipe has been proven to be effective, the O_2 plasma etching process has been tested to be compatible with VO_2. **Figure** 3.6 illustrates the procedure of patterning. A SWNT and VO_2 coated wafer went through a conventional photo-lithography process, in which photoresist s1818 is used to form the pattern. It is well known that O_2 plasma etch is also effective to most of photoresist, and the etching rate of SWNT film in this work is about 40 nm/min that is comparable to the etch rate of photoresist. Thus, a thicker photoresist layer is formed (>1 µm), while the maximum thickness of SWNT film that has been processed is 500 nm.

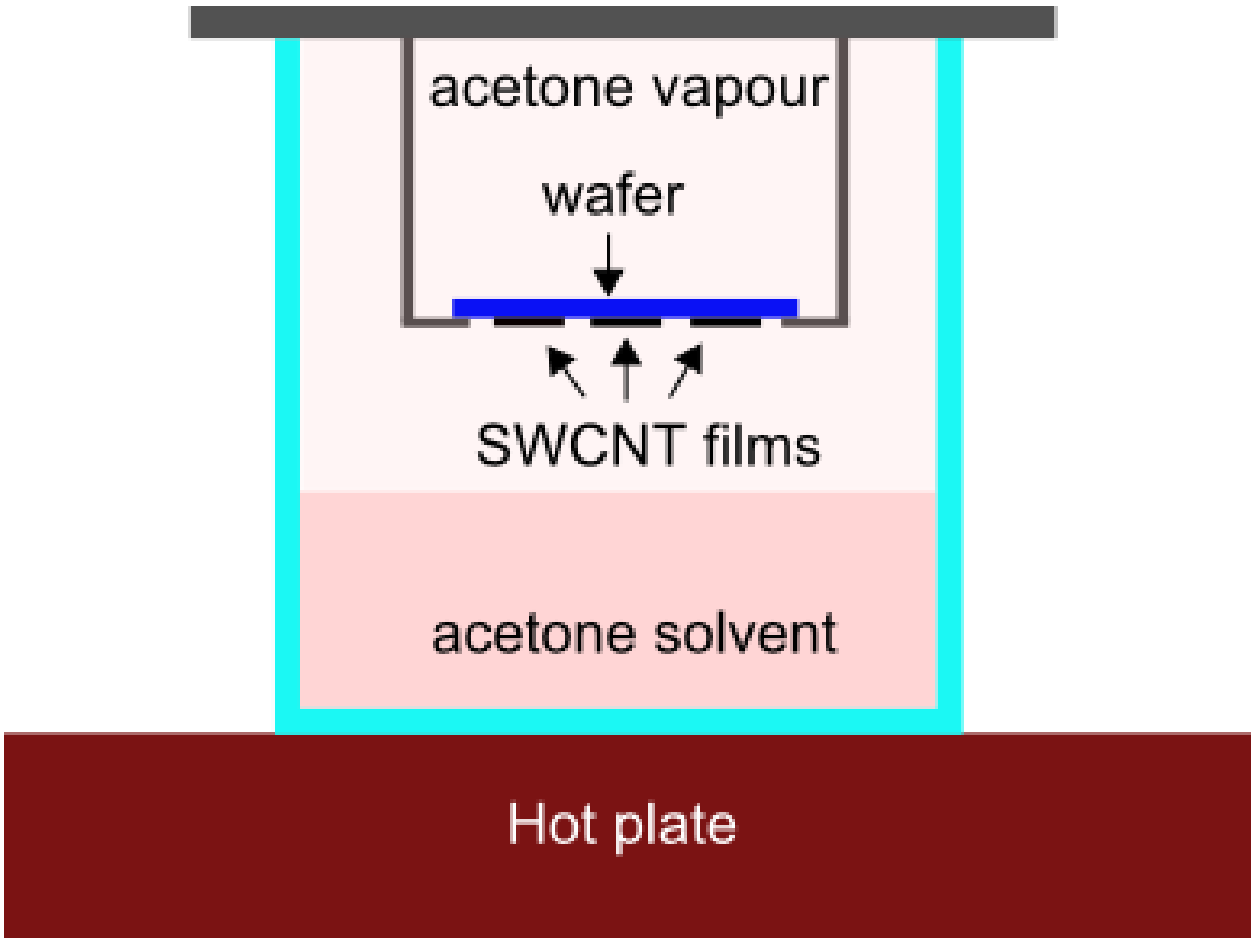

Figure 3.5: The acetone bath setup used to transfer SWNT film on substrate.

The plasma etch recipe used in this work is: 40 sccm O_2, 5 sccm Ar, 20 W, 20 mTorr. As shown in **Figure** 3.6, after the removal of SWNT, the remaining photoresist layer is still thick enough to protect the pattern. A SWNT pattern (see **Figure** 3.7) after O_2 plasma etch matches the design mask.

3.4 Summary

In summary, several methods of processing SWNT have been tested and proven to be successful. Continuous and uniform SWNT film can be made by vacuum filtration, and the thickness of the film can be well controlled by varying solution concentration and volume. A SWNT film transfer process is developed based on acetone vapour bath. O_2 plasma etch is used to pattern SWNT film, while VO_2 stays intact.

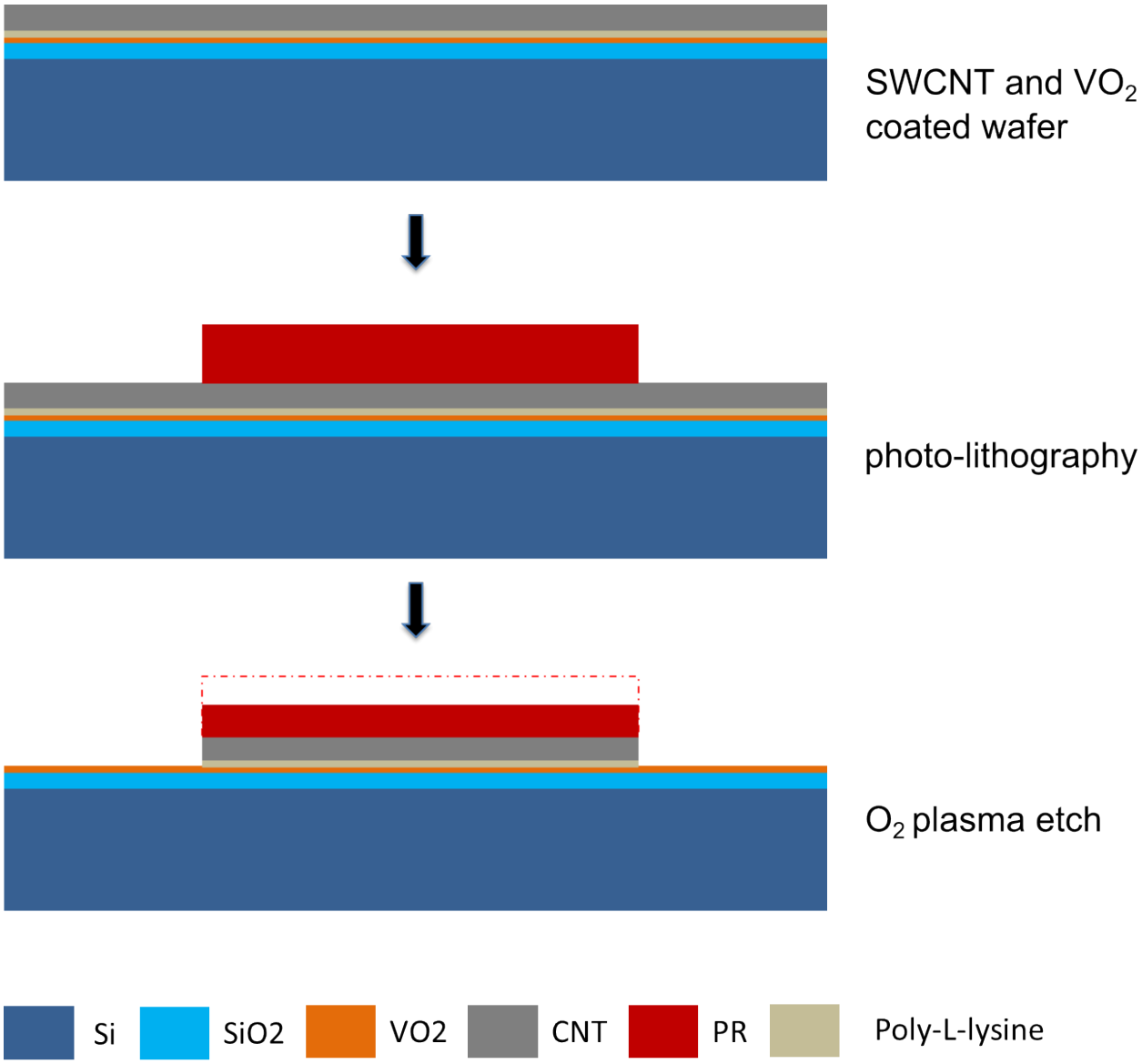

Figure 3.6: The procedure of SWNT patterning.

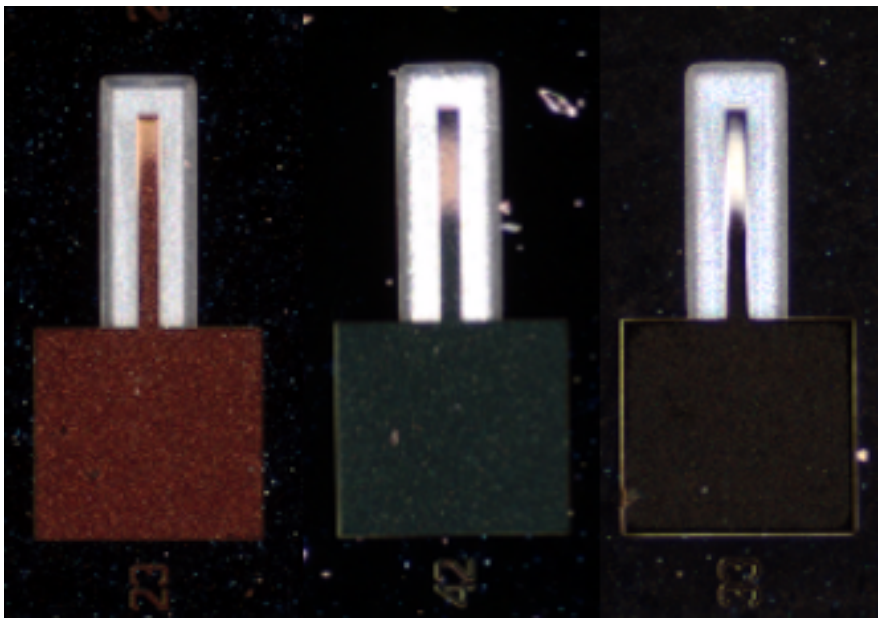

Figure 3.7: SWNT patterns after O_2 plasma etch.

CHAPTER 4

SWNT COATED VO_2 RESISTORS

This chapter reports the first study on the use of single-wall carbon nanotubes (SWNTs) to reduce the amount of photo-thermal energy required to induce the phase transition in vanadium dioxide (VO_2) thin film resistor. A SWNT thin-film prepared using vacuum filtration process was transferred onto a VO_2 thin film (see in **Figure** 4.1). Owing to the superior light-absorption properties of SWNT thin-films, energy from the red light (650 nm) was efficiently harvested and converted to heat, which was then transferred from SWNT to VO_2 to induce the phase transition. We have confirmed that the quality of the VO_2 film was unaltered during the SWNT coating process, nor by the SWNT coating itself. These results show that the integration of SWNT films is an effective way to increase the efficiency of VO_2-based optical sensing devices and could potentially enable triggering of the phase transition in VO_2 films at ambient conditions, which would make low-power VO_2-based non-volatile multifunctional memories a reality. In addition, by using sorted SWNTs with pre-defined chirality, VO_2 sensors with tunable wavelength response could also be readily achieved.

4.1 Fabrication Process

VO_2 thin film was deposited, through pulsed laser deposition (PLD), on the silicon dioxide (SiO_2) substrate to fabricate VO_2 resistors. The substrate was placed into a vacuum chamber with gas pressure of oxygen at 20 mTorr. A metallic vanadium target 2 inches apart from the sample was ablated by forced excimer laser pulses with an intensity of 352 mJ (fluence of 2 J/cm^2) and a frequency of 10 Hz. A ceramic heater used to heat the sample was maintained at 595 °C through 25 minute deposition. Following the deposition, 30 minute annealing process was performed with the same deposition conditions. To determine the quality of the VO_2 film, the resistance of the VO_2 film was measured as a function of temperature which cycled from 30 °C to 100 °C. Two order drop in film resistance was observed, which indicates

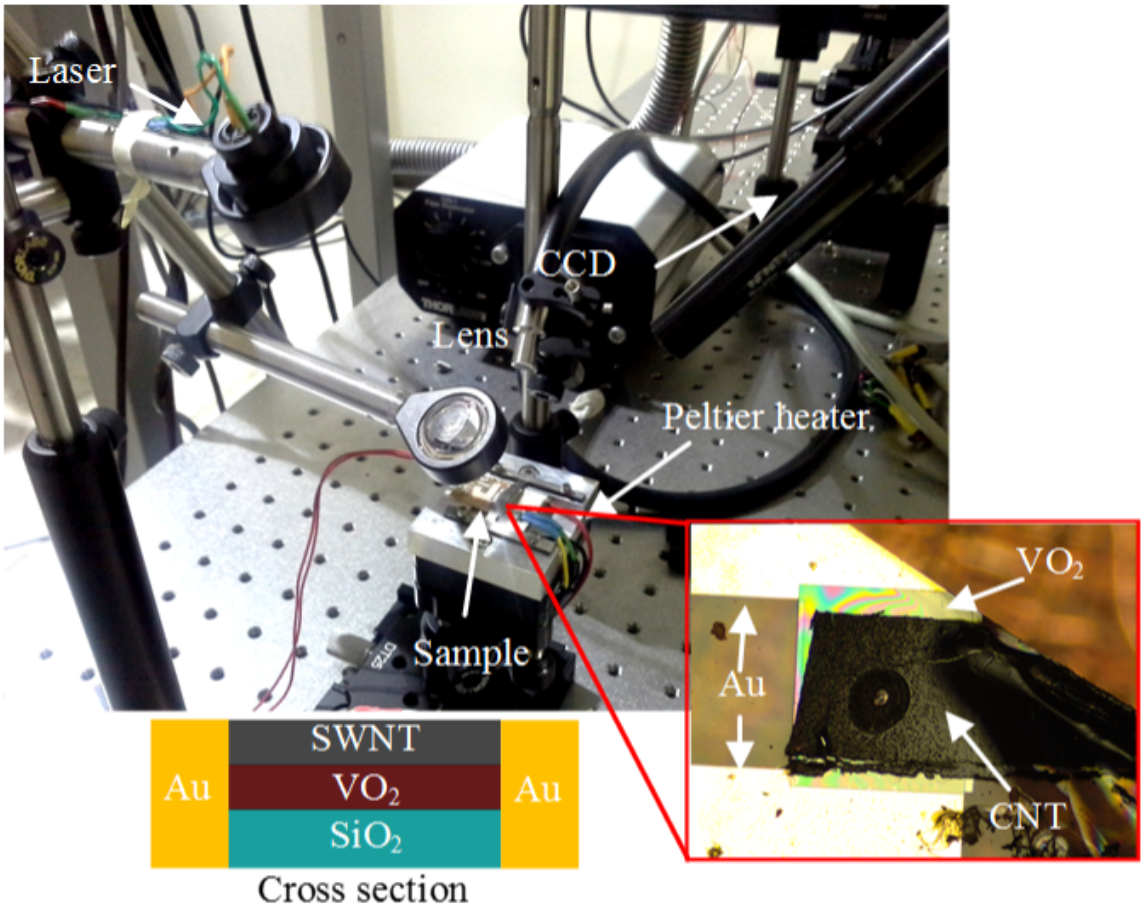

Figure 4.1: Experiment setup used for inducing the phase transition in VO_2 resistor photothermally (using laser) and conductively (using Peltier heater). For scale reference, the VO_2 patch is $550 \times 600\,\mu m^2$.

that the thin film is in fact VO_2.

The SWNT thin-film fabrication follows, in general, the same processes in **Chapter** 3. A 0.1 mg/ml SWNT solution was made of purified SWNT powder purchased from Cheap Tube Inc. (Purity >99wt%, diameter 0.8-1.6 nm, length 3-30 µm), and mixed with 2% sodium deoxycholate as surfactant. 400 minute sonication (Crest Ultrasonic) was performed to completely dissolve the SWNT powder, followed by 10 minute centrifuging with 13,000 rpm rotation speed, which removed large SWNT aggregates and non-SWNT impurities. A standard vacuum filtration setup with 2.5-mm cellulose membrane (pore size 0.45 µm) purchased from Millipore Inc. was used to fabricate the SWNT membrane. The thickness

of SWNT thin film, controlled by the amount of solution used for filtration, was 1 µm as measured using scanning electron microscope (Zeiss EVO LS 25). This thin SWNT film was cut into small pieces being transferred on top of the VO_2 transistor using the same transfer process described in chapter 3.

4.2 Measurement Setup

The measurement setup shown in **Figure** 4.2 was used in all experiments in this paper. The samples were attached to a Peltier heater controlled by a temperature controller (Thorlabs TED 4015), which allowed precise control of temperature. A laser diode (650 nm) was driven by a current source circuit (not shown in **Figure** 4.2) connected to the FPGA controller which was also used to measure the resistance of VO_2/SWNT structures. The FPGA module and temperature controller were completely computer-controlled by using Labview programming. The output power of laser diode was measured as a function of driving current. Through a CCD camera, the laser spot was located to cover the area with SWNT films.

Two types of measurement were applied on different sizes of resistors. The micro scale resistor ($10\times10\,\mu m^2$) was kept at an offset temperature of 55 °C, which is 13 °C lower than the transition temperature, while the laser drove VO_2/SWNT resistors across the IMT transition. The measurement was done on the pristine VO_2 resistor and repeated on the same device after the SWNT film transfer for comparison. This is necessary because the characters of VO_2 film vary slightly from different depositions, which makes the comparison on different samples unreliable even with same size and fabrication conditions. The power consumptions of laser, needed to drive resistor across the transition, were compared, which shows improved power efficiency.

For the large scale resistor ($2.5\times3.5\ mm^2$), the resistance was measured as the temperature was scanned from 30 °C to 100 °C while keeping the laser at a constant power of 70 mW. The hysteretic resistance curve of VO_2/SWNT resistor shifted to lower temperature,

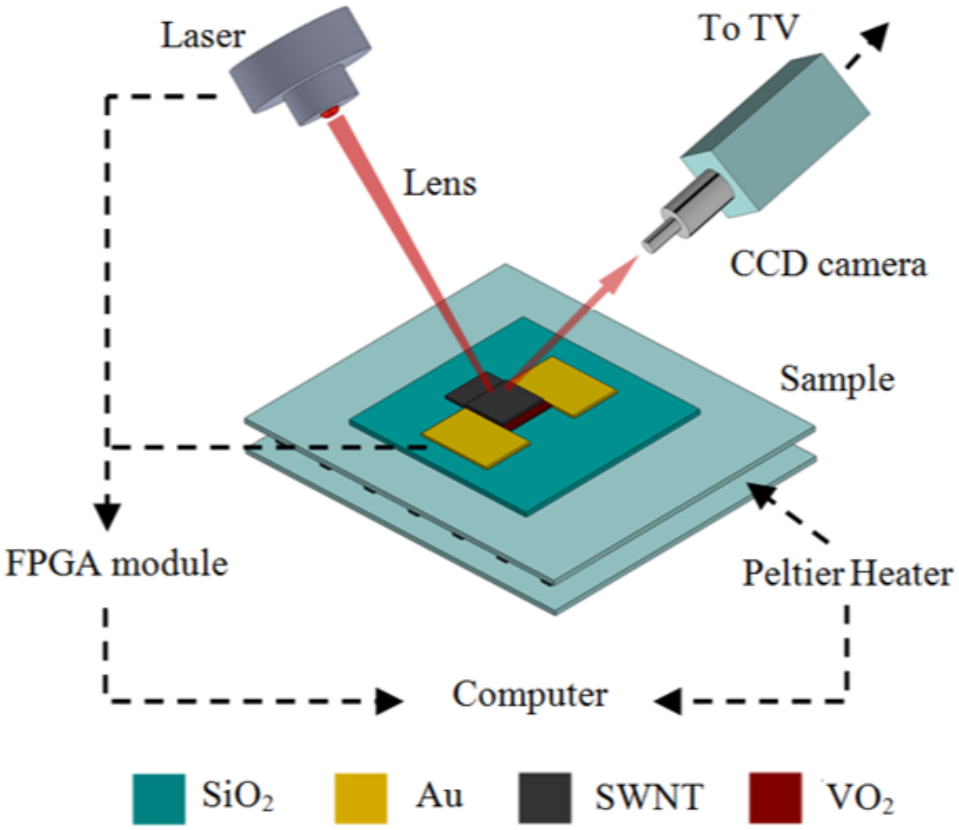

Figure 4.2: Schematic of setup.

compared with the hysteretic resistance curve of pristine VO_2 resistor. Due to the much larger resistor area, this large scale resistor device could not be driven by the laser as it was done for the micro scale device. Driving the transition on the large scale resistor would have required much larger laser power levels, which would most likely damage the device on the hot spots regions of the laser.

4.3 Results

4.3.1 Temperature Response

Figure 4.3 shows the results of measurement on the micro scale device. To determine whether the quality of VO_2 remained the same during the SWNT transfer, heating-cooling cycles of film resistance from the same micro scale device before and after the SWNT film transfer were measured with the laser turned off. As shown in **Figure** 4.3, the shape of the

hysteretic cycle and the transition temperature remain nearly-identical after the SWNT film transfer, which confirms that the SWNT film transfer process is harmless to VO2 film. The difference of the magnitude between lines is due to the parallel resistance of SWNT added to the VO_2 film, which scales down the total resistance, while preserve the hysteretic character of the device.

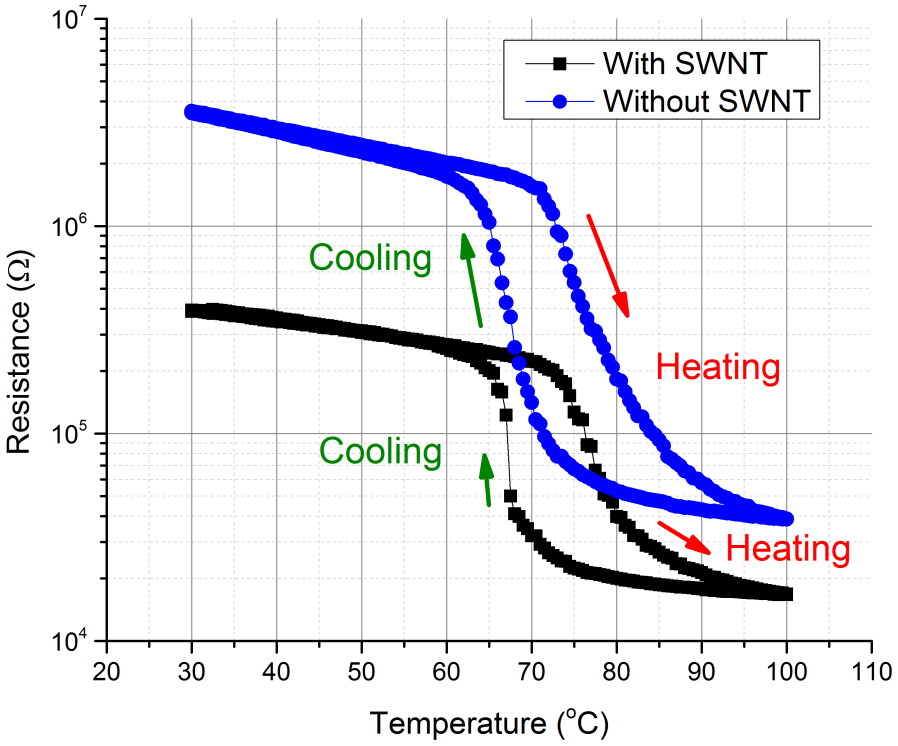

Figure 4.3: Measured resistance of the VO_2 patch (with and without SWNT film coating) as functions of (a) temperature, which is varied using a Peltier heater.

4.3.2 Photo-thermal Response

As mentioned in the previous section, the micro scale resistors were driven through the IMT by laser irradiation at a constant temperature of 55 °C maintained by Peltier heater. The temperature sensor of the heater was placed at the corner of Peltier heater surface to ensure least heating effect from the laser to the sensor. The resistance as a function of laser

intensity is shown in **Figure** 4.4, where it can be seen that after the SWNT film transfer, the resistance response shifts to the left, which means that the laser power required to drive the resistance transition is reduced by the appearance of SWNT film. The laser intensity for triggering the transition in pristine VO_2 resistor is 5.0×10^4 mW/cm2, while a lower intensity of 3.7×10^4 is needed to trigger phase transition in the VO_2/SWNT resistor. This implies about 25% reduction in power consumption.

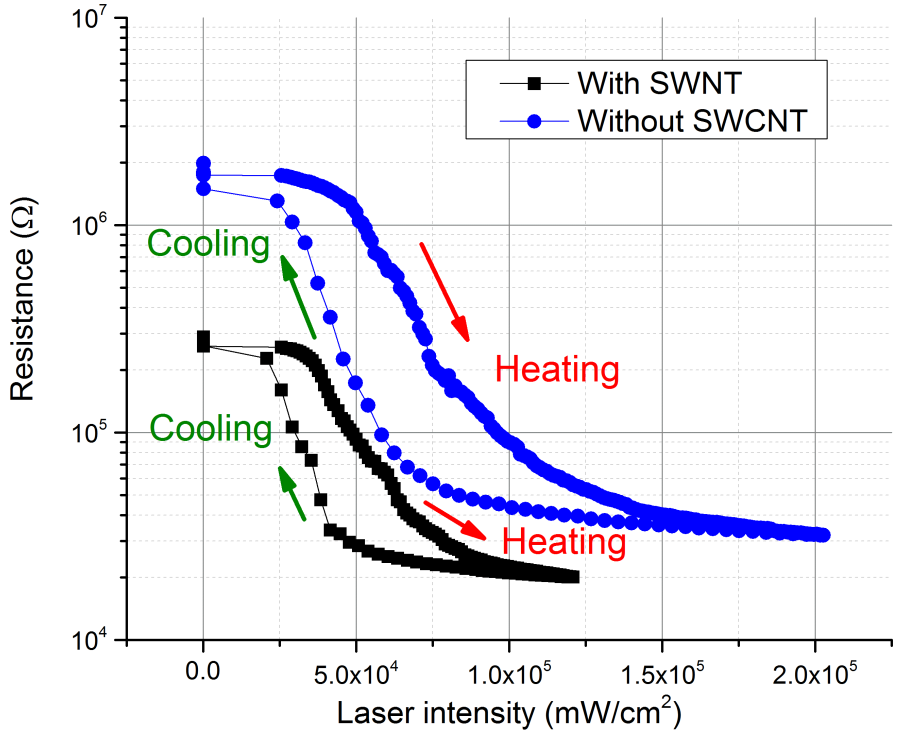

Figure 4.4: Measured resistance of the VO_2 patch (with and without SWNT film coating) as functions of laser intensity.The Peltier heater is used to maintain the substrate at 55 °C, and the laser is used to increase the temperature of the VO_2 resistor.

The resistance of large scale device was measured as a function of temperature, as shown in **Figure** 4.5. The resistance heating-cooling cycles, shown in **Figure** 4.5a, were measured without and with constant laser irradiation of 70 mW before SWNT film transfer, while the same cycles were recorded after the transfer (**Figure** 4.5b). Two insets inside both

figures are from same results only with left-shifted curves that were obtained without laser irradiation. The amount of shift on temperature axis is set to achieve the best overlap with the curves measured with laser irradiation, allowing the quantitative analysis of how much light absorbed by the surfaces and contributing to the transition.

The resistance-temperature curve for the pristine VO_2 device (**Figure** 4.5a) shifts to the left with laser irradiation due to the additional heat contributed by the laser. However, the shift in the curve for VO_2/SWNT device (**Figure** 4.5b) is larger than the one without SWNT film. Minor figures show a 4 °C shift in **Figure** 4.5a and 5 °C in **Figure** 4.5b, indicating a 20% improvement of light absorption. This is consistent with the results from previous measurements of micro scale device.

4.4 Summary

The resistance curve in **Figure** 4.4 for the SWNT-coated VO_2 film is shifted to the left, indicating a lower optical power requirement for reaching the phase transition point. Furthermore, the resistance shift of SWNT-coated VO_2 film in **Figure** 4.5 is also lager than pristine VO_2 resistor. Both results above imply that the SWNT indeed helps improve absorption of optical radiation and reduce the laser power consumption for actuation of VO_2-based devices.

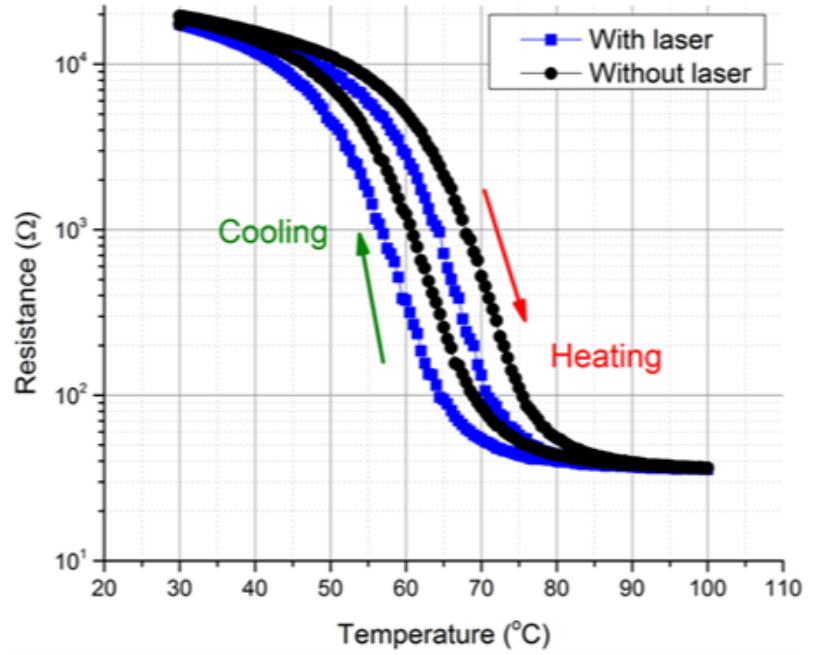

(a)

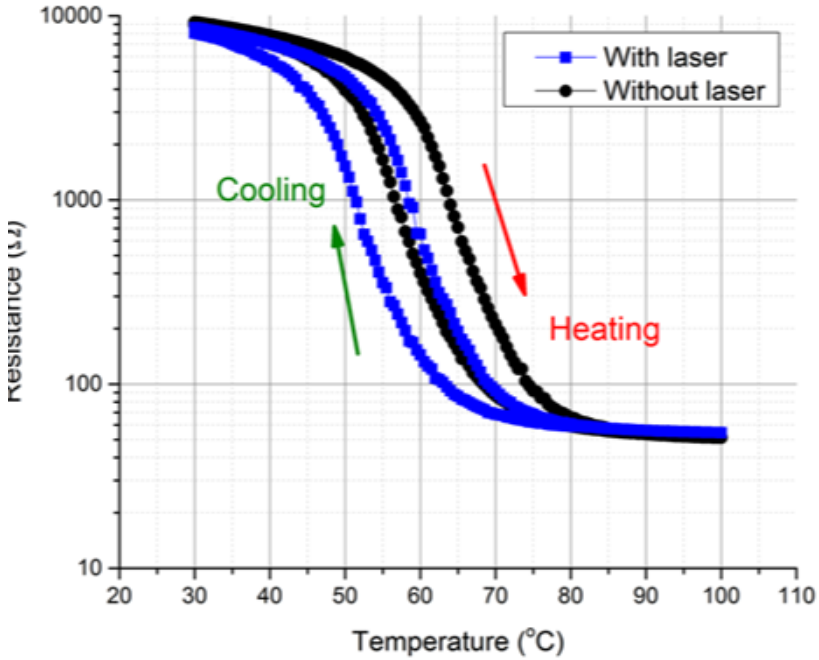

(b)

Figure 4.5: Measured resistance of the VO_2 patch ((a) with and (b) without SWNT film coating) as functions of temperature. In both (a) and (b), the temperature is varied using a Peltier heater, while laser was turned off or set to constant output power (70 mW). The insets in the figures present the same results as that it is belong to except

CHAPTER 5

SWNT COATED VO_2 PHOTO-THERMALLY DRIVEN ACTUATORS

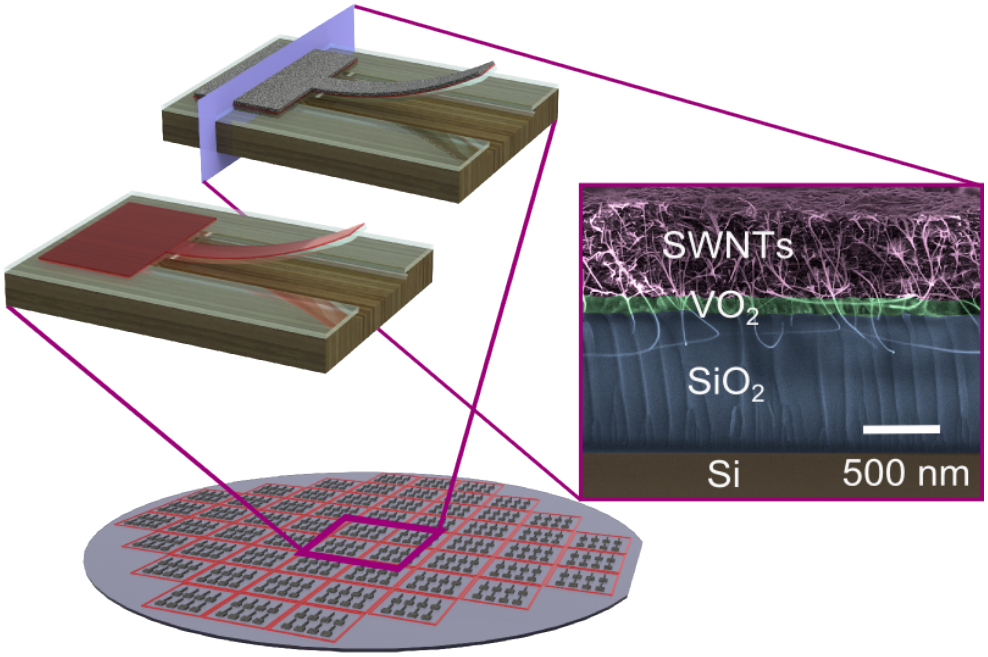

Figure 5.1: Schematic of SWNT coated and VO_2 only actuators with SEM image of cross-section of the device.

In this chapter, a VO_2-based actuator technology that incorporates single-wall carbon nanotubes (SWNTs) as an effective light absorber to reduce the amount of photo-thermal energy required for actuation is presented (see **Figure** 5.1). It is demonstrated that the chemistry involved in the process of integrating the SWNT film with the VO_2-based actuators does not alter the quality of the VO_2 film, and that the addition of such film enhances the actuator performance in terms of speed and responsivity. More importantly, the results show that the combination of VO_2 and SWNT thin films is an effective approach to increase the photo-thermal efficiency of VO_2-based actuators. The integration of SWNT films in VO_2 devices can be easily applied to other VO_2-based photo-transducers as well as to similar

devices based on other phase-change materials. While adding a sufficiently thick layer of some arbitrary material with high absorption for the light used for actuation (λ=650 nm wavelength in this case) could have improved conversion of light to heat in the device, it could also have impeded actuation by increasing its stiffness. It is noted, however, that the low effective Young's modulus of SWNT film coating used in this work does not impair the actuation range.

5.1 Fabrication Process

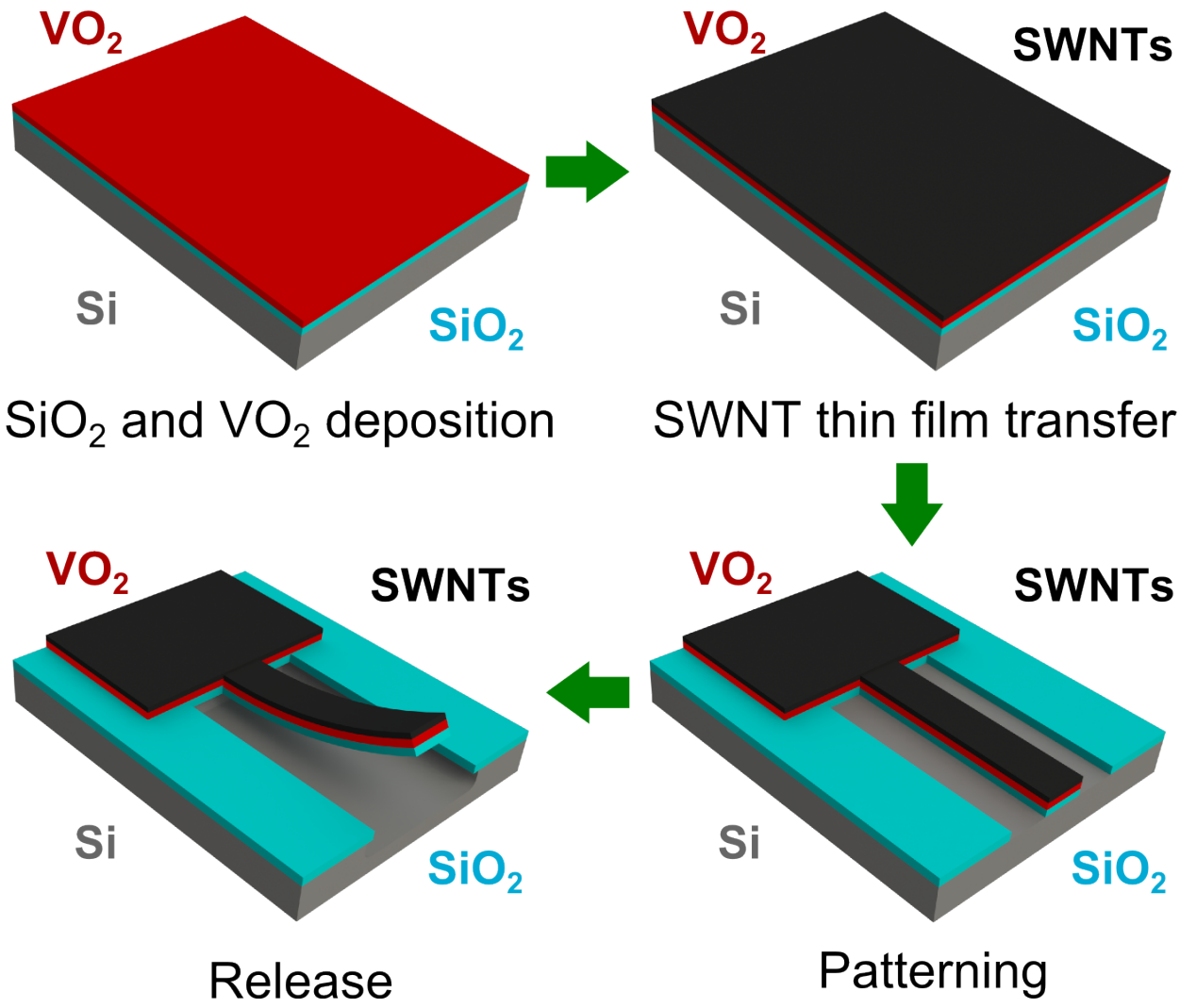

Figure 5.2: Fabrication process of SWNT/VO_2-based cantilever actuator. For clarity, the bare VO_2-based devices are not shown.

Figure 5.2 schematically illustrates the fabrication process of the SWNT/VO_2-based cantilever actuator used in this work. The initial substrate was a 2-inch silicon wafer. A silicon dioxide (SiO_2) layer (1 μm thick) was first deposited by plasma-enhanced chemical vapor deposition (PECVD), followed by the deposition of a 120 nm thick VO_2 layer by the method of pulsed laser deposition (details can be found in previous chapter). The high quality of the VO_2 film is demonstrated by the more than 2 order drop in resistance observed when the temperature was increased from 30 to 100 °C (see **Figure** 5.3. After VO_2 deposition, a

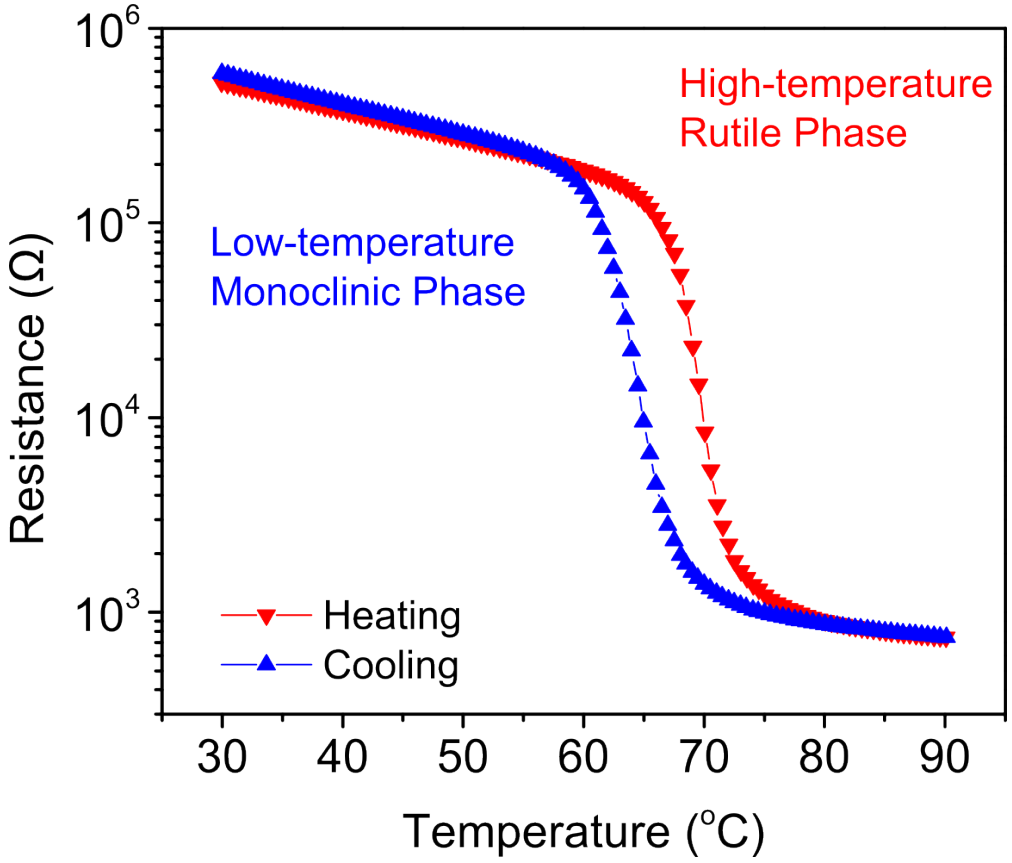

Figure 5.3: (Resistance of VO_2 as a function of temperature.

SWNT thin film ($\sim$ 500 nm thick) made by vacuum filtration (details in the chapter 3) was transferred on top of certain regions of the wafer. At this point, the substrate contains regions of $VO_2/SiO_2/Si$ and others of SWNT/$VO_2/SiO_2/Si$. This fabrication process guaranteed that the same VO_2 film was present in the final VO_2-based actuator devices (with and without a SWNT film coating), thus allowing for a fair device performance comparison.

The SWNT film was patterned first using oxygen plasma, while the regions in the wafer where the VO_2 film was exposed were protected by photoresist. After patterning of the SWNT, the photoresist protecting the VO_2 layer was removed, and the same mask used for the SWNT was used to pattern the VO_2 layer using reactive ion etching CF_4-based recipe. A photoresist layer was also used to pattern the VO_2 film, and to protect it during the dicing of the wafer and the structure release using isotropic etching of silicon in XeF_2 gas. The photoresist was removed after release. The suspended structures showed initial bending at room temperature. This is due to the intrinsic thermal stress induced during the deposition of VO_2 at 595 °C and subsequent cooling to room temperature. **Figure** 5.4 shows

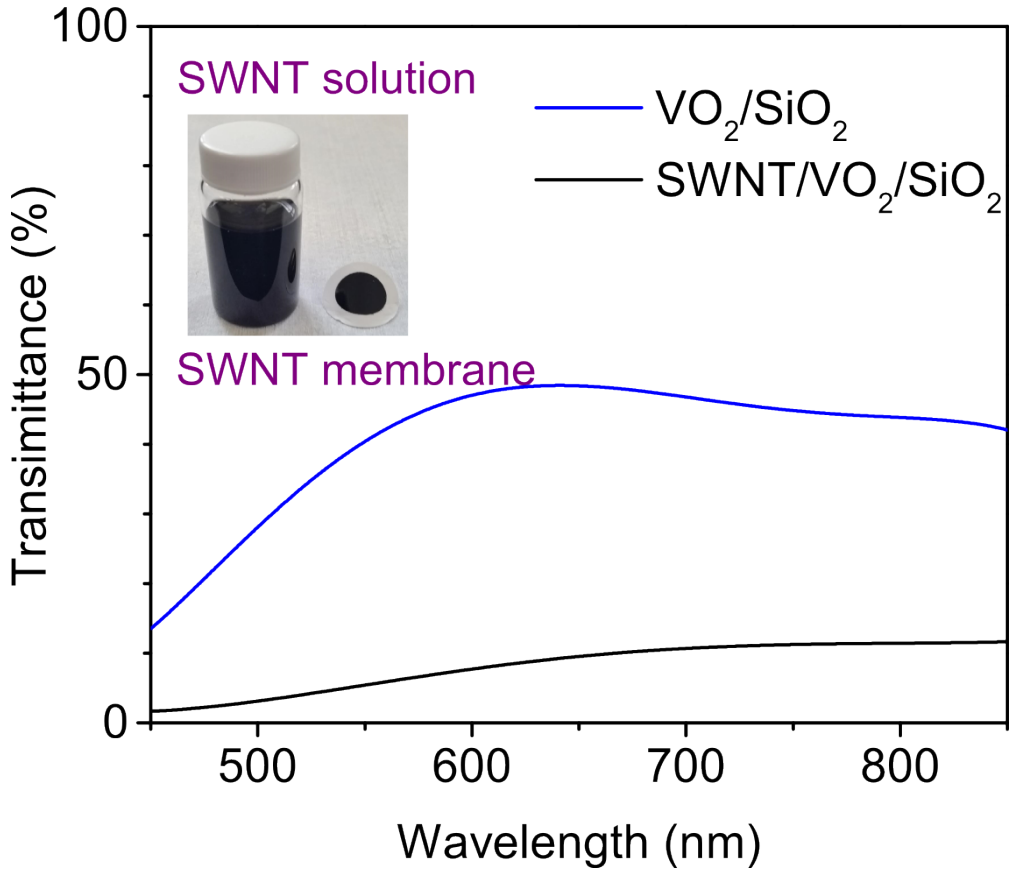

Figure 5.4: (Measured optical transmittance spectra of VO_2 film (120 nm thick) over SiO_2 substrate before (blue curve) and after (black curve) being coated with SWNT film (800 nm thick).

the optical transmittance spectra of VO_2 thin film (120 nm thick) on SiO_2 substrate, and the transmittance of the same sample, now coated with a SWNT film (800 nm thick). Top

view microscope images of SWNT/VO_2- and VO_2-based cantilevers are shown in **Figure** 5.5 with a zoomed scanning electron microscope (SEM) image showing the cross section of SWNT/VO_2-based cantilever, in which display colors have been artificially modified for clarity.

5.2 Measurement Setup

The measurement setup used in this project is shown in **Figure** 5.6. The tested samples were installed on top of a Peltier heater attached on a micrometer translation stage. Above the sample, a red laser (650 nm) focused by a lens was used to illuminate photoactuators. A camera placed at one side is responsible for imaging and recording the cantilever during actuation. Software Tracker tracked the tip movement of cantilever in the video, and the length of the cantilever (400 μm) was used to calibrate the deflection.

Two main types of actuation experiments were performed: 1) conductive and, 2) photo-thermal heating actuation. The conductive heating experiments were performed mainly to verify that the phase change characteristics of VO_2 film remain unchanged after the transfer of the SWNT film. The photo-thermal experiments demonstrated the larger efficiency, speed, and responsivity of SWNT/VO_2-based actuators. In the conductive heating experiments, only a Peltier heater was used, whereas in the photo-thermal experiments, the same Peltier heater was used only to provide a constant temperature offset while laser pulses were applied.

5.3 Results

5.3.1 Temperature Response

The actuator deflection is defined in this work as the displacement of cantilever's tip along the direction normal to initial bending. The deflection of SWNT/VO_2 and bare VO_2 cantilever actuators was studied as their temperature varied by using conductive heating through a Peltier heater under the chips (**Figure** 5.7). This conductive heating produced a change in temperature that was nearly uniform in the entire chip substrate. The typical hysteretic

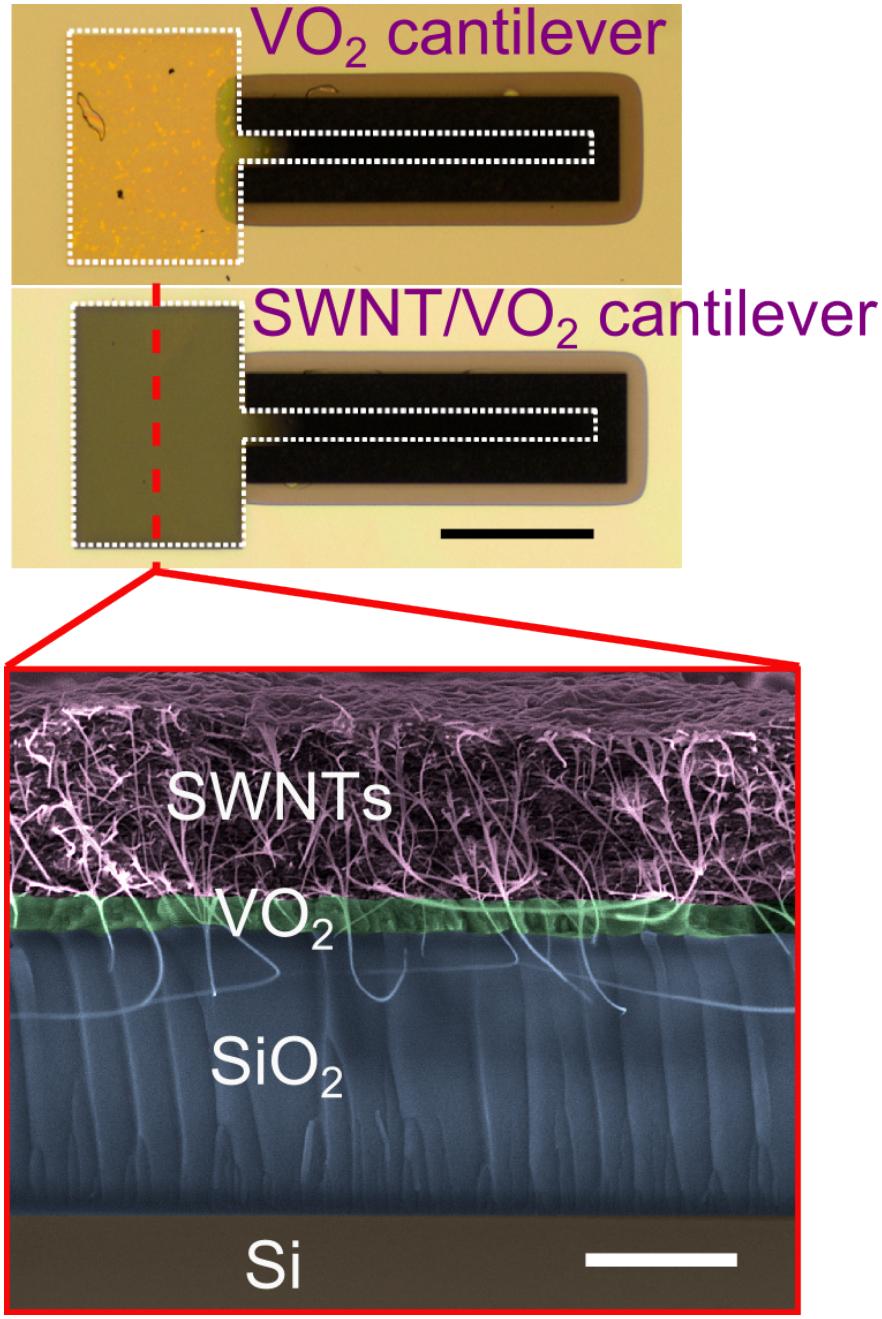

Figure 5.5: Top view microscope images of SWNT/VO_2- and bare VO_2-based cantilevers with same length of 400 μm and width of 40 μm. The zoomed image is a SEM image of cross-section of the SWNT/VO_2-based cantilever, in which colors have been artificially modified for clarity. The scale bars in the optical and SEM images are 200 μm and 500 nm, respectively.

shape of deflection curve of one heating and cooling cycle was obtained for both cantilever structures, which implies that the phase transition of VO_2 is the dominant mechanism that

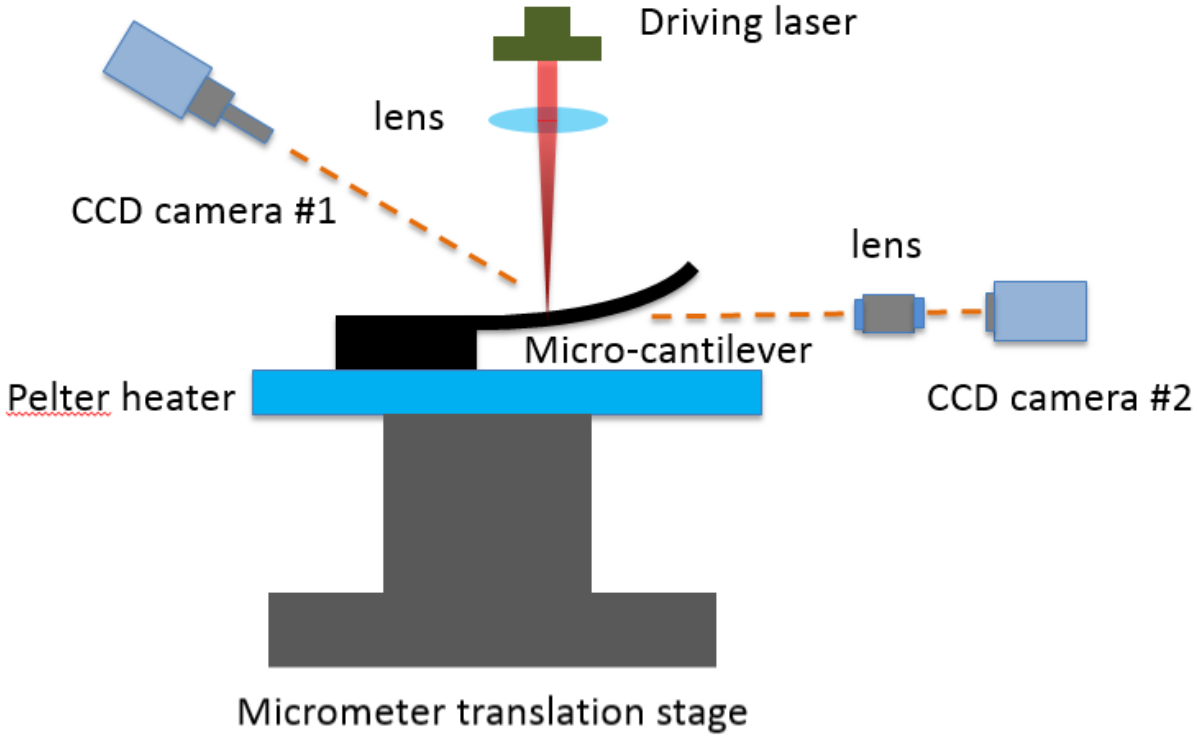

Figure 5.6: Measurement setup for performing characterization experiment on the actuators.

produces actuation for both devices. The effects of the mismatch between the thermal expansion coefficients of the SWNT and VO_2 layers is small during the phase transition, and the low Young's modulus of the SWNT film allows for minimal deflection differences between both devices. For regions outside the phase transition (temperatures below 65 °C and above 80 °C) the observed bending in the opposite direction to the one during the phase transition is produced by the larger thermal expansion coefficients of SWNT and VO_2 films when compared to SiO_2 (see Table 5.1).

It can be noticed in **Figure** 5.7 that the maximum deflection for the SWNT/VO_2-based actuator is $\sim$ 10 μm smaller than that of the bare VO_2-based one. This is probably due mainly to the larger thickness of the SWNT/VO_2 device, which increases the overall structure spring constant and bending resistance. However, the transition temperatures of both cantilevers are practically identical, which indicates that the quality of VO_2 remains unaltered after the SWNT thin film transfer.

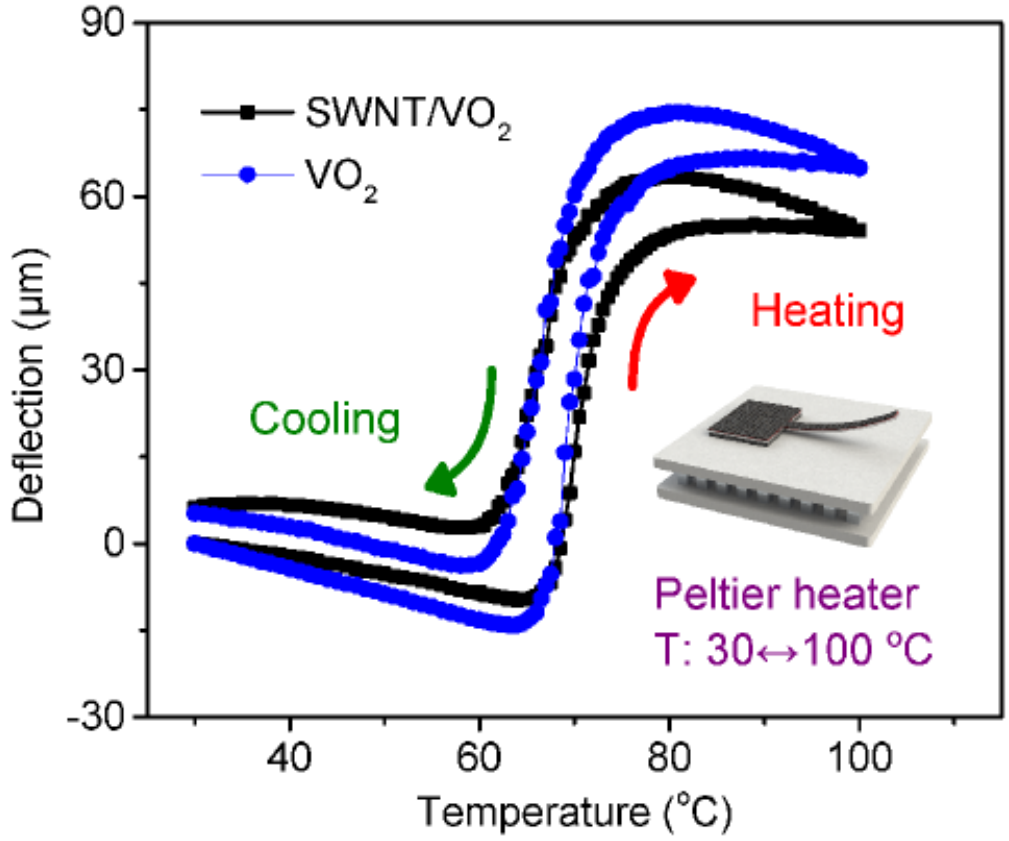

Figure 5.7: Measured displacement of the VO_2 cantilevers and SWNT/VO_2-based cantilevers as functions of temperature. The temperature is varied using a Peltier heater, while laser was turned off.

5.3.2 Photo-thermal Response

The temperature of the substrate was maintained at 30 °C by the same Peltier heater used for the conductive heating experiments. Red laser pulses (λ=650 nm), normal to the testing chip, with duration of 0.5 s were used for photothermal actuation. The red laser beam was focused to $\sim$ 600 μm in diameter in order to illuminate the entire cantilever during each pulse. **Figure** 5.8 shows the deflection measured as a function of laser pulse intensity. As shown in **Figure** 5.9, all cantilevers have initial bending at 30 °C due to residual stress during fabrication. The actual intensity on the cantilever depends on the device bending angle, which means that it varies along its length. Furthermore, the bending angle changes during photo-thermal actuation, which makes the actual irradiance also a function of time

through the actuation cycle. Thus, the laser intensities given were estimated by using the laser power and approximating the laser spot as a circle with a 600 μm in diameter.

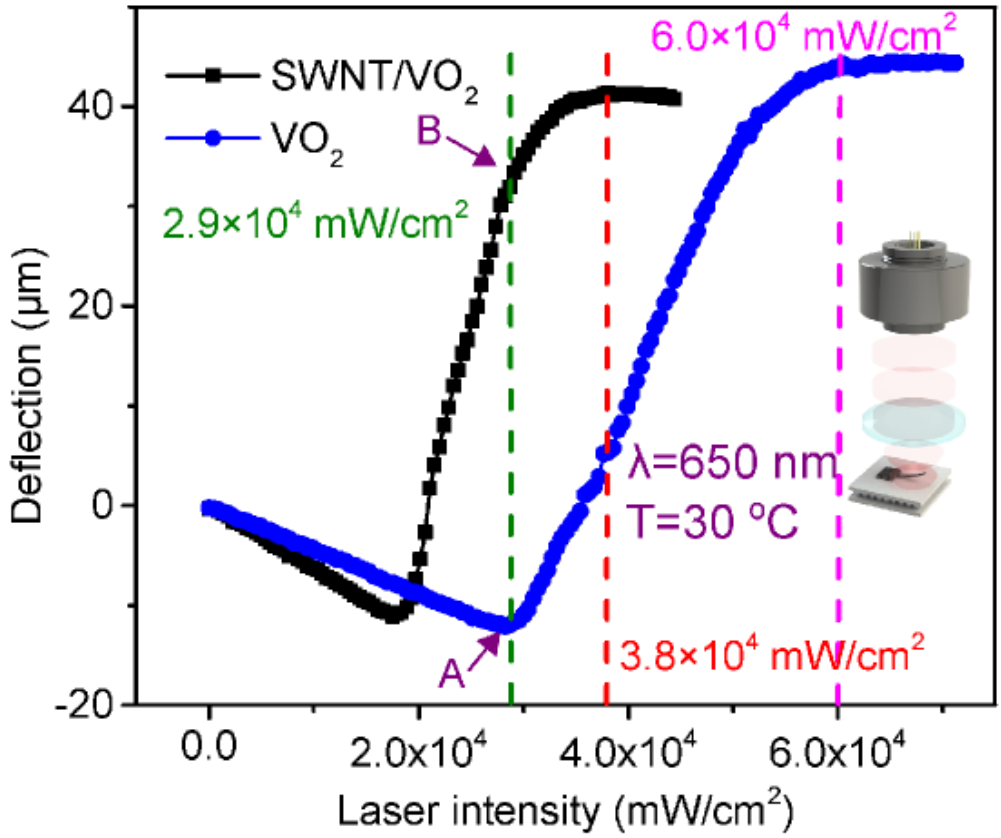

Figure 5.8: (a) Measured displacement of the VO_2 cantilevers and SWNT/VO_2-based cantilevers as functions of intensity of laser pulses. The temperature was set to 30 °C, while laser pulses were applied by controlling the current of a laser diode. The intensities marked with the green and red dashed lines are the ones used in the time-response experiments.

It is noticed that, as shown in **Figure** 5.8a, the light intensity required to achieve the transition for each cantilever is different —the SWNT/VO_2-based actuator curve is shifted to the left. Only 1.8×10^4 mW/cm^2 is needed to initiate the phase transition in the SWNT/VO_2-based actuator, while about 2.9×10^4 mW/cm^2 is needed for the bare VO_2-based actuator. This represents 38% improvement of optical energy consumption. Similarly, the light intensity for full actuation of the SWNT/VO_2- and VO_2-based actuators are $\sim 3.8\times10^4$ and $\sim 6.0\times10^4$ mW/cm^2, respectively. It should also be mentioned that the intensity on the bare VO_2 device is actually larger than that on the SWNT/VO_2-based during the entire actuation

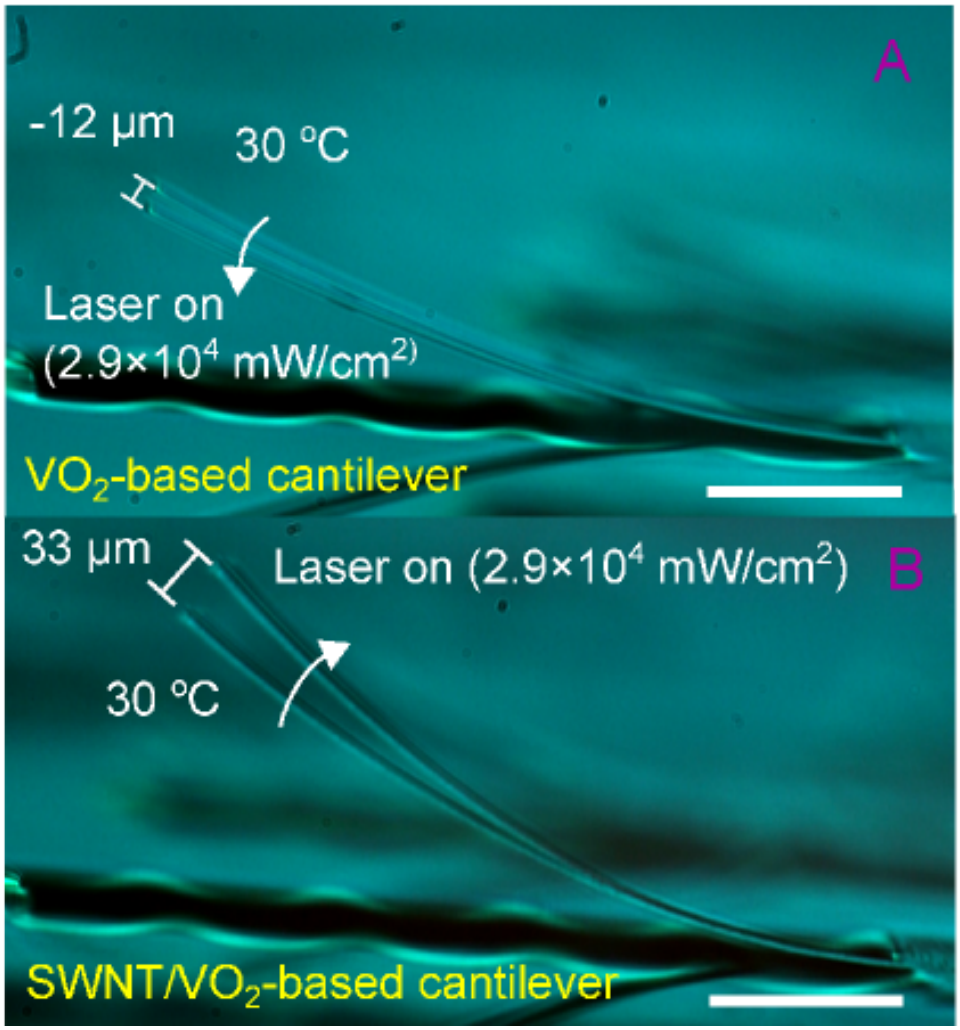

Figure 5.9: (b) Images of cantilevers correspond to the laser intensities A and B labeled in **Figure** 5.8. The scale bar is 100 μm.

range, since the initial curvature at room temperature for the former is smaller. Yet, the bare VO_2-based cantilever still requires larger laser intensity for reaching the phase transition. This supports the obervation of a lower intensity requirement for the SWNT/VO_2-based actuators. This improvement in energy consumption for the SWNT/VO_2-based device is attributed to a combination of the larger thickness and higher absorption of SWNT films (when compared to VO_2). However, although a larger thickness will improve absorption (at least up to a couple of SWNT skin depths), adding thickness to the actuator will increase its rigidity, and therefore could deteriorate the device performance.

The difference of the maximum deflections from uniform conductive heating and photothermal heating is due to the fact that in the photothermally actuated device part of the heat converted from light is dissipated through the cantilever's anchor, where the temperature is maintained at 30 °C; while in conductive heating there is very little difference in temperature between the cantilever, its anchor, and the substrate. Also, the uniform heating of the cantilever when using conductive heating results in a uniform bending along its length, and thus a larger total deflection than when localized optical radiation is used for actuation. Thus, it should be clarified that a direct correlation between laser intensity and temperature using **Figure** 5.7 and **Figure** 5.8 cannot be made, since the temperature boundary conditions for the lumped models of both mechanisms are not the same.

Another difference between two curves in **Figure** 5.8 is the slope during the transition, which represents the responsivity of the device. The results indicate that given the same change in laser intensity, the SWNT/VO_2-based actuator will produce a larger deflection ($\sim$ 3.84 μm/mW-cm^{-2} for the SWNT/VO_2-based and $\sim$ 2.83 μm/mW-cm^{-2} for the bare VO_2-based). This is likely to be due to the combination of two mechanisms: the larger absorption of the SWNT film and the low thermal conductivity of SWNT films. This larger responsivity could also be beneficial if the presented devices were going to be used as light sensors.

5.3.3 Time Response

The optical actuation experiments demonstrated that the SWNT thin film significantly improved the efficiency and responsivity of the VO_2-based photo-actuators. However, the effect of the SWNT layer on the dynamic performance of the VO_2-based photo-actuators in terms of bandwidth was still unclear. Therefore, measurements of time response for the SWNT/VO_2- and bare VO_2-based actuators were performed by using a high speed camera (Nikon One J1 with 1200 frames per second). The results are shown in **Figure** 5.10. The laser pulse duration for both plots (**Figure** 5.10a-b) are 20 ms, but light intensities are different (labeled in

Figure 5.10b as the green and red dashed lines). The light intensity used for **Figure** 5.10a is large enough to enter the phase transition for both devices. It can be seen how the displacement in both devices gradually decreases initially (outside the phase transition region) and then suddenly increases (as soon as the transition is reached), following the same behavior observed in **Figure** 5.10b. The faster response of the SWNT/VO_2-based actuator can be clearly noticed. The time constants for the SWNT/VO_2- and bare VO_2-based actuators were defined as the time from the start of the laser pulse to the steady state deflection value of the actuator. These time constants were measured during heating (see **Figure** 5.10a), which was slower than the cooling process for both devices, and their estimated values were 3.3 ms and 8.3 ms, respectively.

If a slightly lower laser intensity is used (green dashed line in **Figure** 5.10b), the actuation of the SWNT/VO_2-based actuator still crosses most of the phase transition (see **Figure** 5.10b), but the VO_2-only device does not even reach the beginning of the phase transition, thereby exhibiting only downward displacement (**Figure** 5.10b).

5.3.4 Light Absorption Efficiency Calculation

In order to help analyze the obtained results and quantify the increase in light absorption efficiency, a numerical simulation using finite element method (FEM) implemented with COMSOL software was conducted. The results are summarized in **Figure** 5.11. The study in COMSOL used a steady-state heat transfer and solid mechanics modules with the three-dimensional geometry of the cantilever presented in this work. The heat converted from the laser was simulated by an inflow heat flux boundary condition on the top cantilever surface with controlled intensity. The effects of heat transfer through the surrounding air (convection losses) were also included in the simulations. Thermal radiation losses were neglected. Commonly accepted values were used for SiO_2 thermal properties, and the properties for VO_2, and SWNTs used in the simulation were taken from the literature [1, 2, 3, 4, 5], and are summarized in Table 5.1. The thermal expansion coefficient of VO_2 was assumed as

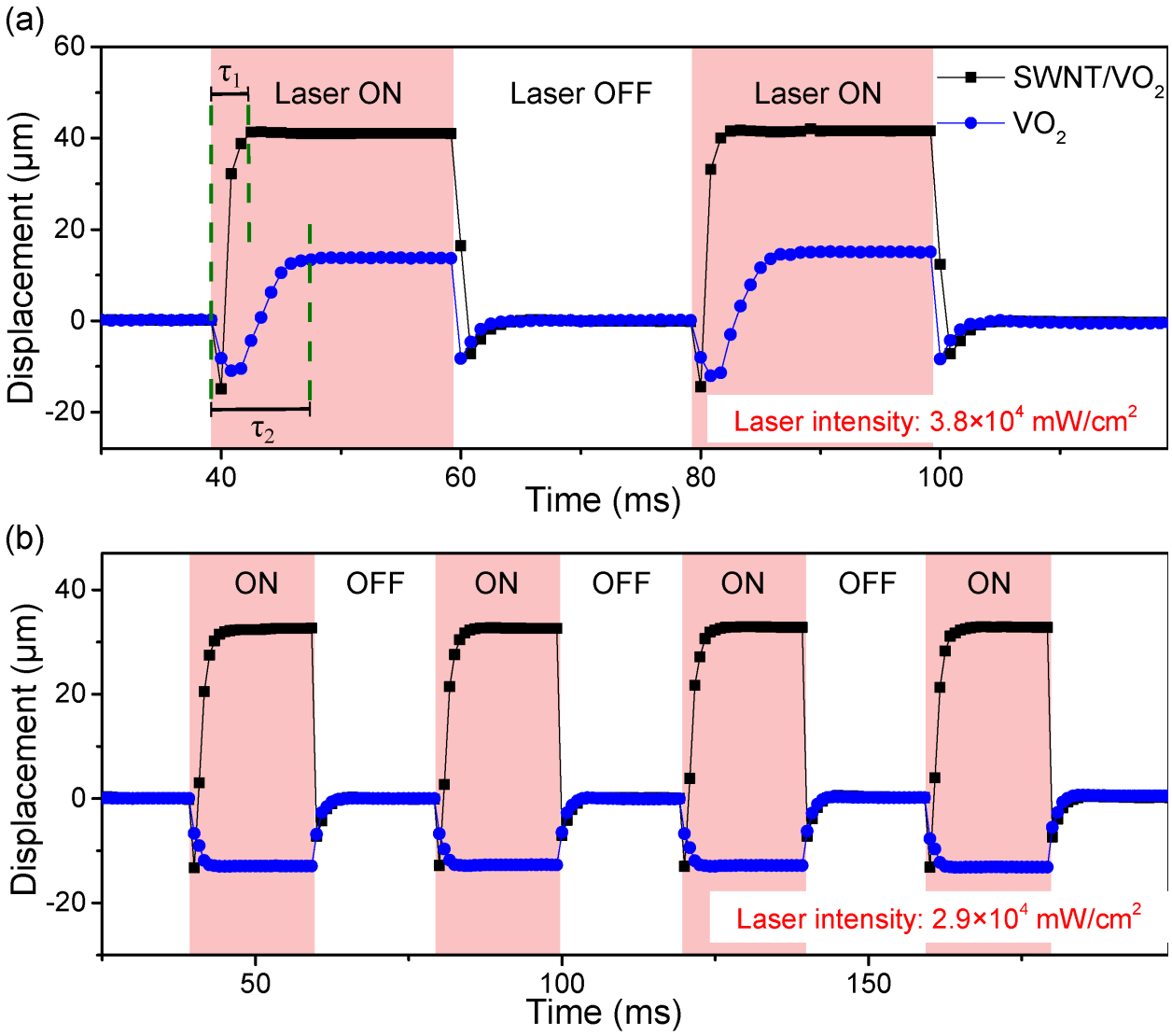

Figure 5.10: Measured time response of the VO_2 cantilevers and SWNT/VO_2-based cantilevers with driven laser intensity of (a) 3.8×10^4 mW/cm^2 and (b) 2.9×10^4 mW/cm^2. The duration of tested laser pulses is 20 ms.

a function of temperature to simulate the phase transition of VO_2 (as it was done in Cabrera et.al [1]). The values for α(T) in Table 5.1 were in the range of 2.3 - 5 $\times10^{-6}$ /K.

Due to the heat sink function of the anchor, and convection cooling of the air, the temperature distribution along the device is not uniform when uniform heat influx is applied. The temperature distribution along the SWNT/VO_2-based cantilever is shown in **Figure** 5.11a with a heat flux of 6.7×10^3 mW/cm^2. From the simulations, the necessary intensity of heat flux to reach maximum deflection was estimated to be 6.7 $\times10^3$ mW/cm^2 for the

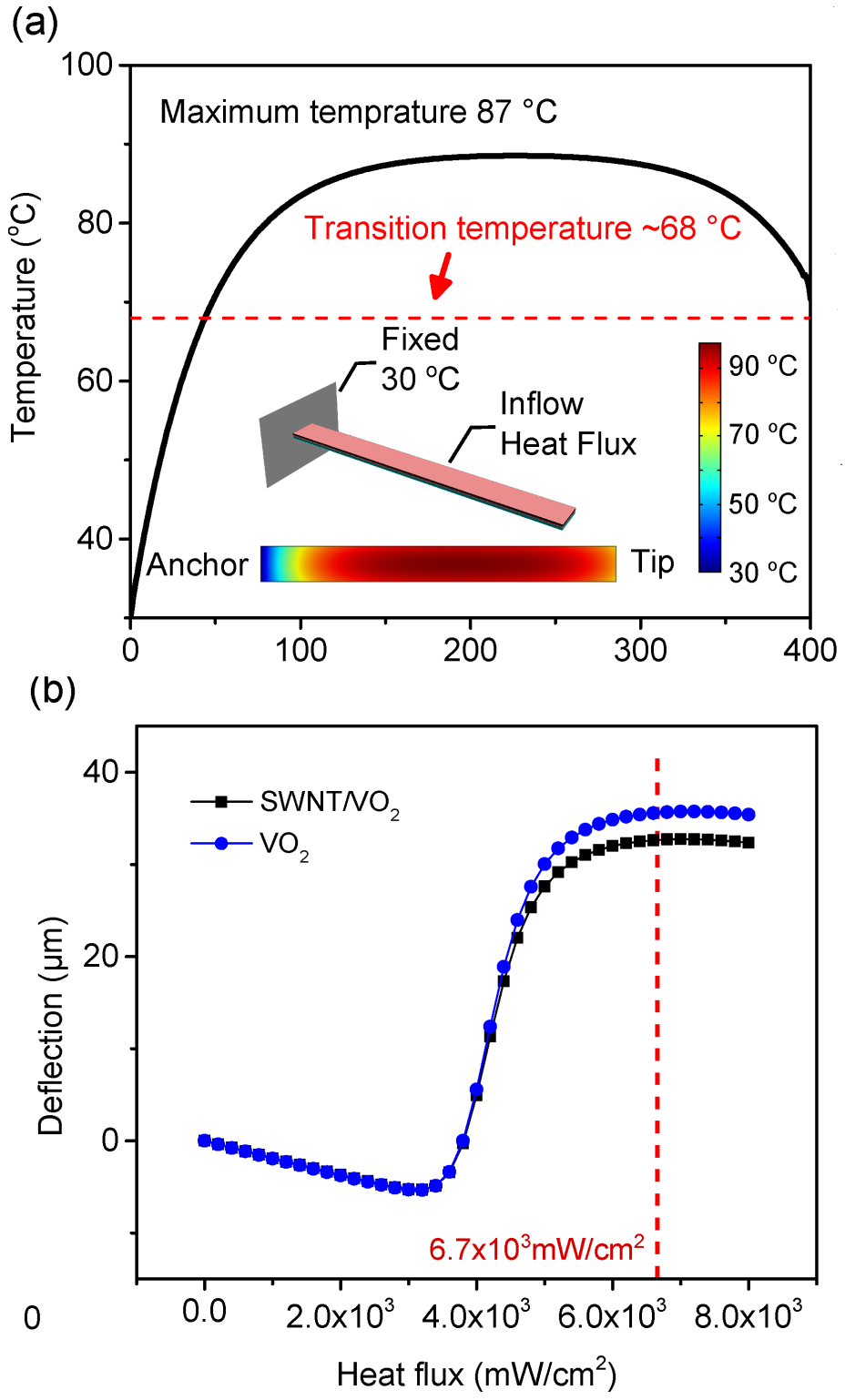

Figure 5.11: (a) Calculated temperature distribution along the SWNT/VO_2-based cantilever with heat flux intensity of 6.7 $\times 10^3$ mW/cm^2. The red dash line represents the transition temperature. (b) Calculated deflection of cantilevers as a function of heat flux.

Table 5.1: Materials properties used in the finite element simulations and for discussions of results [1, 2, 3, 4, 5].

Materials	SiO_2	VO_2	SWNT film
density (kg m^{-3})	2200	4670	1500
Thermal conductivity (W m^{-1} K^{-1})	1.4	5	0.07
Heat capacity at constant pressure (J kg^{-1} K^{-1})	730	700	550
Young's modulus (GPa)	70	140	1.5
Thermal expansion coefficient (10^{-6} /K)	0.5	α(T)	3

SWNT/VO_2- and bare VO_2-based actuators (see **Figure** 5.11b). Using the estimated laser intensities for full actuation for both devices mentioned earlier (and shown in **Figure** 5.11b) and the simulation, the transfer efficiencies from optical energy to heat can be calculated to be 17.6% and 11.7% for the SWNT/VO_2- and bare VO_2-based devices, respectively.

5.4 Summary

In summary, a new and simple approach to increase the efficiency, responsivity, and speed of VO_2-based photo-thermally driven actuators is presented, which utilizes the excellent light-absorbing properties of a SWNT film prepared using a simple vacuum filtration process. Table 5.2 summarizes the comparison between the two presented devices. The improvements are mainly attributed to the better optical absorption, larger thickness, and lower thermal conductivity of SWNT films, when compared to VO_2 films. The transferring of the SWNT did not alter the VO_2 film quality, which represents an opportunity to further expand the integration of SWNTs and VO_2 films to a plurality of device designs and applications. Moving forward, the SWNT/VO_2 photoactuators can be optimized in terms of SWNT and VO_2 thickness. Moreover, by using purified SWNTs with different chirality distribution and thereby different absorption spectra, programmable wavelength-selective photoactuator can be obtained.

Table 5.2: Performance comparison between both presented devices

Performance	VO_2-based	SWNT/VO_2-based
Laser intensity for full actuation (mW/cm^2)	$\sim 6.0 \times 10^4$	$\sim 3.8 \times 10^4$
Absorption efficiency (%)	11.7	17.6
Responsivity (μm/mW-cm^{-2})	2.83	3.84
Time constant (ms)	8.3	3.3

CHAPTER 6

WAVELENGTH SELECTIVE PHOTOTHERMAL ACTUATORS

The search for higher performance of photothermal micro-actuators has typically involved unavoidable trade-offs that hinder the demonstration of ubiquitous devices with high energy density, speed, flexibility, efficiency, sensitivity, and multifunctionality. Improving some of these parameters often implies deterioration of others. In this chapter, we present a device that has been strategically designed to show high performance in every metric and respond to optical radiation of selected wavelength bands. The device combines the large energy densities and sensitivity of vanadium dioxide-based actuators with the wavelength-selective absorption properties of single-wall carbon nanotube films of different chirality distributions. Devices coated with metallic SWNT were found to be 1.57 times more responsive to red light than to near-infrared, while semiconducting SWNT coatings resulted in 1.42 times higher responsivities to near-infrared than to red light. The added functionality establishes a link between optical and mechanical domains of high-performance photoactuators, and enables the future development of mechanical logic gates and electronic devices that are triggered by optical radiation from different frequency bands.

6.1 Fabrication Process

Figure 6.1 schematically illustrates the fabrication process of VO_2/SWNT actuators. The process starts with a 2 inch silicon wafer coated with 1 m thick silicon dioxide (SiO_2) layer deposited by plasma-enhanced chemical vapour deposition (PECVD) at 300 °C. A thin layer of VO_2 (50 nm thick) was then deposited on SiO_2 layer by pulsed laser deposition (PLD). The quality of the VO_2 thin film was characterized by measuring its resistance as function of temperature, which shows a nearly three-order of magnitude resistance drop, as temperature changes from 30 to 100 °C (see **Figure** 6.2), indicating good quality VO_2. The SWNT thin films tested in this project were made by vacuum filtration technique using

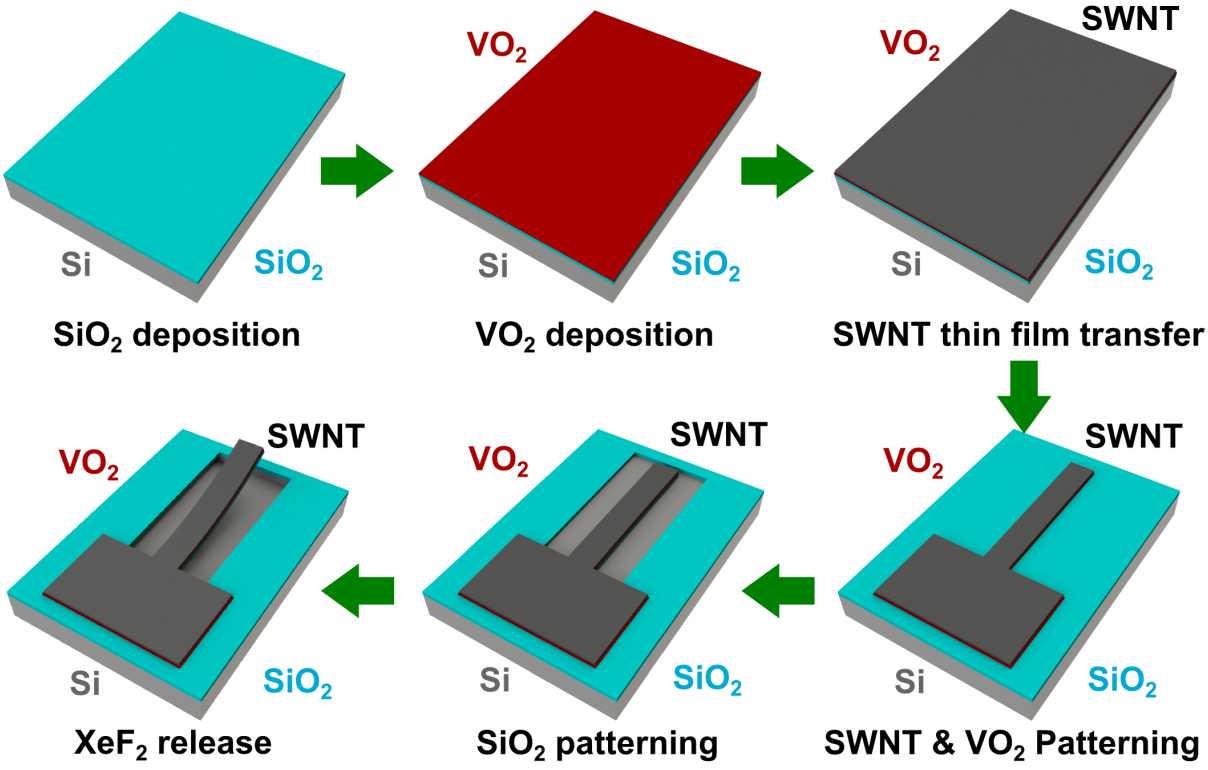

Figure 6.1: Fabrication process of VO_2/SWNT actuators

three different types of SWNT solutions shown in **Figure** 6.3. Unsorted SWNT (uSWNT), metallic SWNT (mSWNT), and semiconducting SWNT (sSWNT) are solutions containing a mixture of chiralities [159, 160, 161]. These SWNT films were transferred on top of the VO_2/SiO_2-coated silicon wafers following a surface functionalization process similar to the one used in [162]. The patterning of SWNT and VO_2 films was done by oxygen plasma etching and SF_6-based reactive ion etching, respectively. The mechanical release of the cantilever structure was done by isotropic etching of the silicon substrate using XeF_2 gas. The cantilever structure of photoactuators in this work are 400 μm long and 40 μm wide. **Figure** 6.4 shows the top view of released photoactuators with different SWNT films, and **Figure** 6.5 shows a cross section scanning electron microscope (SEM) image of the device. The thickness of all the SWNT films was in the vicinity of 100 nm.

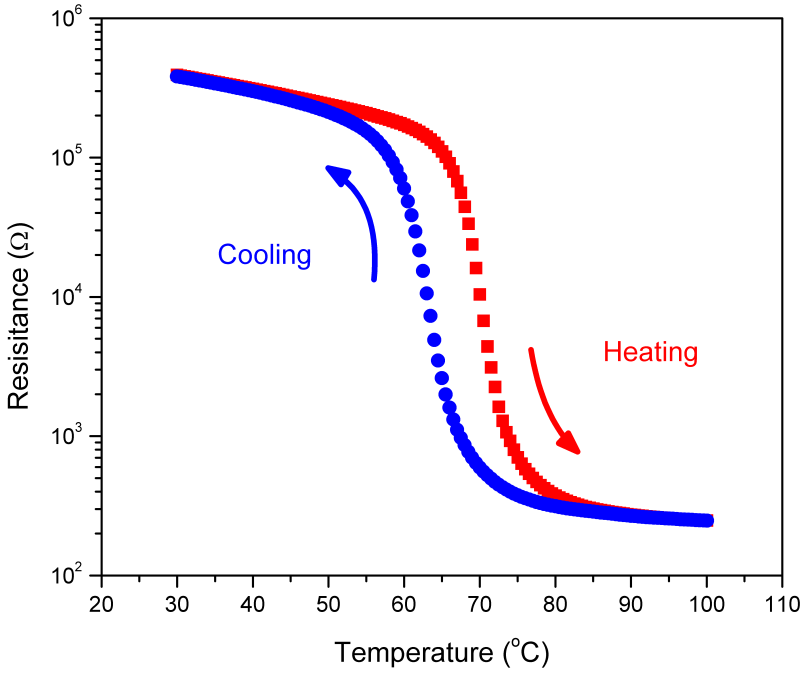

Figure 6.2: Resistance of VO_2 as a function of temperature.

6.2 Measurement Setup

Supplementary **Figure** 6.7 illustrates the setup for photothermal response measurement. Two semiconducting laser diodes with wavelengths of 660 nm and 985 nm were used for light illumination. It is noted that the shape and size of laser spots for each laser are different, which could result in uneven intensity distribution. In order to solve this problem, laser beams were coupled into single mode optical fibres (P2-630A-PCSMA-1 and P2-980A-PCSMA-1 from Thorlabs), which reshape the beam profiles and output standard single mode laser beams. Newport laser driver (Model 505B) controlled by Labview program was used to vary the driving current to the laser, and consequently its power output.

The sample was placed on top of a Petier heater mounted on a two dimensional translation stage which was used to align test samples with the laser beam. The temperature was controlled by Labview program through Thorlab temperature controller TED4015. Shown in **Figure** 6.7, CCD camera NO. 1 assists the alignment of laser sand samples, while CCD

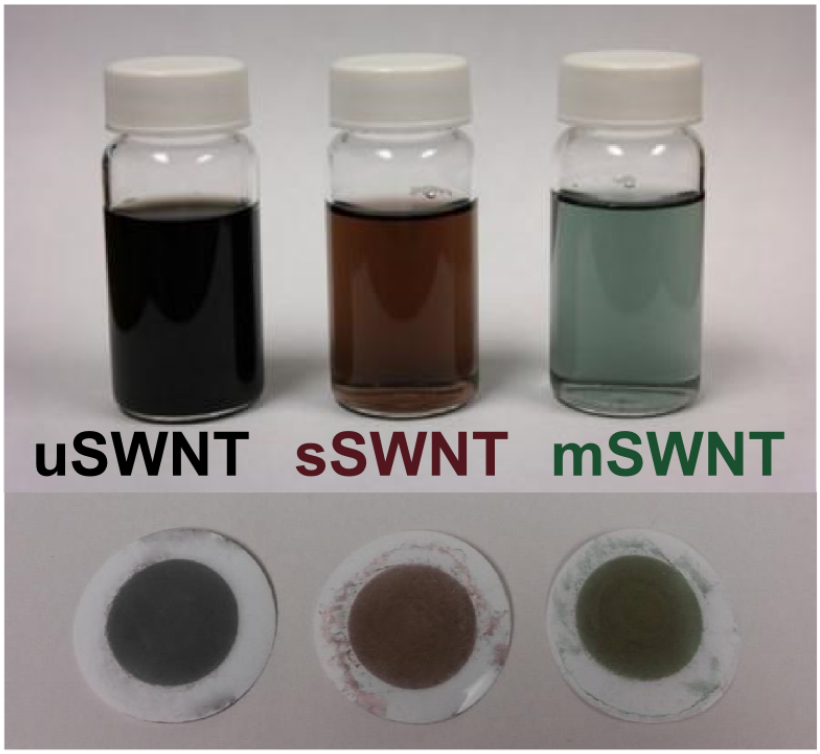

Figure 6.3: Optical images of unsorted SWNT, metallic SWNT, and semiconducting SWNT solution and SWNT/cellulose membranes made of SWNT solution by vacuum filtration. The scale bar here is 20 mm.

camera NO. 2, with the help of a high magnification lens (Mitutoyo, f=200 mm), monitors the actuators motion from side view. Between samples and driving laser, a lens was used to manipulate the diameter of the laser spot on test samples to be 500 μm (measured by a beam profiler Thorlab BP209-VIS, see **Figure** 6.6) for both wavelengths. Videos of CCD camera NO.2 containing displacement information were processed by Tracker software to track the movement of cantilevers tip during photothermal actuation and extract displacement data. For the time response measurement, a high speed camera (Nikon 1 with 1,200 fps) was used to for capturing displacement.

During the photothermal actuation, the laser spot was first aligned with actuators to have maximum displacement at a pre-heat temperature of 45 °C, then the laser was turned off. After the temperature of actuators was reset to 40 °C, the measurement was carried out by varying the power of laser illumination. After one photothermal measurement for one

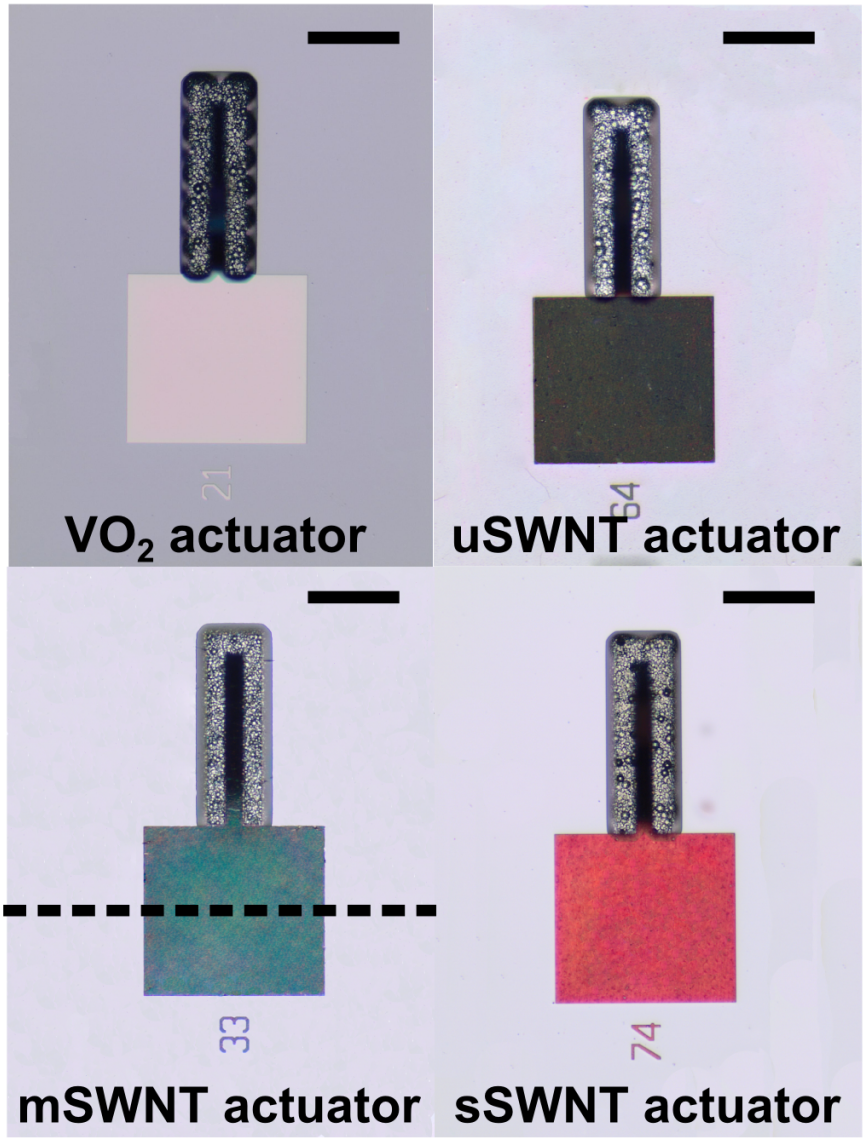

Figure 6.4: Top view microscope images of bare VO_2, VO_2/uSWNT, VO_2/mSWNT, and VO_2/sSWNT micro-actuators. All the cantilevers had the same length and width of 400 and 40 μm, respectively. The scale bars are all 200 μm.

wavelength, the fiber of new wavelength was installed on the fiber adapter that stay unchanged through this procedure. In this way, the positions of two laser of different wavelengths were maintained the same. In time response measurement, an external trigger signal (square wave with 25 ms pulse width and 50% duty cycle) was connected to laser current driver to generate shot laser pulses.

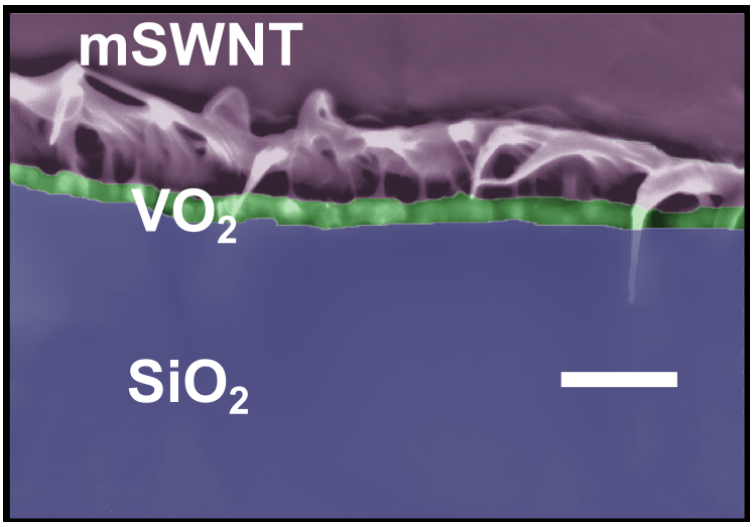

Figure 6.5: SEM image of a cross section of the VO_2/mSWNT actuators. Colors have been artificially modified for clarity. The scale bar in the SEM image is 200 nm.

6.3 Results

6.3.1 Temperature Response

Before performing the laser experiments, deflections of four types of actuators were measured as functions of temperature to verify the phase transition characteristics of VO_2 after the whole fabrication process, and to confirm that the structural phase transition of VO_2 is the dominating actuation mechanism. The results in **Figure** 6.8, show the deflection of all the actuators as the temperature was varied across the VO_2 phase transition (from 30 to 100 °C). It can be seen that all types of actuators (i.e. VO_2 and VO_2/SWNT actuators) show similar shape for the abrupt hysteretic behavior during the heating-cooling cycle. This proves that the dominant actuation mechanism in the SWNT-coated actuator is the stress generated during the phase transition of VO_2, and suggests that the advantages of VO_2-based actuators (e.g. large displacement and high energy density) are still present after SWNT coating.

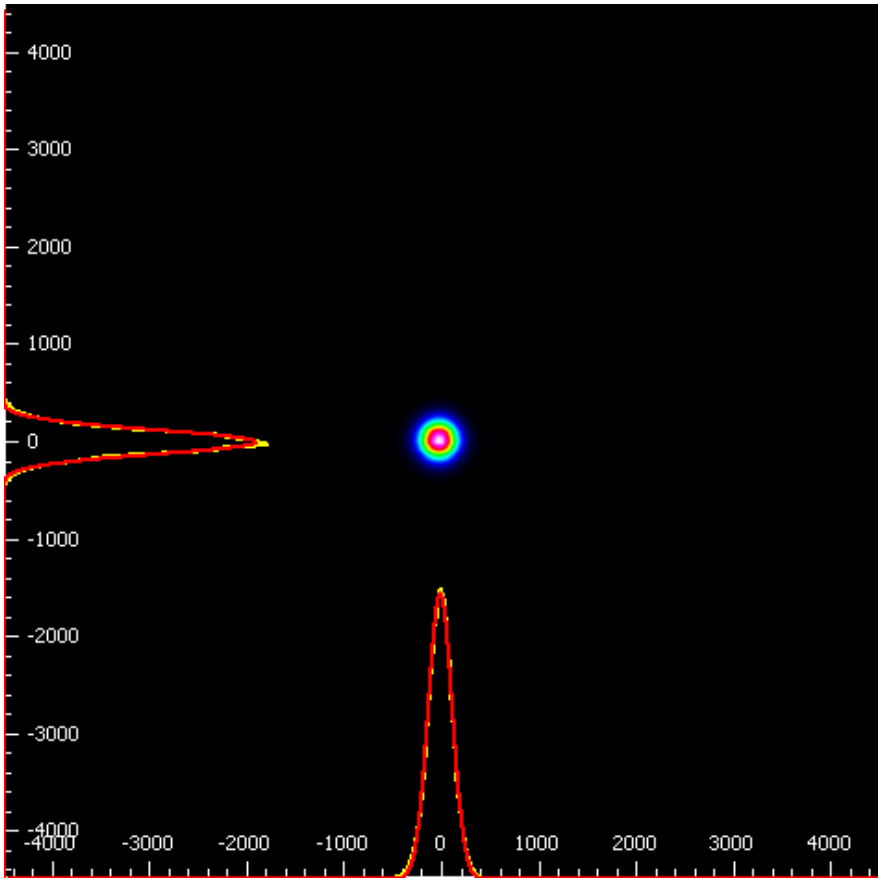

Figure 6.6: Beam profiles for the 660 nm laser on tested actuators. The beam profiles were measured by Thorlabs Dual Scanning Slit Beam Profiler BP209-VIS. The maximum intensity in the circular profile decayed by 13.5 % at a diameter of 500 μm in both x and y directions. Yellow curves represent real measured data, while the red curves are Gaussian fits.

6.3.2 Photothermal Response

The SWNT films in the photoactuators serve as a light absorber layer with absorption spectrum dependent on its chirality distribution. **Figure** 6.10 shows the absorption spectra of VO_2/uSWNT, VO_2/mSWNT, and VO_2/sSWNT films, indicating a near flat spectrum for VO_2/uSWNT and spectra with peaks for VO_2/mSWNT and VO_2/mSWNT at approximately 700 and 1,000 nm, respectively.

Figure 6.9a-d show the photothermal response of VO_2 and VO_2/SWNT actuators as a function of laser power, while the samples were kept at an initial temperature of 40 °C. It can be noticed that when the devices are actuated by conductive heating (**Figure** 6.8) the

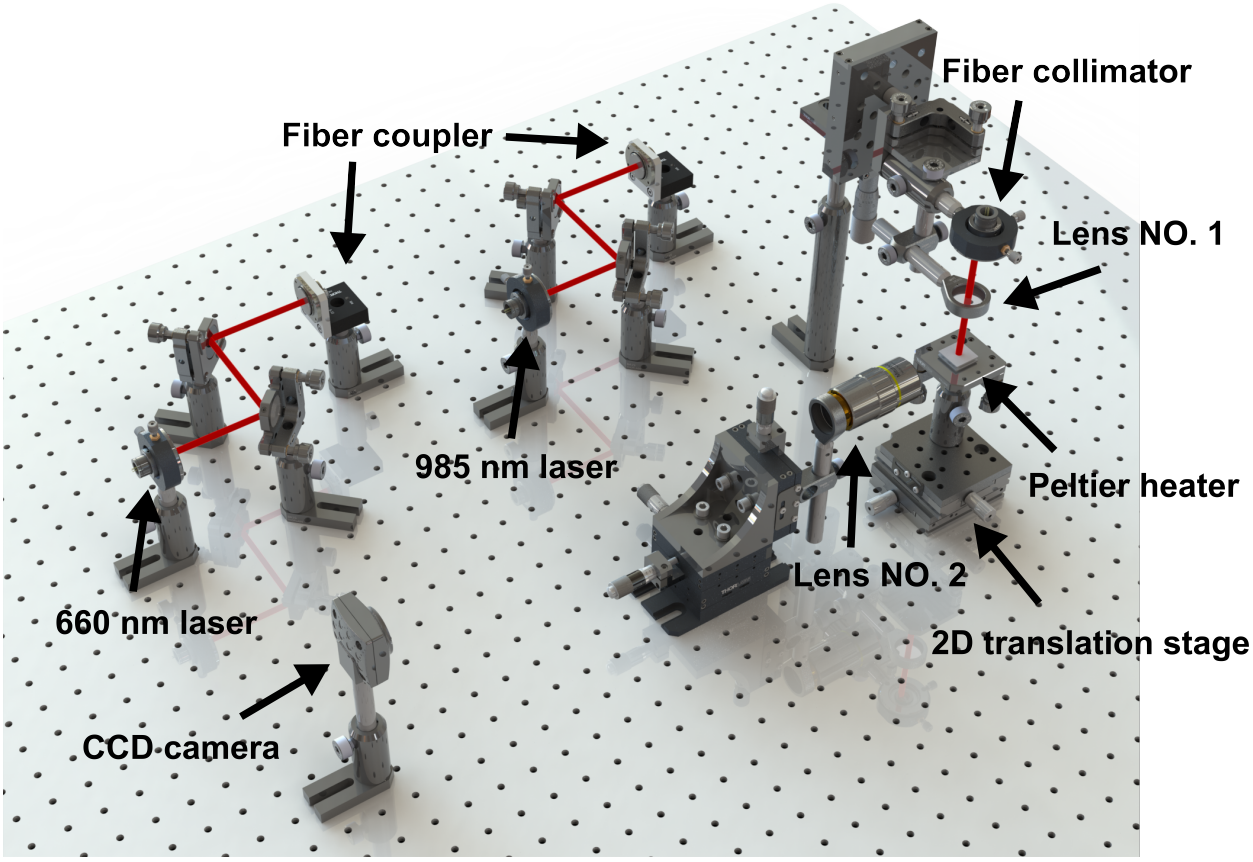

Figure 6.7: Schematic of setup used for photothermal and time response measurements. Two lasers are coupled into two single mode optical fibers, which are not shown in the diagram for clarity. Light coming out of the fiber collimator is focused by lens NO. 1 on the samples. The Peltier heater was used to control the temperature of the sample, either for pre-heating or conductive actuation experiments. CCD camera was used to record deflections of actuators with help of high amplification lens NO. 2.

maximum deflection is larger than that of photothermal actuation (**Figure** 6.9a-d). This difference is due to the fact that part of the heat generated during photothermal actuation is dissipated by the temperature gradient between the device and the substrate which is maintained at 40 °C this temperature gradient is much smaller for conductive heating. More importantly, once the substrate is brought to a given temperature by conductive heating, the bulk of the device acts as infinite heat reservoir; making the heat loss through the suspended cantilever structure negligible and increasing the uniformity of the temperature in the structure.

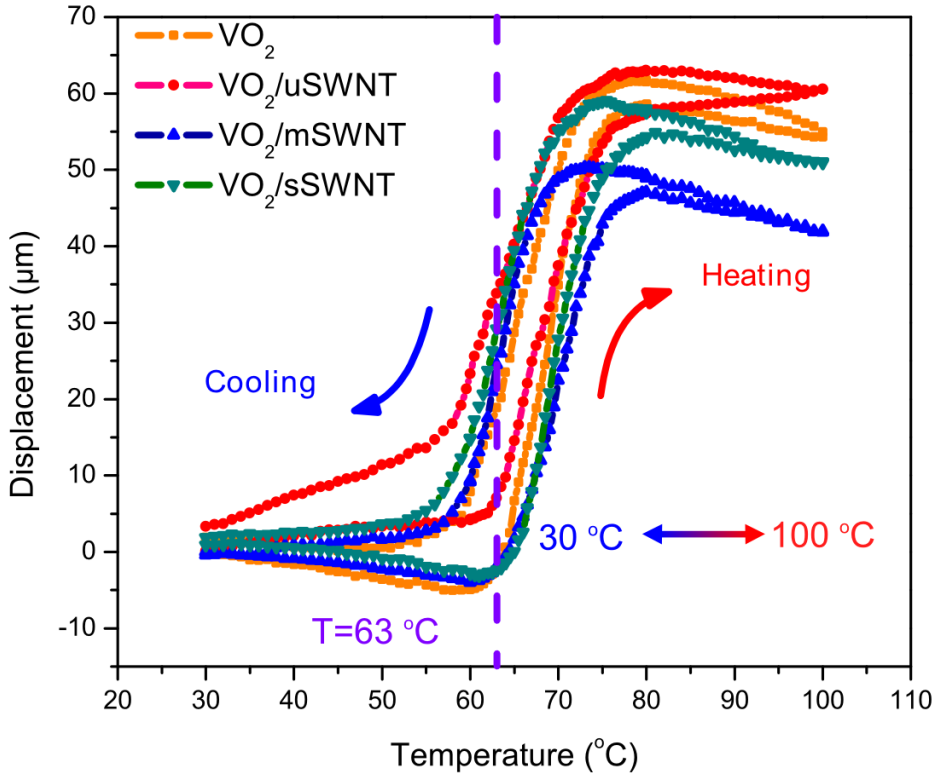

Figure 6.8: Measured displacement of all types of actuators as function of temperature. A Peltier heater in contact with the bottom of the silicon substrate was controlled to cycle the temperature from 30 to 100 °C.

The high absorption of SWNT films can be readily observed by comparing the results for the VO_2-based actuator (**Figure** 6.9a) with any of the VO_2/SWNT-based actuators (**Figure** 6.9b-d). Regardless of the different response for the two tested wavelengths, all VO_2/SWNT actuators require less laser power to reach the phase transition i.e. they have a lower "triggering power" (PT). It can be noticed that the VO_2-based actuator has lower PT for 660 nm laser illumination; but the rate of change in displacement per unit power (i.e. responsivity) during the phase transition of VO_2 is lower for 660 nm. At low temperature, VO_2 films show higher optical absorption at 660 nm than 985 nm; but the absorption spectrum of VO_2 changes during the transition, resulting in higher optical absorption at 985 nm than 660 nm (see **Figure** 6.11). This causes a crossover of the curves at a laser power of approximately 56 mW. On the other hand, VO_2/SWNT actuators photothermal response is mainly determined by the absorption properties of the SWNT film coating, which do not

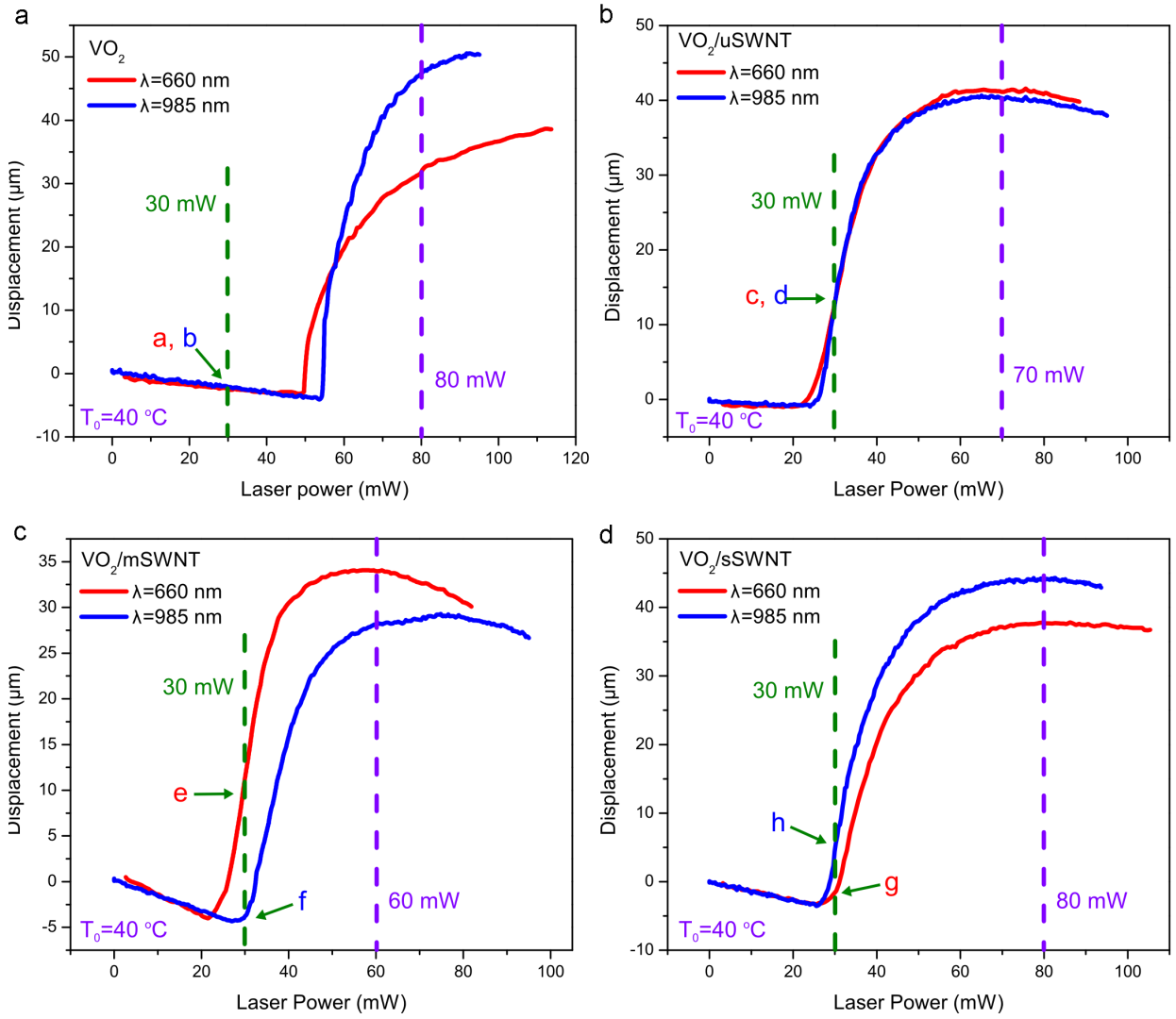

Figure 6.9: Photothermal response of VO_2/SWNT micro-actuators. Measured displacements as functions of laser power (660 nm and 985 nm) of (a) bare VO_2, (b) VO_2/uSWNT, (c) VO_2/mSWNT, and (d) VO_2/sSWNT actuators while the substrate temperature was set to 40 °C. The laser power used in time response measurements is marked by purple dash lines, while the laser power used for wavelength selective actuation is marked by green dash lines. The measured points, a, b, c, d, e, f, g, and h, correspond to **Figure** 6.12A-H.

show variations with temperature changes across the phase transition of VO_2.

6.3.3 Wavelength Selective Actuation

Due to the flat absorption spectrum of uSWNT film, the photothermal responses in VO_2/uSWNT for 660 nm and 985 nm wavelengths are practically overlapping (see **Figure** 6.9b). However,

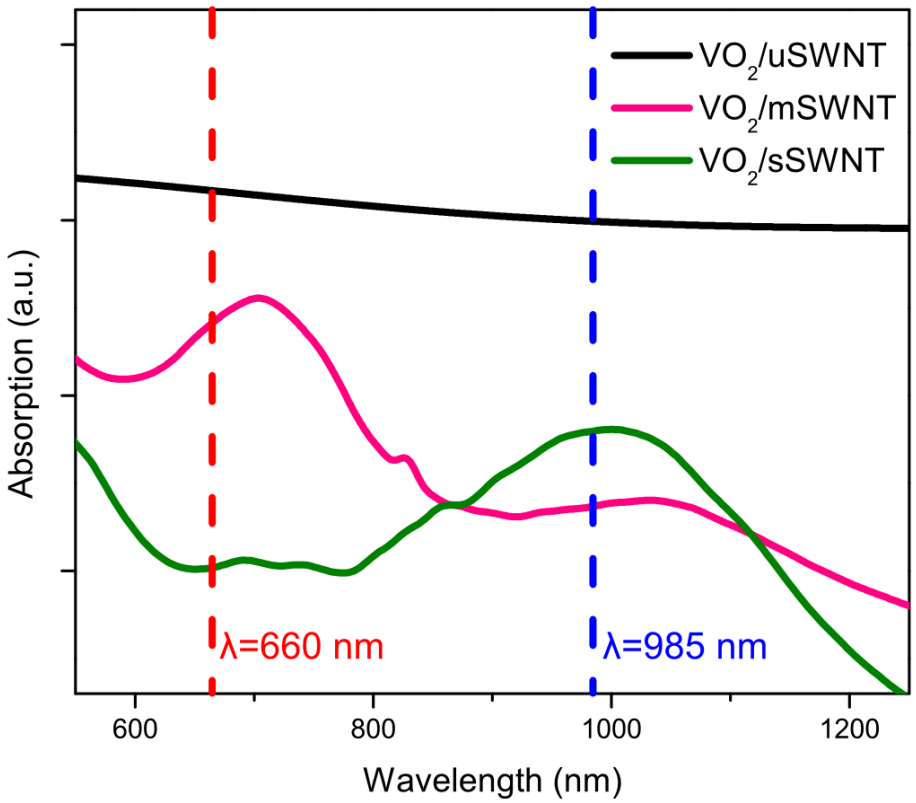

Figure 6.10: Measured optical absorption spectra of VO_2/uSWNT, VO_2/mSWNT, and VO_2/sSWNT films which compose of 50 nm thick VO_2 and 100 nm SWNT film. The two wavelengths (660 nm and 985 nm) used in this work are marked in the plot.

the VO_2/mSWNT and VO_2/sSWNT actuators show different responses for the two wavelengths used. It is clear that film absorption depends on the optical properties and thickness of the film. Therefore, although the absorption coefficient of mSWNT and sSWNT films is wavelength-dependent, this property can be masked by a large thickness see **section** 6.3.4 for details. We found that a thickness of 100 nm was enough to maintain a continuous SWNT film with wavelength-dependent absorption spectrum. To study the wavelength-selective response of VO_2/mSWNT-based actuators, both wavelengths were tested on the same device, so differences in response are not caused by differences in film thickness of either mSWNT or VO_2. Furthermore, by comparing the responses of a device with a given initial deflection, we have the same illuminated surface area, and consequently the same delivered power for both wavelengths.

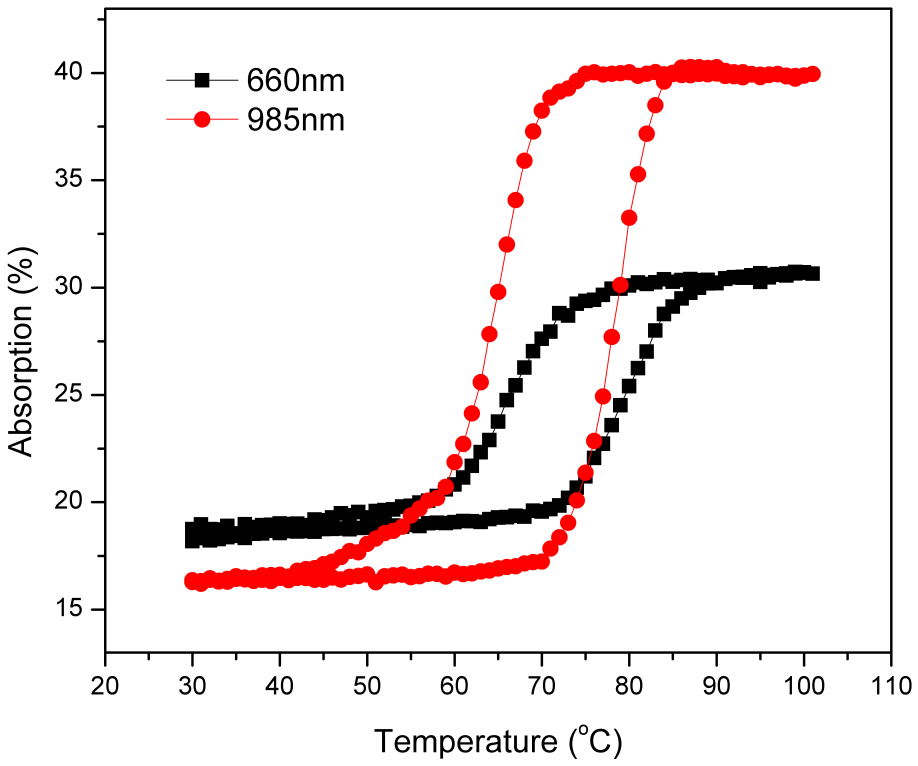

Figure 6.11: Light absorption of VO_2 thin film. The VO_2 film was deposited on SiO_2 substrate, and the absorption was measured as a function temperature for wavelengths of 660 nm and 985 nm. Absorption (Ab) was calculated by measuring transmittance (Tr), reflectance (R), and then using $Ab = (1 - Tr - R) \times 100\%$.

The separations between photothermal response curves in **Figure** 6.9c and **Figure** 6.9d are attributed to the wavelength-dependent absorption coefficients of metallic and semiconducting SWNT films. Due to the optical absorption peak around 700 nm for mSWNT films (see **Figure** 6.10) and all other parameters being equal, the temperature increase for mSWNT will be higher for illumination from the 660 nm laser. Thus, VO_2/mSWNT actuators will have a lower P_T for illumination from the 660 nm laser (see **Figure** 6.9c). Conversely, sSWNT films have better absorption for 985 nm, which translates into a lower PT for illumination from the 985 nm laser (see **Figure** 6.9d). Furthermore, the responsivity across the phase transition is higher for 660 nm illumination in the VO_2/mSWNT actuator; and for 985 nm in the VO_2/sSWNT actuator. Therefore, energy from light is being absorbed and converted to heat more efficiently for the wavelength of higher absorption across

Table 6.1: Light responsivity during phase transition. The responsivity is calculated from an estimate of the slope of displacement versus light power curve for the linear region across the phase transition in **Figure** 6.9.

λ (nm)	Responsivity (μm/mW)		
	VO_2/uSWNT	VO_2/mSWNT	VO_2/sSWNT
660	2.74	3.13	2.48
985	2.74	2.00	3.51

the entire VO_2 s phase transition range. **Table** 6.1 summarizes the responsivity between wavelengths for all the SWNT coated devices.

The wavelength-selective response of the present devices is better visualized in the **Figure** 6.12. A laser power of 30 mW was used for both lasers (660 nm and 985 nm), as labelled in **Figure** 6.9a-d. This power is much lower than the P_T for the bare VO_2-based micro-actuator, and therefore the device shows negative displacements (i.e. displacements towards the substrate) for both wavelengths (**Figure** 6.12A and B), which is induced by the mismatch between thermal expansion coefficient of VO_2 and SiO_2 note that the VO_2 thin film has a higher thermal expansion coefficient than SiO_2. In contrast, VO_2/SWNT actuators have much higher photothermal efficiency, than bare VO_2-based actuators. The VO_2/uSWNT actuator shows very similar displacement for both wavelengths (in **Figure** 6.12C and D), which is consistent with the absorption spectrum in **Figure** 6.10. VO_2/mSWNT actuators are more responsive to 660 nm illumination, and therefore show a larger deflection (almost four-fold) for this wavelength (see **Figure** 6.12E and F). On the other hand, VO_2/sSWNT actuators show larger deflections for the 985 nm laser. The still images in **Figure** 6.12G and H show how a laser power of 30 mW for both laser wavelengths generates displacements in opposite directions for the VO_2/mSWNT and VO_2/sSWNT-based actuators.

6.3.4 SWNT Film Thickness and Wavelength Selectivity

The band structure of SWNT with selective chirality endows the material with intriguing wavelength selective optical properties (shown in **Figure** 6.10). However, the optical ab-

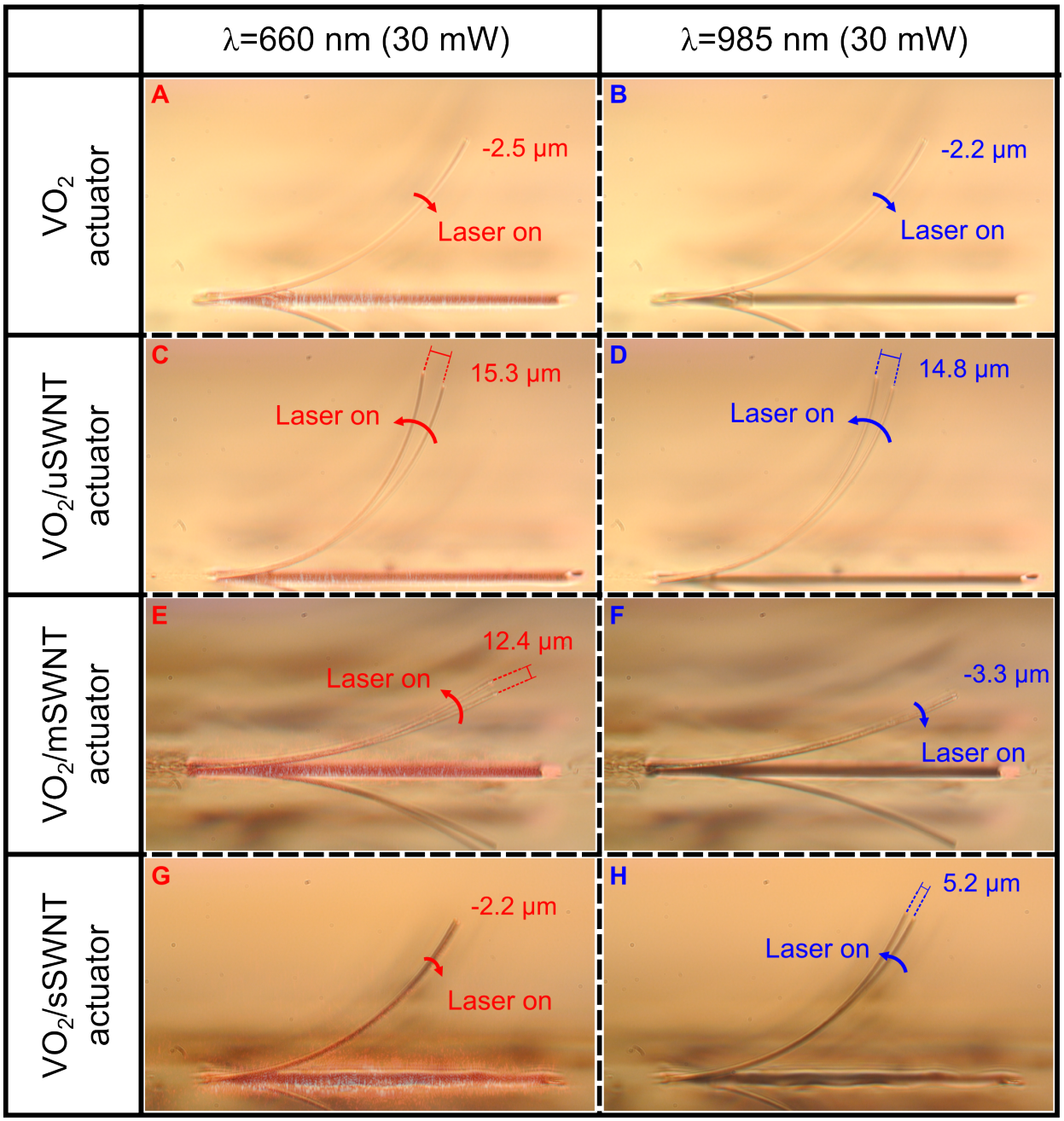

Figure 6.12: Wavelength selective actuation. Light response of the four different actuators for pulses from both lasers (660 nm and 985 nm). For each wavelength, the power was calibrated to maintain the same delivered power of 30 mW that is marked in **Figure** 6.9 with green dash lines, while the substrate temperature is maintained constant at 40 °C.

sorption is not the only parameter that influences absorption in a thin film. According to Beer-Lamberts law, the transmittance across a film decreases with the films thickness. For a SWNT film with specific chirality distribution, the absorption of all wavelengths increases

as the film gets thicker. Eventually, the absorption of all wavelengths will saturate (close to 100%), and the wavelength selective spectrum will become indistinctive. Here, we studied the relation between SWNT film thickness and its absorption spectrum, which allowed for the design of a film thickness suitable for our devices.

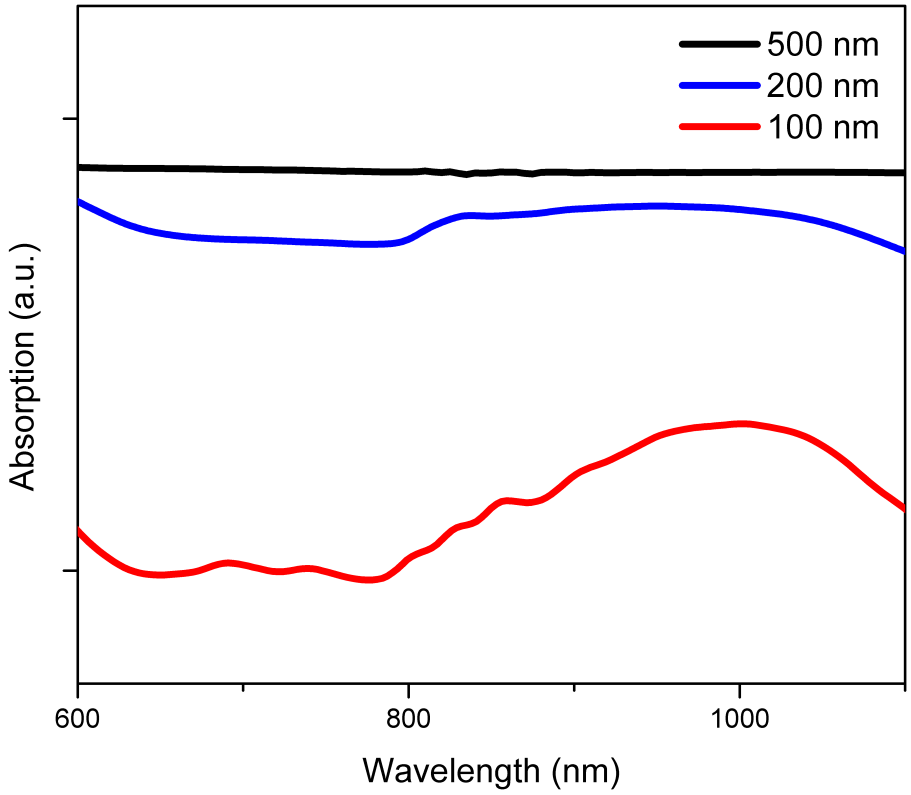

Figure 6.13: Absorption spectra of semiconducting SWNT films for different thickness. The wavelength selectivity of semiconducting SWNT thin film degrades as the thickness increases.

As an example, the absorption spectrum of semiconducting SWNT films for different thickness is shown in **Figure** 6.13. For 100 nm thick semiconducting SWNT film, the spectrum shows an absorption peak at 1000 nm, while for 200 nm thick film, the absorption peak becomes almost unnoticeable. For 500 nm thick film, most of the light is absorbed by the film regardless of the wavelength, causing a near flat spectrum and no wavelength selectivity. Given this relation between wavelength selectivity and film thickness, we used 100 nm thick SWNT film to fabricate the wavelength selective micro-actuators. It should also be noticed that thinner films could give better wavelength selective spectrum shape,

but then the total absorbed power will also decrease; thus increasing the laser intensity requirement for inducing the phase transition of the VO_2 thin film.

The optical absorption of SWNT thin films are determined by two factors, thickness (d) and attenuation coefficient (σ). The absorption rate can be expressed as $Ab = (1 - Tr - R - Sc)$, where Ab is absorption rate, Tr is transmittance, and Sc is scattering. Assuming $Ab + Tr \gg Sc$), then the equation can be simplified as $Ab \approx (1 - Tr - R)$. Based on Beer-Lambert law, the absorption rate that is dependent on wavelengths in the case of SWNT films can be expressed as a function of thickness and attenuation coefficient in the following way:

$$Ab(\lambda, d) = 1 - e^{-\sigma(\lambda)d} \tag{6.1}$$

The wavelength selectivity of a film can be quantitatively characterized as the difference of absorption for two wavelengths, as shown below:

$$\Delta Ab = Ab(\lambda_1, d) - Ab(\lambda_2, d) = e^{-\sigma(\lambda_2)d} - e^{-\sigma(\lambda_1)d} \tag{6.2}$$

Then the partial derivative of ΔAb with respect to the variable d can be expressed as:

$$\frac{\partial \Delta Ab}{\partial d} = \sigma_1 e^{-\sigma(\lambda_1)d} - \sigma_2 e^{-\sigma(\lambda_2)d} \tag{6.3}$$

where $0 \leqslant d \leqslant \infty$; and $\sigma(\lambda_1)$ and $\sigma(\lambda_2)$ have been re-defines as σ_1 and σ_2, respectively. Assuming $\sigma_1 > \sigma_2$, the plot of **Equation** 6.2 and 6.3 are qualitatively shown in **Figure** 6.14.

When $\frac{\partial \Delta Ab}{\partial d} = 0$, ΔAb reaches the highest point. Solving **Equation** 6.3 equal 0 for "d" results in the thickness for highest absorption difference for two wavelengths, which is

$$d = \frac{ln(\frac{\sigma_1}{\sigma_2})}{\sigma_1 - \sigma_2} \tag{6.4}$$

The attenuation coefficient of SWNT films can be estimated from the measured absorbance (see **Figure** 6.13) by using $\sigma = \frac{Aln(10)}{d_100}$, where d_100=100 nm (thickness of the SWNT films in the experiments), and A is the measured absorbance. Using the estimated attenuation coefficient for a thickness of 100 nm, we can then estimate the optimal thickness for

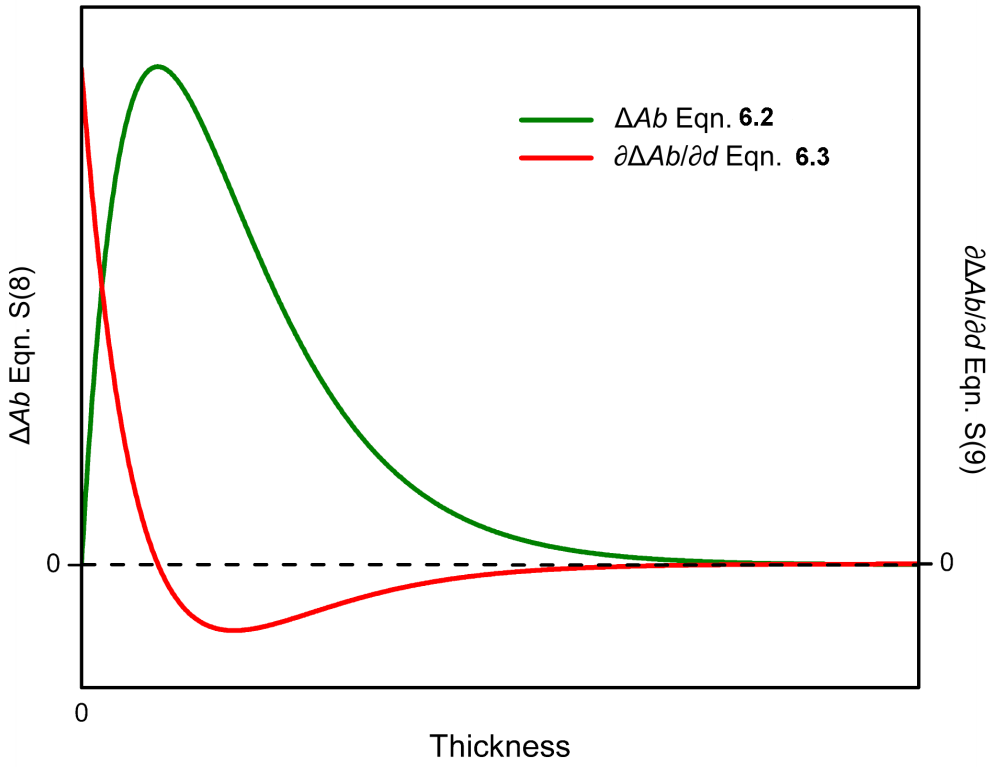

Figure 6.14: Wavelength selectivity as a function of thickness. The largest difference in absorption for two wavelengths occurs when the thickness of mSWNT or sSWNT films is 119 and 91 nm, respectively.

mSWNT and sSWNT films to be d_m=119, and d_s=91 nm, respectively. For experiments, we chose a thickness of 100 nm, which is approximately a midpoint.

6.3.5 Time Response

For most conventional thermal micro-actuators, the actuation mechanism is based on thermal expansion of materials. The total displacement of actuators operated on this principle is proportional to the product of the difference in thermal expansion coefficient of the materials involved ($\Delta\alpha$) and the temperature change (ΔT). Since the $\Delta\alpha$ is inherently limited to values lower than $2x10^{-5}K^{-1}$ for metal-ceramic bimorphs [163], and to values in the vicinity of $2x10^{-4}K^{-1}$ for polymer-silicon bimorphs [80], the needed ΔT for generating large deflections is relatively high. Moreover, a larger ΔT requirement typically results in slower devices [63,

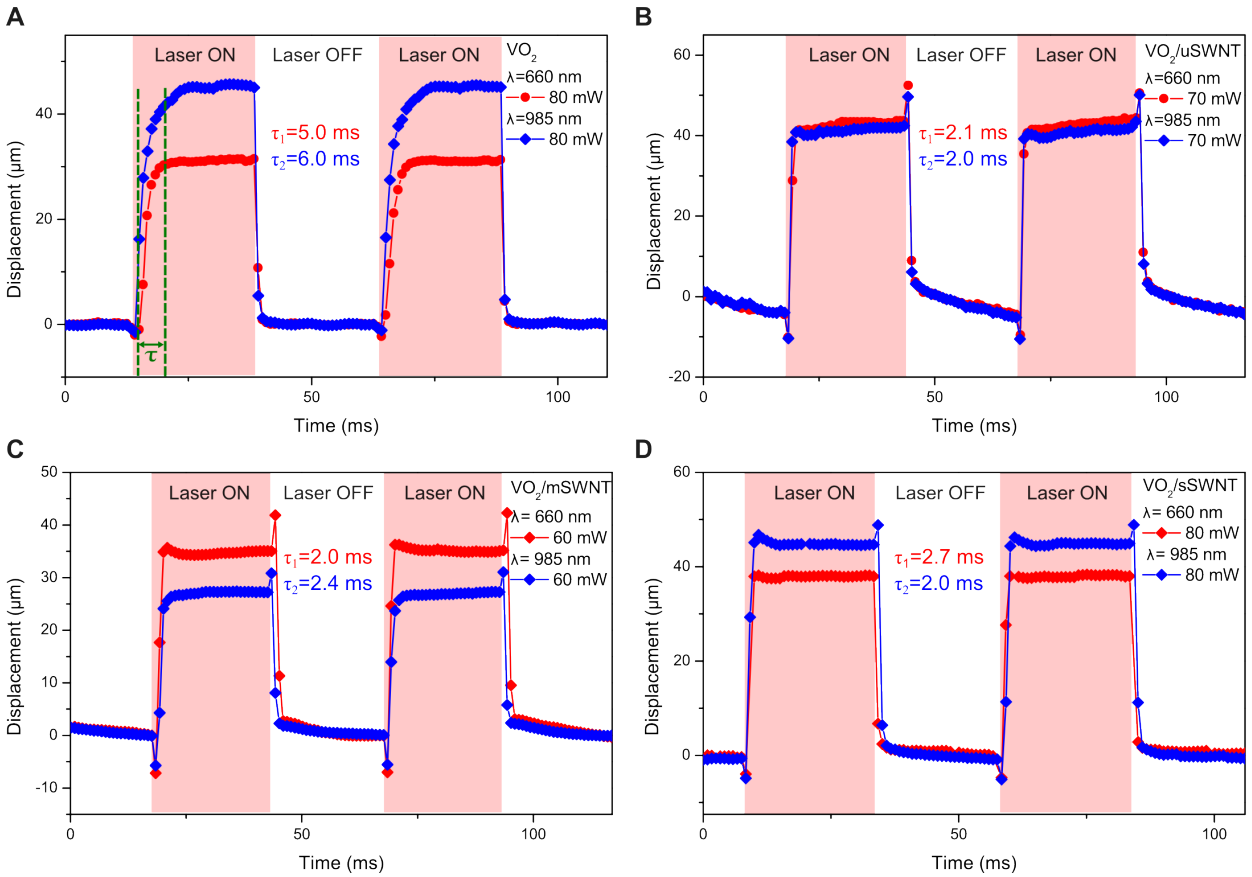

Figure 6.15: Time response of VO2/SWNT actuators. (A) Measured displacements of (A) bare VO_2, (B) VO_2/uSWNT, (C) VO_2/mSWNT, and (D) VO_2/sSWNT actuators as lasers are turned on and off by controlling driven current. The pulse duration is 25 ms for all tests. The power used in time response is also marked in **Figure** 6.9 with purple dash lines. The response times show that VO_2/SWNT-based actuators are much faster than the uncoated device, and the wavelength-selective actuators respond faster to the better-absorbed wavelength.

64]. Large displacements often require very large temperature changes (ΔT) and are therefore slow [63, 64]. In contrast, VO_2-based actuators rely on the materials phase transition, which happens at about 68 °C and typically spans over a temperature window of only 5 10 °C. Due to the lower ΔT required for full actuation, VO_2-based actuator devices are much faster than similar designs based on thermal expansion mechanisms. In this work, the time response of all types of actuators was captured by a high speed camera (1,200 fps), and the deflection is plotted as a function of time for pulses of different illumination power from both lasers (see in **Figure** 6.15). Before actuation, the samples were pre-heated to 40 °C. The laser

pulse duration in all the plots are 25 ms, and the power used is marked in **Figure** 6.9. It should be noted that the laser power used for the time response experiments for the three different SWNT films (purple vertical dashed lines in **Figure** 6.9b-d and labeled power in **Figure** 6.15) is different. This is done in order to be able to calculate the time response of each device. Each type of SWNT film absorbs each wavelength differently. Therefore, the required amount of power to completely go through the transition region and achieve full actuation will be different for each type of SWNT film. Since the response time is the required time for achieving full actuation, it was necessary to use the power that resulted in full actuation for each device. The bare VO_2 actuator was not fully driven across the phase transition due to power limitations of the lasers used. The response time is calculated as the time required for the displacement to rise from 10% to 90% of the stable value. All the VO_2/SWNT-based actuators are approximately twice as fast as the uncoated VO_2-based actuator. Furthermore, when comparing the time responses for the VO_2/mSWNT and VO_2/sSWNT, it is observed that each device responds faster to the wavelength that is better absorbed by the corresponding SWNT film.

It should be noted that the photothermal process is slower than the mechanical actuation process, which means that the time response of the photoactuators presented here will be ultimately limited by the speed with which the absorbed power is converted to heat, and not by the mechanical properties of the device. This is expected because heat transfer in solids is in general much slower than the speed of sound in the material. A model that allows for estimating the time response is discussed in the Supplementary Materials section.

6.3.6 Photothermal Actuation Mechanism

A model based on finite element method (FEM) was created in COMSOL with physics of "Heat Transfer" and "Solid Mechanics". The phase transition of VO_2 was modelled by a

temperature dependent thermal expansion coefficient $\alpha(T)$ [164]:

$$\alpha(T) = \frac{6 \times 10^{-6}}{1 + e^{-0.2(T-226.15)}} - 3 \times 10^{-8}(T - 273.15) + 6.9 \times 10^{-6} \tag{6.5}$$

which is obtained from a curve fit to the experimental measurement. A heat influx on the surface of actuators acts as the light illumination, while the anchor was set to be 40 °C same as experiments. The air convection was applied to the model with convection cooling coefficient hair which is a function of dimensions of the device and calculated by the software. The parameters used in the model are summarized in **Table** 6.2.

Table 6.2: Material properties used in FEM model. The thermal expansion coefficient of VO_2, $\alpha(T)$, is a function of temperature T.

	VO_2 [164]	uSWNT [5, 165]		
Density(kg/m^3)	4670	1500		
Young's modulus (GPa)	140	1.5		
Thermal conductivity ($W \cdot m^{-1} \cdot K^{-1}$)	5	uSWNT	mSWNT	sSWNT
		242	121	191
Thermal expansion coefficient (K^{-1})	$\alpha(T)$	3×10^{-6}		
Specific heat ($J \cdot kg^{-1} \cdot K^{-1}$)	700	550		

First, a "Stationary" study was performed to calculate the stabilized temperature distribution on the actuators with laser irradiation. The light intensity distribution on the actuators is complicated as a result of beams Gaussian profile and unknown exact location of the laser spot. Hence, we assume that heat influx intensity is uniform in the model, and fitted the simulated deflection with the measured deflection, matching the power used in the experiments. The results are shown **Figure** 6.16 with temperature distribution on the actuators surface, along the cantilevers length, and for different devices.

In order to study the dynamic performance of this type of actuators, we studied the photothermal and mechanical processes. For obtaining the time response associated with the photothermal mechanism, the following heat transfer **Equation** 6.6 is used:

$$\rho C_p \frac{T}{t} = \nabla \cdot (k \nabla T) + Q \tag{6.6}$$

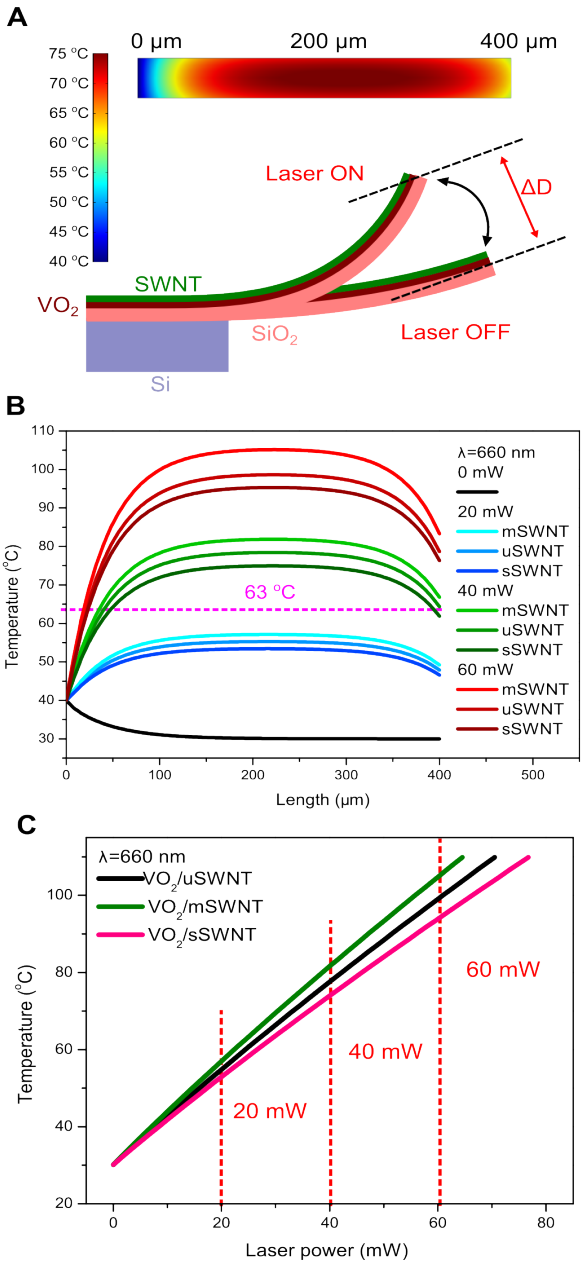

Figure 6.16: Photothermal effects. (A) A schematic of the micro-actuator model used in the COMSOL simulation. When illuminated, the actuator is locally heated resulting in displacement of ΔD. Here, the anchor of the structure is fixed and maintained at a temperature of 40 °C, same as the experiments. The inset shows the surface temperature distribution of VO_2/uSWNT actuator under 660 nm laser illumination of 30 mW. (B) Calculated temperature distribution along actuators length (400 μm) under 660 nm laser irradiation with different laser power. The phase transition temperature of VO_2 is 63 °C marked by purple dash line. (C) Calculated temperature at the length of 300 μm of actuators as a function of laser power (660 nm). Purple dash lines represent the power plotted in (B).

where ρ is density of VO_2 and SWNT film, C_p is the specific heat, T is temperature, t is time, k is thermal conductivity, and Q contains all heat source. The convective cooling of air and light illumination were introduced by following **Equations** 6.7 and 6.8:

$$-\mathbf{n}\cdot(-k\nabla T) = h_{air}(T_{ext} - T) \tag{6.7}$$

$$-\mathbf{n}\cdot(-k\nabla T) = I_{light} \tag{6.8}$$

where $\boldsymbol{n}$ is normal vector of the surface, h_{air} is air convection cooling coefficient that is a function of structure geometry, T_{ext} is external temperature, and I_{light} is the laser intensity on the actuators. **Figure** 6.17 shows the time dependent temperature curve of VO_2/uSWNT, VO_2/mSWNT , and VO_2/sSWNT actuators, in which the step input light illumination (40 mW) was applied at 5 ms. The response time that enables 90% of full actuation, is calculated to be 2.65, 3.0, and 2.82 ms, respectively.

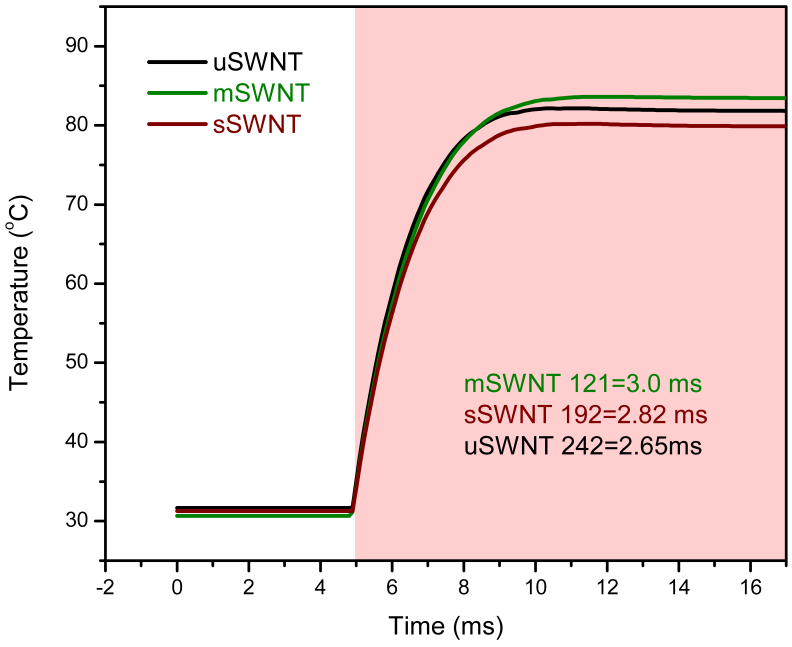

Figure 6.17: Simulated temperature changes of the actuator tips as a function of time. The step input of light illumination is applied on actuators at 5 ms.

For obtaining the time response associated to the structures mechanical behavior, we studied structural resonance frequencies. Here, the "Eigenfrequency" study in COMSOL was used to characterize VO_2/uSWNT actuators mechanical resonance frequencies. It is important to notice that additional stress and strain inside the structure caused by temperature increase during actuation could change its resonance frequencies. Therefore, the initial values including temperature, displacement, and stress for "Eigenfrequency" study were imported from a "Stationary" study under same light illumination (40 mW). The first resonance frequency mode ω_n calculated is 6 kHz, and for a second order underdamping system ($0 < \zeta < 1$) the rise time τ of an unit step input can be approximated to **Equation** 6.9 [166]:

$$t_r \cong \frac{1 - 0.4167\zeta + 2.917\zeta^2}{\omega_n} \tag{6.9}$$

indicating a fast response time in the range of $0.16ms < \tau < 0.6ms$. Clearly, the thermal process dominates the response time for the photothermal actuation of these devices, and a faster response is obtained by improving the photothermal process, which in this work is achieved by the higher absorption of SWNT films (see **Figure** 6.15).

Photothermal actuation process is analysed in two steps. First, the light is absorbed by the SWNT films and converted to thermal energy. This process is mainly determined by the optical properties of SWNT films, and it is the process that allows for the wavelength-selective added multifunctionality of the reported devices. The second step involves the distribution of thermal energy over the actuator structure. Thermal conductivity and heat capacity of the structural materials (i.e. SWNT films, VO_2 layers, and SiO_2) play a role in the photothermal process.

Since both processes occur simultaneously, it is very difficult to analyse them individually by using experimental studies. Thus, two finite element method simulations were performed: one using different values for heat capacity (while keeping the thermal conductivity constant), and another using different values for thermal conductivity (while keeping the heat capacity constant).

Heat capacity variations: The heat capacity used in the manuscript for all the SWNT films is $550 J/(kg \cdot K)$, which is the value for uSWNT films [5]. The heat capacity values for the other films (i.e. mSWNT and sSWNT) is not available in the literature. However, in order to study the effects of possible changes in the time response due to different heat capacities between SWNT films, we proceeded to run simulations for three different heat capacity values: 350, 550, and 750 $J/(kg \cdot K)$. **Figure** 6.18 shows the temperature increase for the three cases as a function of time for the same input. It can be noticed that the curves are almost overlapping, with the largest difference in response time being only 0.09 ms, which is found between the 350 and 750 $J/(kg \cdot K)$ curves. This means that doubling the heat capacity only produces a change in the time response of about 3%. Therefore, variations in the heat capacity of the SWNT films have little effect on the response time.

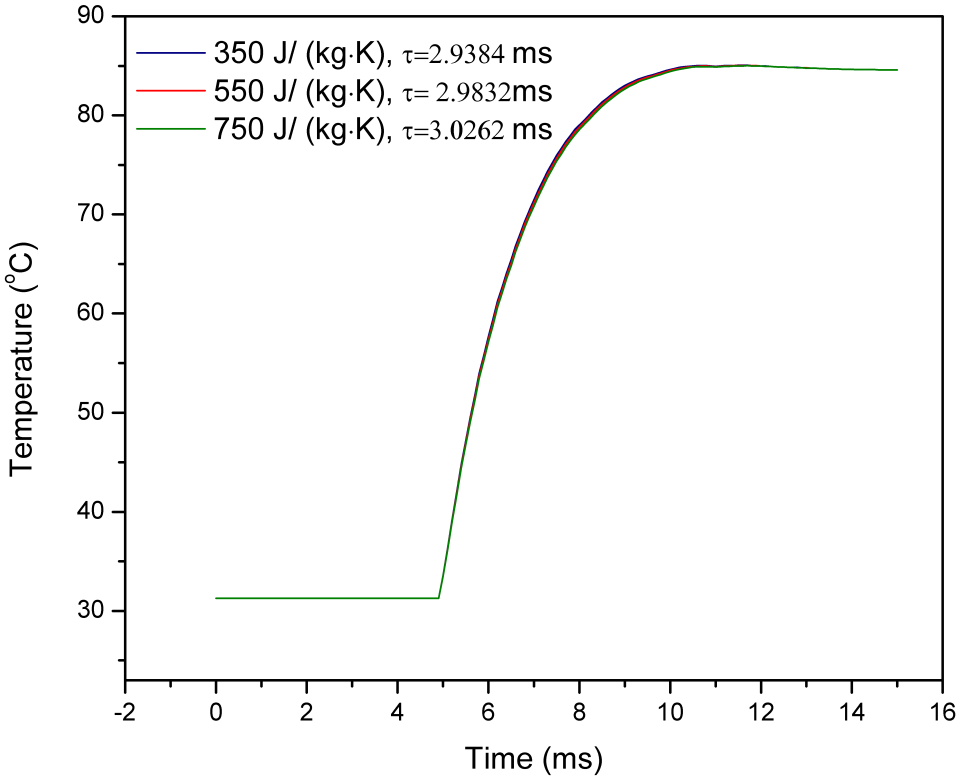

Figure 6.18: Photothermal response for SWNT films with different heat capacity. The difference in response time for the SWNT actuators is not significantly influenced by the heat capacity of the SWNT film. An increase in heat capacity from 350 to 750 $J/(kg \cdot K)$ changes the time response by only 3%.

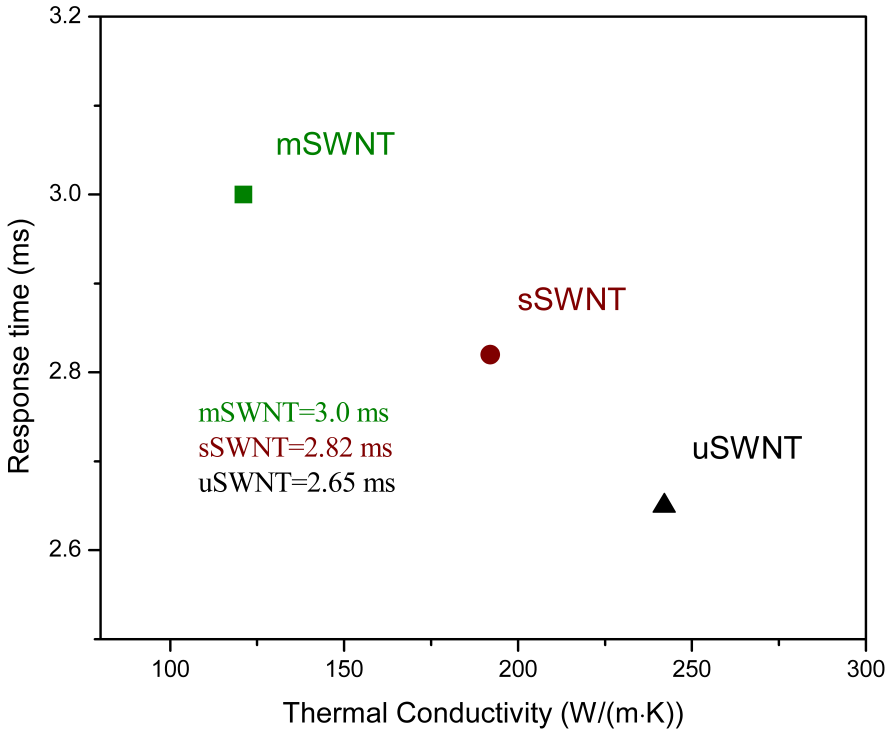

Figure 6.19: Photothermal response for SWNT films with different heat capacity. The difference in response time for the SWNT actuators is not significantly influenced by the heat capacity of the SWNT film. An increase in heat capacity from 350 to 750 $J/(kg \cdot K)$ changes the time response by only 3%.

Heat capacity relates to the amount of energy that is required to increase the temperature of a given mass of the material -it should be noted that heat capacity does not play a role in the final equilibrium temperature. With constant incident illumination power (constant absorbed heat), SWNT films with lower heat capacity require less energy to increase temperature, and therefore reach equilibrium temperature faster. This is why the response time increases with heat capacity. However, the role of heat capacity in the time response in our devices is mostly dominated by the VO_2 and SiO_2 layers the difference in heat capacities of the different SWNT has very little effect on determining the time response of the device. Assuming the average temperature increase of the actuators is ΔT, the absorbed optical energy power is h_l, and the average power of heat loss power through conduction at

the anchor and convection of the surfaces is H_{cc}, the total energy required to complete the heating process can be expressed as following equation:

$$E = (\rho_{SWNT} C_{SWNT} d_{SWNT} + \rho_{VO_2} C_{VO_2} d_{VO_2} + \rho_{SiO_2} C_{SiO_2} d_{SiO_2}) S \Delta T = \tau (h_l - h_{cc}) \tag{6.10}$$

where ρ is the density, C is heat capacity, S is surface area, d is the thickness of different layers, and τ is the response time. The SWNT films are only 100 nm thick, and have a density of 1500 kg/m^3. The VO_2 and SiO_2 layers, on the other hand, are 50 nm and 1000 nm thick; have densities of 4670 and 2200 kg/m^3; and their heat capacities are 700 and 730 $J/(kg \cdot K)$, respectively. This means that VO_2 and SiO_2 layers play a much more important role in determining the energy required to reach equilibrium temperature; and explains the small change in time response (only 3%) for an increase in heat capacity from 350 to 750 $J/(kg \cdot K)$.

Thermal conductivity variations: We ran simulations using the new thermal conductivity values: 121, 192, and 242 $W/(m \cdot K)$ for the mSWNT, sSWNT, and uSWNT, respectively; while keeping all the other simulation parameters equal (the heat capacity used for the simulations is 550 $J/(kg \cdot K)$). **Figure** 6.19 shows the response times obtained from the simulation, and the corresponding response curves are shown in **Figure** 6.17. It can be noticed that the response time decreases with thermal conductivity. The response times are 3.0, 2.82, and 2.65 ms, for the mSWNT, sSWNT, and uSWNT devices, respectively. Higher thermal conductivity can help distribute the heat faster across the actuator. As a result, the temperature settling time is smaller, meaning lower thermal response time.

6.4 Summary

In summary, the present work demonstrates wavelength-selective VO_2/SWNT photothermal micro-actuators that combine the high performance of VO_2-based actuators with the superb optical properties of SWNT, resulting in energy efficient micro-devices with high speed, large deflections, and wavelength-dependent response multifunctionality. The device

fabrication is compatible with standard MEMS fabrication technologies and the properties of the VO_2 or SWNT films are maintained in the process. This allows for the integration of the present devices into larger MEMS transducers or systems that involve components defined by conventional micro-lithography. The present device can find applications in monochromatic sensors such as portable spectrometers and enable optically-triggered micro-electro-mechanical devices where MEMS-based logic gates, multiplexers, and decoders can be controlled by light pulses. Furthermore, the present work suggests that the response of VO_2 based photo-sensors or bolometers which are very sensitive due to the large change in VO_2 s resistance with temperature can be made wavelength-dependent by using SWNT film coatings. The measurements reported in this work could be extended to include more wavelengths by using single chirality SWNT films with sharper absorption peaks than metallic and semiconducting SWNTs.

CHAPTER 7

SUMMARY

7.1 Summary of Contributions

In this work, a new type of photo-thermal actuator based on SWNT and VO_2 is presented. Compatible fabrication process of SWNT thin film and VO_2 is explored and developed. Continuous and uniform SWNT film can be made by vacuum filtration, and a SWNT film transfer process is developed based on acetone vapour bath. O_2 plasma etch is used to pattern SWNT film, while VO_2 stays intact. A preliminary set of studies that involved conduction heating actuation, photo-thermal actuation, dynamic deflection performance, and wavelength selective actuation are performed. The results obtained from these studies suggest that SWNT coated VO_2 micro-actuators possess advantages over VO_2 only actuators in terms of power consumption, optical responsivity, and dynamic response. Moreover, VO_2 micro-actuators coated SWNT thin films with various SWNT chirality distribution (semiconducting and metallic SWNT) were fabricated and tested, which implements wavelength selective actuation. A detailed FEM model is built to describe the photo-thermo-mechanical process of VO_2/SWNT photothermal actuators. The effect of thermal conductivity, heat capacity, and thickness are studied to optimize wavelength selectivity. This new type of wavelength selective photothermal actuators make it possible to implement micro-spectrometer, micro-robotics, and remote control devices.

7.2 List of Problems Solved in This Thesis

This work addresses the following:

1. Synthesized SWNT thin films by vacuum filtration technique. Pore size of filter membranes and vacuum pressure have been studied to achieve best film quality.

2. Developed SWNT thin film transfer process by using acetone bath procedure. Temperature, distance, and time were investigated to get uniform and intact film.

3. Designed VO_2-based MEMS actuator coated with SWNT thin film and developed compatible fabrication process related to VO_2 and SWNT.

4. Confirmed that the fabrication process does not alter the quality of SWNT and VO_2 thin film quality by conduction actuation, and that VO_2's structural transition still dominate the actuation of the devices.

5. Studied the photothermal performance of SWNT-coated VO_2 micro-actuators including photothermal efficiency and time response, which indicates significant improvement on both parameters.

6. Studied the relation between thickness of SWNT films (semiconducting and metallic) and wavelength selectivity, and calculated the optimum thickness for best wavelength selectivity.

7. Given the experimental results of unsorted SWNT coated VO_2-based actuators, design and fabricate a VO_2 actuator coated with different chirality distribution of SWNT thin film (semiconducting and metallic).

8. Demonstrate the wavelength selectivie actuation of SWNT-coated VO_2 micro-actuators with different chiralities.

9. Modelled the photo-thermo-mechanical process of VO_2/SWNT actuators, and confirmed the experimental results and simulation results.

10. Studied the effects of heat capacity and thermal conductivity of SWNT films on the performance of the actuators.

BIBLIOGRAPHY

BIBLIOGRAPHY

[1] R. Cabrera, E. Merced, and N. Sepúlveda, "Performance of electro-thermally driven VO_2-based MEMS actuators," *Microelectromechanical Systems, Journal of*, 2013. 10.1109/JMEMS.2013.2271774.

[2] K. Y. Tsai, T. S. Chin, and H. P. D. Shieh, "Effect of grain curvature on nano-indentation measurements of thin films," *Japanese Journal of Applied Physics*, vol. 43, pp. 6268–6273, 2004.

[3] C. N. Berglund and H. J. Guggenheim, "Electronic properties of vo_2 near the semiconductor-metal transition," *Phys. Rev.*, vol. 185, pp. 1022–1033, Sept. 1969.

[4] D.-W. Oh, C. Ko, S. Ramanathan, and D. G. Cahill, "Thermal conductivity and dynamic heat capacity across the metal-insulator transition in thin film vo_2," *Appl. Phys. Lett.*, vol. 96, no. 15, pp. 151906-1–151906-3, 2010.

[5] X. Zhang, Z. Yu, C. Wang, D. Zarrouk, J.-W. T. Seo, J. C. Cheng, A. D. Buchan, K. Takei, Y. Zhao, J. W. Ager, J. Zhang, M. Hettick, M. C. Hersam, A. P. Pisano, R. S. Fearing, and A. Javey, "Photoactuators and motors based on carbon nanotubes with selective chirality distributions," *Nat. Commun.*, vol. 5, pp. 2983–1–2983–8, Jan. 2014.

[6] E. Merced, N. Dávila, D. Torres, R. Cabrera, F. E. Fernández, and N. Sepúlveda, "Photothermal actuation of VO_2:Cr-coated microcantilevers in air and aqueous media," *Smart Materials and Structures*, vol. 21, no. 10, pp. 105009–1–105009–9, 2012.

[7] A. Rua, F. Fernández, and N. Sepúlveda, "Optoelectronic and full-optical multiple state memory response in phase-change materials," *J. Appl. Phys*, vol. 108, no. 11, 2010.

[8] N. R. Mlyuka, G. A. Niklasson, and C. G. Granqvist, "Mg doping of thermochromic vo_2 films enhances the optical transmittance and decreases the metal-insulator transition temperature," *Appl. Phys. Lett.*, vol. 95, no. 17, pp. 171909-1–171909-3, 2009.

[9] Y. Zhao, J. Hwan Lee, Y. Zhu, M. Nazari, C. Chen, H. Wang, A. Bernussi, M. Holtz, and Z. Fan, "Structural, electrical, and terahertz transmission properties of vo_2 thin films grown on c-, r-, and m-plane sapphire substrates," *J. Appl. Phys.*, vol. 111, no. 5, pp. 053533-1–053533-8, 2012.

[10] J. Sun, S. Guo, L. Wu, L. Liu, S.-W. Choe, B. S. Sorg, and H. Xie, "3d in vivo optical coherence tomography based on a low-voltage, large-scan-range 2d mems mirror," *Opt. Express*, vol. 18, pp. 12065–12075, Jun 2010.

[11] D. Yan, A. Khajepour, and R. Mansour, "Modeling of two-hot-arm horizontal thermal actuator," *Journal of Micromechanics and Microengineering*, vol. 13, no. 2, p. 312, 2003.

[12] T. Ebefors, J. U. Mattsson, E. Klvesten, and G. Stemme, "A robust micro conveyer realized by arrayed polyimide joint actuators," *Journal of Micromechanics and Microengineering*, vol. 10, no. 3, p. 337, 2000.

[13] O. C. Jeong, S. W. Park, S. S. Yang, and J. J. Pak, "Fabrication of a peristaltic {PDMS} micropump," *Sensors and Actuators A: Physical*, vol. 123124, pp. 453 – 458, 2005. Eurosensors {XVIII} 2004The 18th European conference on Solid-State Transducers.

[14] R. Horowitz, T.-L. Chen, K. Oldham, and Y. Li, "Microactuators for dual-stage servo systems in magnetic disk files," in *Springer Handbook of Nanotechnology*, pp. 951–981, Springer, 2004.

[15] E. Sarajlic, C. Yamahata, M. Cordero, and H. Fujita, "Three-phase electrostatic rotary stepper micromotor with a flexural pivot bearing," *Microelectromechanical Systems, Journal of*, vol. 19, no. 2, pp. 338–349, 2010.

[16] J. Grade, H. Jerman, and T. Kenny, "Design of large deflection electrostatic actuators," *Microelectromechanical Systems, Journal of*, vol. 12, no. 3, pp. 335–343, 2003.

[17] M. S. Rodgers, S. Kota, J. Hetrick, Z. Li, B. D. Jensen, T. W. Krygowski, S. L. Miller, S. M. Barnes, and M. S. Burg, "A new class of high force, low-voltage, compliant actuation systems," in *Proc. Solid-State Sensor and Actuator Workshop*, pp. 210–213, 2000.

[18] H. J. Cho and C. H. Ahn, "A bidirectional magnetic microactuator using electroplated permanent magnet arrays," *Microelectromechanical Systems, Journal of*, vol. 11, no. 1, pp. 78–84, 2002.

[19] M. Khoo and C. Liu, "Micro magnetic silicone elastomer membrane actuator," *Sensors and Actuators A: Physical*, vol. 89, no. 3, pp. 259–266, 2001.

[20] H. A. Tilmans, E. Fullin, H. Ziad, M. D. Van de Peer, J. Kesters, E. Van Geffen, J. Bergqvist, M. Pantus, E. Beyne, K. Baert, *et al.*, "A fully-packaged electromagnetic microrelay," in *Micro Electro Mechanical Systems, 1999. MEMS'99. Twelfth IEEE International Conference on*, pp. 25–30, IEEE, 1999.

[21] S. Gross, S. Tadigadapa, T. Jackson, S. Trolier-McKinstry, and Q. Zhang, "Lead-zirconate-titanate-based piezoelectric micromachined switch," *Applied Physics Letters*, vol. 83, no. 1, pp. 174–176, 2003.

[22] R. C. Ruby, P. Bradley, Y. Oshmyansky, A. Chien, and J. D. Larson III, "Thin film bulk wave acoustic resonators (fbar) for wireless applications," in *Ultrasonics Symposium, 2001 IEEE*, vol. 1, pp. 813–821, IEEE, 2001.

[23] Y. Q. Fu, J. K. Luo, S. E. Ong, S. Zhang, A. J. Flewitt, and W. I. Milne, "A shape memory microcage of TiNi/DLC films for biological applications," *Journal of Micromechanics and Microengineering*, vol. 18, no. 3, pp. 035026–1–035026–8, 2008.

[24] J. W. Zhou, H.-Y. Chan, T. K. To, K. W. Lai, and W. J. Li, "Polymer mems actuators for underwater micromanipulation," *Mechatronics, IEEE/ASME Transactions on*, vol. 9, no. 2, pp. 334–342, 2004.

[25] T. Bourouina, E. Lebrasseur, G. Reyne, A. Debray, H. Fujita, A. Ludwig, E. Quandt, H. Muro, T. Oki, and A. Asaoka, "Integration of two degree-of-freedom magnetostrictive actuation and piezoresistive detection: application to a two-dimensional optical scanner," *Microelectromechanical Systems, Journal of*, vol. 11, no. 4, pp. 355–361, 2002.

[26] A. Rúa, F. E. Fernández, and N. Sepúlveda, "Bending in VO_2-coated microcantilevers suitable for thermally activated actuators," *Journal of Applied Physics*, vol. 107, no. 7, pp. 074506–1–074506–4, 2010.

[27] H. Kakiuchida, P. Jin, S. Nakao, and M. Tazawa, "Optical properties of vanadium dioxide film during semiconductive–metallic phase transition," *Japanese Journal of Applied Physics*, vol. 46, no. 2L, p. L113, 2007.

[28] V. Eyert, "The metal-insulator transitions of VO_2: A band theoretical approach," *Annalen der Physik*, vol. 11, no. 9, pp. 650–704, 2002.

[29] Q. Su, C. Huang, Y. Wang, Y. Fan, B. Lu, W. Lan, Y. Wang, and X. Liu, "Formation of vanadium oxides with various morphologies by chemical vapor deposition," *Journal of Alloys and Compounds*, vol. 475, no. 1, pp. 518–523, 2009.

[30] S. Sheshmani, A. Ashori, and M. A. Fashapoyeh, "Wood plastic composite using graphene nanoplatelets," *International journal of biological macromolecules*, vol. 58, pp. 1–6, 2013.

[31] A. Szabó, C. Perri, A. Csató, G. Giordano, D. Vuono, and J. B. Nagy, "Synthesis methods of carbon nanotubes and related materials," *Materials*, vol. 3, no. 5, pp. 3092–3140, 2010.

[32] S. J. Henley, J. V. Anguita, and S. R. P. Silva, *Encyclopedia of Nanotechnology*, ch. Synthesis of Carbon Nanotubes, pp. 2615–2621. Dordrecht: Springer Netherlands, 2012.

[33] J. Prasek, J. Drbohlavova, J. Chomoucka, J. Hubalek, O. Jasek, V. Adam, and R. Kizek, "Methods for carbon nanotubes synthesisreview," *Journal of Materials Chemistry*, vol. 21, no. 40, pp. 15872–15884, 2011.

[34] R. Saito, M. Fujita, G. Dresselhaus, and u. M. Dresselhaus, "Electronic structure of chiral graphene tubules," *Applied physics letters*, vol. 60, no. 18, pp. 2204–2206, 1992.

[35] S. M. Bachilo, M. S. Strano, C. Kittrell, R. H. Hauge, R. E. Smalley, and R. B. Weisman, "Structure-assigned optical spectra of single-walled carbon nanotubes," *Science*, vol. 298, no. 5602, pp. 2361–2366, 2002.

[36] H. Liu, D. Nishide, T. Tanaka, and H. Kataura, "Large-scale single-chirality separation of single-wall carbon nanotubes by simple gel chromatography," *Nature communications*, vol. 2, p. 309, 2011.

[37] F. Morin, "Oxides which show a metal-to-insulator transition at the neel temperature," *Physical Review Letters*, vol. 3, no. 1, pp. 34–36, 1959.

[38] M. Imada, A. Fujimori, and Y. Tokura, "Metal-insulator transitions," *Rev. Mod. Phys.*, vol. 70, pp. 1039–1263, Oct. 1998.

[39] M. W. Haverkort, Z. Hu, A. Tanaka, W. Reichelt, S. V. Streltsov, M. A. Korotin, V. I. Anisimov, H. H. Hsieh, H.-J. Lin, C. T. Chen, D. I. Khomskii, and L. H. Tjeng, "Orbital-assisted metal-insulator transition in vo_2," *Phys. Rev. Lett.*, vol. 95, pp. 196404-1–196404-4, Nov. 2005.

[40] S. Lysenko, V. Vikhnin, G. Zhang, A. Rua, F. E. Fernández, and H. Liu, "Insulator-to-metal phase transformation of vo_2 films upon femtosecond laser excitation," *J. Electron. Mater.*, vol. 35, no. 10, pp. 1866–1872, 2006.

[41] B. Hu, Y. Ding, W. Chen, D. Kulkarni, Y. Shen, V. V. Tsukruk, and Z. L. Wang, "External-strain induced insulating phase transition in vo_2 nanobeam and its application as flexible strain sensor," *Adv. Mater.*, vol. 22, no. 45, pp. 5134–5139, 2010.

[42] C. Ko and S. Ramanathan, "Observation of electric field-assisted phase transition in thin film vanadium oxide in a metal-oxide-semiconductor device geometry," *Appl. Phys. Lett.*, vol. 93, no. 25, pp. 252101-1–252101-3, 2008.

[43] A. S. Barker, H. W. Verleur, and H. J. Guggenheim, "Infrared optical properties of vanadium dioxide above and below the transition temperature," *Phys. Rev. Lett.*, vol. 17, pp. 1286–1289, Dec. 1966.

[44] H. W. Verleur, A. S. Barker, and C. N. Berglund, "Optical properties of vo_2 between 0.25 and 5 ev," *Phys. Rev.*, vol. 172, pp. 788–798, Aug. 1968.

[45] N. F. Mott and L. Friedman, "Metal-insulator transitions in vo_2, ti_2o_3 and $ti_{2-x}\ v_x o_3$," *Philos. Mag.*, vol. 30, pp. 389–402, Aug. 1974.

[46] G. Stefanovich, A. Pergament, and D. Stefanovich, "Electrical switching and mott transition in vo_2," *J. Phys.: Condens. Matter*, vol. 12, no. 41, pp. 8837–8845, 2000.

[47] A. Cavalleri, T. Dekorsy, H. H. W. Chong, J. C. Kieffer, and R. W. Schoenlein, "Evidence for a structurally-driven insulator-to-metal transition in vo_2: A view from the ultrafast timescale," *Phys. Rev. B*, vol. 70, pp. 161102-1–161102-4, Oct. 2004.

[48] J. Cao, W. Fan, Q. Zhou, E. Sheu, A. Liu, C. Barrett, and J. Wu, "Colossal thermal-mechanical actuation *via* phase transition in single-crystal vo_2 microcantilevers," *J. Appl. Phys.*, vol. 108, no. 8, pp. 083538-1–083538-4, 2010.

[49] R. Cabrera, E. Merced, and N. Sepúlveda, "A micro-electro-mechanical memory based on the structural phase transition of vo_2," *Phys. Status Solidi A*, vol. 210, no. 9, pp. 1704–1711, 2013.

[50] N. Davila, E. Merced, and N. Sepúlveda, "Electronically variable optical attenuator enabled by self-sensing in vanadium dioxide," *IEEE Photonics Technol. Lett.*, vol. 26, no. 10, pp. 1011–1014, 2014.

[51] S. Ha, Y. Zhou, A. Duwel, D. White, and S. Ramanathan, "Quick switch: Strongly correlated electronic phase transition systems for cutting-edge microwave devices," *IEEE Microwave Magazine*, vol. 15, no. 6, pp. 32–44, 2014.

[52] E. Merced, X. Tan, and N. Seplveda, "Strain energy density of VO_2-based microactuators," *Sensors and Actuators A: Physical*, vol. 196, pp. 30–37, 2013.

[53] K. Liu, C. Cheng, Z. Cheng, K. Wang, R. Ramesh, and J. Wu, "Giant-amplitude, high-work density microactuators with phase transition activated nanolayer bimorphs," *Nano Lett.*, vol. 12, pp. 6302–6308, Dec. 2012.

[54] S. Lee, C. Cheng, H. Guo, K. Hippalgaonkar, K. Wang, J. Suh, K. Liu, and J. Wu, "Axially engineered metal-insulator phase transition by graded doping vo_2 nanowires," *J. Am. Chem. Soc.*, vol. 135, no. 12, pp. 4850–4855, 2013.

[55] A. Tselev, J. D. Budai, E. Strelcov, J. Z. Tischler, A. Kolmakov, and S. V. Kalinin, "Electromechanical actuation and current-induced metastable states in suspended single-crystalline vo_2 nanoplatelets," *Nano Lett.*, vol. 11, no. 8, pp. 3065–3073, 2011.

[56] L. Pellegrino, N. Manca, T. Kanki, H. Tanaka, M. Biasotti, E. Bellingeri, A. S. Siri, and D. Marré, "Multistate memory devices based on free-standing vo_2/tio_2 microstructures driven by joule self-heating," *Adv. Mater.*, vol. 24, no. 21, pp. 2929–2934, 2012.

[57] S.-H. Bae, S. Lee, H. Koo, L. Lin, B. H. Jo, C. Park, and Z. L. Wang, "The memristive properties of a single vo_2 nanowire with switching controlled by self-heating," *Adv. Mater.*, vol. 25, no. 36, pp. 5098–5103, 2013.

[58] H. Coy, R. Cabrera, N. Sepúlveda, and F. E. Fernández, "Optoelectronic and all-optical multiple memory states in vanadium dioxide," *J. Appl. Phys.*, vol. 108, no. 11, pp. 113115-1–113115-6, 2010.

[59] F. Najar, S. Choura, S. El-Borgi, E. M. Abdel-Rahman, and A. H. Nayfeh, "Modeling and design of variable-geometry electrostatic microactuators," *J. Micromech. Microeng.*, vol. 15, no. 3, pp. 419–429, 2005.

[60] H. Adriaens, W. De Koning, and R. Banning, "Modeling piezoelectric actuators," *IEEE/ASME Transactions on Mechatronics*, vol. 5, pp. 331–341, Dec 2000.

[61] L. Que, J.-S. Park, and Y. Gianchandani, "Bent-beam electro-thermal actuators for high force applications," in *12th IEEE International Conference on Micro Electro Mechanical Systems*, (Orlando, Florida, United States), pp. 31–36, IEEE, Jan 17–21 1999.

[62] L. Que, J.-S. Park, and Y. Gianchandani, "Bent-beam electrothermal actuators-part i: Single beam and cascaded devices," *J. Microelectromech. Syst.*, vol. 10, pp. 247–254, June 2001.

[63] L. Que, J.-S. Park, M.-H. Li, and Y. Gianchandani, "Reliability studies of bent-beam electro-thermal actuators," in *Proceedings of 38th Annual IEEE International Reliability Physics Symposium*, (San Jose, Carlifonia, United States), pp. 118–122, Apr 10–13 2000.

[64] J. Luo, Y. Q. Fu, J. A. Williams, and W. Milne, "Thermal degradation of electroplated nickel thermal microactuators," *Microelectromechanical Systems, Journal of*, vol. 18, no. 6, pp. 1279–1287, 2009.

[65] Y. Zhao, G. Karaoglan-Bebek, X. Pan, M. Holtz, A. A. Bernussi, and Z. Fan, "Hydrogen-doping stabilized metallic vo_2 (r) thin films and their application to suppress fabry-perot resonances in the terahertz regime," *Appl. Phys. Lett.*, vol. 104, no. 24, pp. 241901-1–241901-5, 2014.

[66] J. Li and J. Dho, "Characteristics of phase transition of vo_2 films grown on tio_2 substrates with different crystal orientations," *J. Cryst. Growth*, vol. 404, no. 0, pp. 84–88, 2014.

[67] J. Wright, Y.-C. Tai, and S.-C. Chang, "A large-force, fully-integrated MEMS magnetic actuator," in *Solid State Sensors and Actuators, International Conference on*, vol. 2, pp. 793–796, 1997.

[68] C. H. Ko, J. J. Yang, and J. C. Chiou, "Efficient magnetic microactuator with an enclosed magnetic core," *Journal of Microlithography, Microfabrication and Microsystems*, vol. 1, pp. 144–149, 2002.

[69] J. Juuti, K. Kords, R. Lonnakko, V.-P. Moilanen, and S. Leppvuori, "Mechanically amplified large displacement piezoelectric actuators," *Sensors and Actuators A: Physical*, vol. 120, no. 1, pp. 225–231, 2005.

[70] R. Legtenberg, A. W. Groeneveld, and M. Elwenspoek, "Comb-drive actuators for large displacements," *Journal of Micromechanics and Microengineering*, vol. 6, no. 3, pp. 320–329, 1996.

[71] E. J. García and J. J. Sniegowski, "Surface micromachined microengine," *Sensors and Actuators A: Physical*, vol. 48, no. 3, pp. 203–214, 1995.

[72] P. H. Pham, D. V. Dao, L. B. Dang, and S. Sugiyama, "Single mask, simple structure micro rotational motor driven by electrostatic comb-drive actuators," *Journal of Micromechanics and Microengineering*, vol. 22, no. 1, pp. 015008–1–015008–7, 2012.

[73] D. J. Bell, T. J. Lu, N. A. Fleck, and S. M. Spearing, "MEMS actuators and sensors: observations on their performance and selection for purpose," *Journal of Micromechanics and Microengineering*, vol. 15, no. 7, pp. S153–S164, 2005.

[74] M. Mita, M. Arai, S. Tensaka, D. Kobayashi, and H. Fujita, "A micromachined impact microactuator driven by electrostatic force," *Microelectromechanical Systems, Journal of*, vol. 12, no. 1, pp. 37–41, 2003.

[75] T. Akiyama, D. Collard, and H. Fujita, "Scratch drive actuator with mechanical links for self-assembly of three-dimensional MEMS," *Microelectromechanical Systems, Journal of*, vol. 6, no. 1, pp. 10–17, 1997.

[76] B. Kim, M. G. Lee, Y. P. Lee, Y. Kim, and G. Lee, "An earthworm-like micro robot using shape memory alloy actuator," *Sensors and Actuators A: Physical*, vol. 125, no. 2, pp. 429–437, 2006.

[77] O. C. Jeong and S. S. Yang, "Fabrication of a thermopneumatic microactuator with a corrugated p plus silicon diaphragm," *Sensors and Actuators A: Physical*, vol. 80, no. 1, pp. 62–67, 2000.

[78] P. Krulevitch, A. Lee, P. Ramsey, J. Trevino, J. Hamilton, and M. Northrup, "Thin film shape memory alloy microactuators," *Microelectromechanical Systems, Journal of*, vol. 5, no. 4, pp. 270–282, 1996.

[79] J. Suh, C. Storment, and G. T. A. Kovacs, "Characterization of multi-segment organic thermal actuators," in *Solid-State Sensors and Actuators, International Conference on*, vol. 2, pp. 333–336, 1995.

[80] M. C. LeMieux, M. E. McConney, Y.-H. Lin, S. Singamaneni, H. Jiang, T. J. Bunning, and V. V. Tsukruk, "Polymeric nanolayers as actuators for ultrasensitive thermal bimorphs," *Nano Letters*, vol. 6, no. 4, pp. 730–734, 2006.

[81] E. Enikov, S. Kedar, and K. Lazarov, "Analytical model for analysis and design of V-shaped thermal microactuators," *Microelectromechanical Systems, Journal of*, vol. 14, no. 4, pp. 788–798, 2005.

[82] A. Atre, "Analysis of out-of-plane thermal microactuators," *Journal of Micromechanics and Microengineering*, vol. 16, no. 2, pp. 205–213, 2006.

[83] G. Alici, V. Devaud, P. Renaud, and G. Spinks, "Conducting polymer microactuators operating in air," *Journal of Micromechanics and Microengineering*, vol. 19, no. 2, pp. 025017–1–025017–9, 2009.

[84] Z. Chen and X. Tan, "Monolithic fabrication of ionic polymermetal composite actuators capable of complex deformation," *Sensors and Actuators A: Physical*, vol. 157, no. 2, pp. 246–257, 2010.

[85] B. Gaihre, G. Alici, G. M. Spinks, and J. Cairney, "Pushing the limits for microactuators based on electroactive polymers," *Microelectromechanical Systems, Journal of*, vol. 21, no. 3, pp. 574–585, 2012.

[86] N. Conway and S.-G. Kim, "Large-strain, piezoelectric, in-plane micro-actuator," in *Micro Electro Mechanical Systems, International Conference on. (MEMS)*, pp. 454–457, 2004.

[87] N. J. Graf and M. T. Browser, "A soft-polymer piezoelectric bimorph cantilever-actuated peristaltic micropump," *Lab Chip*, vol. 8, no. 10, p. 16641670, 2008.

[88] Y. Zhao and T. Cui, "Fabrication of high-aspect-ratio polymer-based electrostatic comb drives using the hot embossing technique," *Journal of Micromechanics and Microengineering*, vol. 13, no. 3, p. 430, 2003.

[89] L. Li, J. G. Brown, and D. Uttamchandani, "Study of scratch drive actuator force characteristics," *Journal of Micromechanics and microengineering*, vol. 12, no. 6, p. 736, 2002.

[90] J. J. Yao, S. C. Arney, and N. C. MacDonald, "Fabrication of high frequency two-dimensional nanoactuators for scanned probe devices," *Microelectromechanical Systems, Journal of*, vol. 1, no. 1, pp. 14–22, 1992.

[91] R. Yeh, S. Hollar, and K. S. Pister, "Single mask, large force, and large displacement electrostatic linear inchworm motors," *Microelectromechanical Systems, Journal of*, vol. 11, no. 4, pp. 330–336, 2002.

[92] K. Minami, S. Kawamura, and M. Esashi, "Fabrication of distributed electrostatic micro actuator (dema)," *Microelectromechanical Systems, Journal of*, vol. 2, no. 3, pp. 121–127, 1993.

[93] K. B. Lee and Y.-H. Cho, "Laterally driven electrostatic repulsive-force microactuators using asymmetric field distribution," *Microelectromechanical Systems, Journal of*, vol. 10, no. 1, pp. 128–136, 2001.

[94] R. Legtenberg, J. Gilbert, S. D. Senturia, and M. Elwenspoek, "Electrostatic curved electrode actuators," *Microelectromechanical Systems, Journal of*, vol. 6, no. 3, pp. 257–265, 1997.

[95] M. Shikida, K. Sato, and T. Harada, "Fabrication of an s-shaped microactuator," *Microelectromechanical Systems, Journal of*, vol. 6, no. 1, pp. 18–24, 1997.

[96] H.-S. Lee, C. H. Leung, J. Shi, S.-C. Chang, S. Lorincz, and I. Nedelescu, "Integrated microrelays: Concept and initial results," *Microelectromechanical Systems, Journal of*, vol. 11, no. 2, pp. 147–153, 2002.

[97] M. Ruan, J. Shen, and C. B. Wheeler, "Latching micromagnetic relays," *Microelectromechanical Systems, Journal of*, vol. 10, no. 4, pp. 511–517, 2001.

[98] M. Madou, "Fundamentals of microfabrication (crc, boca raton, fl)," *MadouFundamentals of Microfabrication1997*, 1997.

[99] A. Manbachi and R. S. Cobbold, "Development and application of piezoelectric materials for ultrasound generation and detection," *Ultrasound*, vol. 19, no. 4, pp. 187–196, 2011.

[100] K. Otsuka and C. M. Wayman, *Shape memory materials*. Cambridge university press, 1999.

[101] R. Pelrine, R. Kornbluh, Q. Pei, and J. Joseph, "High-speed electrically actuated elastomers with strain greater than 100%," *Science*, vol. 287, no. 5454, pp. 836–839, 2000.

[102] R. E. Pelrine, R. D. Kornbluh, and J. P. Joseph, "Electrostriction of polymer dielectrics with compliant electrodes as a means of actuation," *Sensors and Actuators A: Physical*, vol. 64, no. 1, pp. 77 – 85, 1998. Tenth {IEEE} International Workshop on Micro Electro Mechanical Systems.

[103] K. J. Kim and S. Tadokoro, "Electroactive polymers for robotic applications," *Artificial Muscles and Sensors (291 p.), Springer: London, United Kingdom*, 2007.

[104] M. Shahinpoor, Y. Bar-Cohen, J. Simpson, and J. Smith, "Ionic polymer-metal composites (ipmcs) as biomimetic sensors, actuators and artificial muscles-a review," *Smart materials and structures*, vol. 7, no. 6, p. R15, 1998.

[105] X. Tan and J. S. Baras, "Modeling and control of hysteresis in magnetostrictive actuators," *Automatica*, vol. 40, no. 9, pp. 1469–1480, 2004.

[106] J. Nag, R. F. Haglund, E. Andrew Payzant, and K. L. More, "Non-congruence of thermally driven structural and electronic transitions in VO_2," *Journal of Applied Physics*, vol. 112, no. 10, pp. 103532–1–103532–7, 2012.

[107] J. B. Goodenough, "The two components of the crystallographic transition in VO_2," *Journal of Solid State Chemistry*, vol. 3, no. 4, pp. 490–500, 1971.

[108] P. Dernier, "Structural investigation of the metal-insulator transition in V_6O_{13}," *Materials Research Bulletin*, vol. 9, no. 7, pp. 955–963, 1974.

[109] J. Feinleib and W. Paul, "Semiconductor-to-metal transition in V_2O_3," *Physical Review*, vol. 155, pp. 841–850, 1967.

[110] K. Kosuge, "The phase diagram and phase transition of the V_2O_3-V_2O_5, system," *Journal of Physics and Chemistry of Solids*, vol. 28, no. 8, pp. 1613–1621, 1967.

[111] W. Burkhardt, T. Christmann, B. Meyer, W. Niessner, D. Schalch, and A. Scharmann, "W- and F-doped VO_2 films studied by photoelectron spectrometry," *Thin Solid Films*, vol. 345, no. 2, pp. 229–235, 1999.

[112] S. Kabashima, T. Goto, K. Nishimura, and T. Kawakubo, "Impurity conduction in Ti-doped VO_2 studied by microwave frequency conductivity," *Journal of the Physical Society of Japan*, vol. 32, no. 1, pp. 158–163, 1972.

[113] M. Marezio, D. B. McWhan, J. P. Remeika, and P. D. Dernier, "Structural aspects of the metal-insulator transitions in Cr-doped VO_2," *Physical Review B*, vol. 5, pp. 2541–2551, 1972.

[114] T. Phillips, R. Murphy, and T. Poehler, "Electrical studies of reactively sputtered Fe-doped VO_2 thin films," *Materials Research Bulletin*, vol. 22, no. 8, pp. 1113–1123, 1987.

[115] S. Kumar, M. D. Pickett, J. P. Strachan, G. Gibson, Y. Nishi, and R. S. Williams, "Local temperature redistribution and structural transition during joule-heating-driven conductance switching in vo2," *Advanced Materials*, vol. 25, no. 42, pp. 6128–6132, 2013.

[116] M. Kang, S. W. Kim, J.-W. Ryu, and T. Noh, "Optical properties for the mott transition in vo2," *AIP Advances*, vol. 2, no. 1, p. 012168, 2012.

[117] J. Nag and R. Haglund Jr, "Synthesis of vanadium dioxide thin films and nanoparticles," *Journal of Physics: Condensed Matter*, vol. 20, no. 26, p. 264016, 2008.

[118] T. D. Manning, I. P. Parkin, R. J. Clark, D. Sheel, M. E. Pemble, and D. Vernadou, "Intelligent window coatings: atmospheric pressure chemical vapour deposition of vanadium oxides," *Journal of Materials Chemistry*, vol. 12, no. 10, pp. 2936–2939, 2002.

[119] D. Vernardou, M. Pemble, and D. Sheel, "In-situ ftir studies of the growth of vanadium dioxide coatings on glass by atmospheric pressure chemical vapour deposition for vcl 4 and h 2 o system," *Thin Solid Films*, vol. 515, no. 24, pp. 8768–8770, 2007.

[120] B. G. Chae and H. T. Kim, "Effects of w doping on the metal–insulator transition in vanadium dioxide film," *Physica B: Condensed Matter*, vol. 405, no. 2, pp. 663–667, 2010.

[121] J.-H. Cho, Y.-J. Byun, J.-H. Kim, Y.-J. Lee, Y.-H. Jeong, M.-P. Chun, J.-H. Paik, and T. H. Sung, "Thermochromic characteristics of wo 3-doped vanadium dioxide thin films prepared by sol–gel method," *Ceramics International*, vol. 38, pp. S589–S593, 2012.

[122] M. Pan, H. Zhong, S. Wang, J. Liu, Z. Li, X. Chen, and W. Lu, "Properties of vo 2 thin film prepared with precursor vo (acac) 2," *Journal of Crystal Growth*, vol. 265, no. 1, pp. 121–126, 2004.

[123] T. Hanlon, J. Coath, and M. Richardson, "Molybdenum-doped vanadium dioxide coatings on glass produced by the aqueous sol–gel method," *Thin Solid Films*, vol. 436, no. 2, pp. 269–272, 2003.

[124] J. Duchene, M. Terraillon, and M. Pailly, "Rf and dc reactive sputtering for crystalline and amorphous vo 2 thin film deposition," *Thin Solid Films*, vol. 12, no. 2, pp. 231–234, 1972.

[125] R. Dillon, K. Le, and N. Ianno, "Thermochromic VO_2 sputtered by control of a vanadium-oxygen emission ratio," *Thin Solid Films*, vol. 398, pp. 10–16, 2001.

[126] N. Mlyuka and R. Kivaisi, "Correlation between optical, electrical and structural properties of vanadium dioxide thin films," *Journal of materials science*, vol. 41, no. 17, pp. 5619–5624, 2006.

[127] F. Guinneton, J.-C. Valmalette, and J.-R. Gavarri, "Nanocrystalline vanadium dioxide: synthesis and mid-infrared properties," *Optical Materials*, vol. 15, no. 2, pp. 111–114, 2000.

[128] F. Guinneton, L. Sauques, J. Valmalette, F. Cros, and J. Gavarri, "Comparative study between nanocrystalline powder and thin film of vanadium dioxide vo 2: electrical and infrared properties," *Journal of Physics and Chemistry of Solids*, vol. 62, no. 7, pp. 1229–1238, 2001.

[129] J. Y. Suh, R. Lopez, L. C. Feldman, and R. Haglund Jr, "Semiconductor to metal phase transition in the nucleation and growth of vo2 nanoparticles and thin films," *Journal of Applied Physics*, vol. 96, no. 2, pp. 1209–1213, 2004.

[130] S. J. Tans, M. H. Devoret, H. Dai, A. Thess, R. E. Smalley, L. Georliga, and C. Dekker, "Individual single-wall carbon nanotubes as quantum wires," *Nature 386 (6624), 474-477.(1997)*, 1997.

[131] M. Bockrath, D. H. Cobden, P. L. McEuen, N. G. Chopra, A. Zettl, A. Thess, and R. E. Smalley, "Single-electron transport in ropes of carbon nanotubes," *Science*, vol. 275, no. 5308, pp. 1922–1925, 1997.

[132] S. J. Tans, A. R. Verschueren, and C. Dekker, "Room-temperature transistor based on a single carbon nanotube," *Nature*, vol. 393, no. 6680, pp. 49–52, 1998.

[133] A. Javey, J. Guo, Q. Wang, M. Lundstrom, and H. Dai, "Ballistic carbon nanotube field-effect transistors," *nature*, vol. 424, no. 6949, pp. 654–657, 2003.

[134] Z. Chen, J. Appenzeller, Y.-M. Lin, J. Sippel-Oakley, A. G. Rinzler, J. Tang, S. J. Wind, P. M. Solomon, and P. Avouris, "An integrated logic circuit assembled on a single carbon nanotube," *Science*, vol. 311, no. 5768, pp. 1735–1735, 2006.

[135] S. J. Kang, C. Kocabas, T. Ozel, M. Shim, N. Pimparkar, M. A. Alam, S. V. Rotkin, and J. A. Rogers, "High-performance electronics using dense, perfectly aligned arrays of single-walled carbon nanotubes," *Nature nanotechnology*, vol. 2, no. 4, pp. 230–236, 2007.

[136] D.-m. Sun, M. Y. Timmermans, Y. Tian, A. G. Nasibulin, E. I. Kauppinen, S. Kishimoto, T. Mizutani, and Y. Ohno, "Flexible high-performance carbon nanotube integrated circuits," *Nature nanotechnology*, vol. 6, no. 3, pp. 156–161, 2011.

[137] K. Ryu, A. Badmaev, C. Wang, A. Lin, N. Patil, L. Gomez, A. Kumar, S. Mitra, H.-S. P. Wong, and C. Zhou, "Cmos-analogous wafer-scale nanotube-on-insulator approach for submicrometer devices and integrated circuits using aligned nanotubes," *Nano Letters*, vol. 9, no. 1, pp. 189–197, 2008.

[138] Z. Liu, S. Tabakman, K. Welsher, and H. Dai, "Carbon nanotubes in biology and medicine: in vitro and in vivo detection, imaging and drug delivery," *Nano research*, vol. 2, no. 2, pp. 85–120, 2009.

[139] W. Kratschmer, L. D. Lamb, K. Fostiropoulos, and D. Huffman, "Solid c60: a new form of carbon," *Nature*, vol. 347, p. 27, 1990.

[140] S. Iijima *et al.*, "Helical microtubules of graphitic carbon," *nature*, vol. 354, no. 6348, pp. 56–58, 1991.

[141] T. Ebbesen and P. Ajayan, "Large-scale synthesis of carbon nanotubes," *Nature*, vol. 358, no. 6383, pp. 220–222, 1992.

[142] M. Itkis, D. Perea, S. Niyogi, J. Love, J. Tang, A. Yu, C. Kang, R. Jung, and R. Haddon, "Optimization of the ni-y catalyst composition in bulk electric arc synthesis of single-walled carbon nanotubes by use of near-infrared spectroscopy," *The Journal of Physical Chemistry B*, vol. 108, no. 34, pp. 12770–12775, 2004.

[143] C. Journet, W. Maser, P. Bernier, A. Loiseau, M. L. De La Chapelle, d. l. S. Lefrant, P. Deniard, R. Lee, and J. Fischer, "Large-scale production of single-walled carbon nanotubes by the electric-arc technique," *nature*, vol. 388, no. 6644, pp. 756–758, 1997.

[144] M. Itkis, D. Perea, S. Niyogi, J. Love, J. Tang, A. Yu, C. Kang, and R. Haddon, "Optimization of the electric arc discharge synthesis of single-walled carbon nanotubes on the basis of near-ir spectroscopy," in *APS Meeting Abstracts*, vol. 1, p. 17006, 2004.

[145] T. Guo, P. Nikolaev, A. G. Rinzler, D. Tomanek, D. T. Colbert, and R. E. Smalley, "Self-assembly of tubular fullerenes," *The Journal of Physical Chemistry*, vol. 99, no. 27, pp. 10694–10697, 1995.

[146] B. I. Yakobson and R. E. Smalley, "Fullerene nanotubes: C 1,000,000 and beyond: Some unusual new moleculeslong, hollow fibers with tantalizing electronic and mechanical propertieshave joined diamonds and graphite in the carbon family," *American Scientist*, vol. 85, no. 4, pp. 324–337, 1997.

[147] T. Guo, P. Nikolaev, A. Thess, D. Colbert, and R. Smalley, "Catalytic growth of single-walled manotubes by laser vaporization," *Chemical physics letters*, vol. 243, no. 1, pp. 49–54, 1995.

[148] A. Thess, R. Lee, P. Nikolaev, and H. Dai, "Crystalline ropes of metallic carbon nanotubes," *Science*, vol. 273, no. 5274, p. 483, 1996.

[149] Y. Zhang, A. Chang, J. Cao, Q. Wang, W. Kim, Y. Li, N. Morris, E. Yenilmez, J. Kong, and H. Dai, "Electric-field-directed growth of aligned single-walled carbon nanotubes," *Applied physics letters*, vol. 79, no. 19, pp. 3155–3157, 2001.

[150] Q. Wen, W. Qian, J. Nie, A. Cao, G. Ning, Y. Wang, L. Hu, Q. Zhang, J. Huang, and F. Wei, "100 mm long, semiconducting triple-walled carbon nanotubes," *Advanced Materials*, vol. 22, no. 16, pp. 1867–1871, 2010.

[151] S. Huang, B. Maynor, X. Cai, and J. Liu, "Ultralong, well-aligned single-walled carbon nanotube architectureson surfaces," *Advanced Materials*, vol. 15, no. 19, pp. 1651–1655, 2003.

[152] L. An, J. M. Owens, L. E. McNeil, and J. Liu, "Synthesis of nearly uniform single-walled carbon nanotubes using identical metal-containing molecular nanoclusters as catalysts," *Journal of the American Chemical Society*, vol. 124, no. 46, pp. 13688–13689, 2002.

[153] Q. Fu, S. Huang, and J. Liu, "Chemical vapor depositions of single-walled carbon nanotubes catalyzed by uniform fe2o3 nanoclusters synthesized using diblock copolymer micelles," *The Journal of Physical Chemistry B*, vol. 108, no. 20, pp. 6124–6129, 2004.

[154] T. Yamada, T. Namai, K. Hata, D. N. Futaba, K. Mizuno, J. Fan, M. Yudasaka, M. Yumura, and S. Iijima, "Size-selective growth of double-walled carbon nanotube forests from engineered iron catalysts," *Nature nanotechnology*, vol. 1, no. 2, pp. 131–136, 2006.

[155] C. L. Cheung, A. Kurtz, H. Park, and C. M. Lieber, "Diameter-controlled synthesis of carbon nanotubes," *The Journal of Physical Chemistry B*, vol. 106, no. 10, pp. 2429–2433, 2002.

[156] Y. Li, D. Mann, M. Rolandi, W. Kim, A. Ural, S. Hung, A. Javey, J. Cao, D. Wang, E. Yenilmez, *et al.*, "Preferential growth of semiconducting single-walled carbon nanotubes by a plasma enhanced cvd method," *Nano Letters*, vol. 4, no. 2, pp. 317–321, 2004.

[157] G. Hong, B. Zhang, B. Peng, J. Zhang, W. M. Choi, J.-Y. Choi, J. M. Kim, and Z. Liu, "Direct growth of semiconducting single-walled carbon nanotube array," *Journal of the American Chemical Society*, vol. 131, no. 41, pp. 14642–14643, 2009.

[158] L. Ding, A. Tselev, J. Wang, D. Yuan, H. Chu, T. P. McNicholas, Y. Li, and J. Liu, "Selective growth of well-aligned semiconducting single-walled carbon nanotubes," *Nano letters*, vol. 9, no. 2, pp. 800–805, 2009.

[159] S. Ghosh, S. M. Bachilo, and R. B. Weisman, "Advanced sorting of single-walled carbon nanotubes by nonlinear density-gradient ultracentrifugation," *Nature nanotechnology*, vol. 5, no. 6, pp. 443–450, 2010.

[160] A. A. Green and M. C. Hersam, "Nearly single-chirality single-walled carbon nanotubes produced via orthogonal iterative density gradient ultracentrifugation," *Advanced Materials*, vol. 23, no. 19, pp. 2185–2190, 2011.

[161] X. Tu, S. Manohar, A. Jagota, and M. Zheng, "Dna sequence motifs for structure-specific recognition and separation of carbon nanotubes," *Nature*, vol. 460, no. 7252, pp. 250–253, 2009.

[162] T. Wang, D. Torres, F. E. Fernandez, A. J. Green, C. Wang, and N. Sepúlveda, "Increasing efficiency, speed, and responsivity of vanadium dioxide based photothermally driven actuators using single-wall carbon nanotube thin-films," *ACS nano*, vol. 9, no. 4, pp. 4371–4378, 2015.

[163] J. Corbeil, N. Lavrik, S. Rajic, and P. Datskos, ""self-leveling" uncooled microcantilever thermal detector," *Applied Physics Letters*, vol. 81, no. 7, pp. 1306–1308, 2002.

[164] R. Cabrera, E. Merced, and N. Sepúlveda, "Performance of electro-thermally driven VO_2-based mems actuators," *Journal of Microelectromechanical Systems*, vol. 23, no. 1, pp. 243–251, 2014.

[165] F. Lian, J. P. Llinas, Z. Li, D. Estrada, and E. Pop, "Thermal conductivity of chirality-sorted carbon nanotube networks," *Applied Physics Letters*, vol. 108, no. 10, p. 103101, 2016.

[166] W. S. Levine, *The Control Systems Handbook: Control System Advanced Methods*. CRC press, 2010.